



**THE UNIVERSITY  
OF BIRMINGHAM**

# **Novel waveguide filters in communication systems**

**Daxin Wang**

A thesis submitted to the University of Birmingham for the degree of

**DOCTOR OF PHILOSOPHY**

**School of Electronic, Electrical and Systems Engineering**

**The University of Birmingham**

**March 2023**

UNIVERSITY OF  
BIRMINGHAM

**University of Birmingham Research Archive**

**e-theses repository**

This unpublished thesis/dissertation is copyright of the author and/or third parties. The intellectual property rights of the author or third parties in respect of this work are as defined by The Copyright Designs and Patents Act 1988 or as modified by any successor legislation.

Any use made of information contained in this thesis/dissertation must be in accordance with that legislation and must be properly acknowledged. Further distribution or reproduction in any format is prohibited without the permission of the copyright holder.

# Abstract

This thesis presents the design and fabrication of several waveguide bandpass filters operating at X band (8-12 GHz), V band (50-75 GHz) and WR-1.5 band (500-750 GHz). A WR-1.5 band (500-750 GHz) 3<sup>rd</sup> order waveguide bandpass filter has been designed and manufactured using high-precision computer numerically controlled (CNC) metal machining. This filter is used as a prototype to find the tolerance of commercial CNC milling machine. The sensitivity analysis and yield analysis are presented to help estimate the real production and improve the fabrication tolerance. However, the long waveguide section in that filter leads to additional losses. To reduce the loss of waveguide, the filter can be shortened by applying folded structure, which can make the whole structure more compact. Therefore, the filters with folded structure was developed. The folded structure allows a very compact filter with axial connection to waveguide ports. However, the compact structure leads to small bandwidth and increases the difficulty of fabrication. In order to increase the bandwidth, a new coupling structure has been introduced. The bandwidth is increased successfully.

The designs of three-dimensional (3D) printed filters are also presented in this thesis. 3D printing presents attractive benefits such as flexibility in structural and material selection. In contrast to filters fabricated by conventional milling technologies, these two 3D printed filters can be manufactured in a single piece without assembly. To take advantage of the flexibility in structural selection, bent, twisted and triangular resonators are analyzed and applied on the filter. Bend and twist structure can change port orientation and polarization, respectively. In traditional, to realize port orientation and polarization, two components are needed. However, the twist waveguide filter in this thesis can be considered as integration of filtering and polarization change. 3D

printing shows great potential for the devices working at 60 GHz or higher frequency. However, the fabrication still requires external support structures to avoid overhang structure. These additional support structures will be no longer needed if the resonators are triangular with appropriate angle range. Therefore, the waveguide filter with triangular resonators are designed. The results show that the triangular resonator can realize self-supporting structure and no more additional internal supporting structure are needed. Because the structure of filter is raised to make sure the filter port is on the middle of the flange, external support structure is still needed under the filter. But it is a relatively easy support structure and requires less support materials.

# Acknowledgements

I would like to express my sincerest gratitude to Professor Yi Wang and Michael J. Lancaster for the patient supervising and continuous support during my PhD study at the University of Birmingham. Every report with comments is precious to me. Without their assistance and encouragement, the work presented in this thesis may never have been accomplished. I am also grateful to my co-supervisor Qingfeng Zhang for his useful advices and assistance on my PhD work.

My appreciation also goes to my colleagues, Dr Yang Yu and Dr Cheng Guo for their encouragement and useful suggestions. In particular, I would like to thank Dr. Talal Skaik for many useful assistances on the filter fabrication. I would like to extend thanks to my colleagues in the Emerging Device Technology Research Group at the University of Birmingham and the colleagues in the group at SUSTech. My great gratitude goes to all my friends and family for their accompany, support and encouragement.

# CONTENTS

Chapter 1 Introduction .....	1
1.1 Background and motivation .....	1
1.2 Novelty and contribution to knowledge of the thesis .....	4
1.3 Thesis overview .....	5
Chapter 2 Fundamental Filter theories.....	7
2.1 Overview of Filter.....	7
2.2 Transfer Functions .....	8
2.3 Lowpass Prototype Filter .....	10
2.4 Immittance Inverters .....	10
2.5 Element Transformations .....	12
2.6 Coupled-Resonator Circuits.....	15
2.6.1 General coupling matrix .....	15
2.6.2 Electric and magnetic coupling.....	19
2.7 Summary.....	24
Chapter 3 WR-1.5 waveguide bandpass filter .....	25
3.1 Design of the 3 <sup>rd</sup> order waveguide filter .....	25
3.2 Calculation of external quality factors.....	27
3.3 Calculation of inter-resonator couplings coefficients .....	29
3.4 Simulation and sensitivity analysis.....	30
3.4.1 Simulation results.....	30
3.4.2 Sensitivity analysis.....	31
3.5 Fabrication and measurement .....	35
3.6 Yield analysis .....	38
3.7 Summary.....	40

Chapter 4 Folded Waveguide Bandpass Filter .....	41
4.1 Introduction.....	41
4.2 Design of the original <i>X</i> band folded filter-I.....	42
4.3 Connection with steps .....	49
4.4 Improved <i>X</i> band folded filter-II.....	52
4.4.1 Design of the filter .....	52
4.4.2 Fabrication and Measurement.....	57
4.4.3 Tuning and measurement .....	60
4.5 Design of the WR-1.5 band folded filter.....	63
4.6 Summary .....	69
Chapter 5 3D printed bent and twisted filters at U/V-band.....	70
5.1 Introduction.....	70
5.2 Resonators.....	71
5.2.1 Resonators bent in the H-plane .....	71
5.2.2 Resonators bent in the E-plane .....	74
5.2.3 Twisted resonators.....	77
5.3 U band waveguide bandpass filter .....	80
5.3.1 Design of the twist filter .....	80
5.3.2 Twist filter with different bent angle.....	83
5.3.3 Different twist angles of each cavity.....	85
5.3.4 Suppress the spurious modes .....	86
5.4 V band waveguide bandpass filter .....	89
5.4.1 Design and measurement .....	90
5.4.2 Analysis of internal surface roughness .....	93

5.5 Summary .....	95
Chapter 6 Triangular resonators and waveguide bandpass filters.....	96
6.1 Triangular resonators .....	97
6.2 Design of the 2 <sup>nd</sup> order BPF .....	102
6.3 Design of the 3 <sup>rd</sup> order BPF .....	103
6.4 Fabrication and measurement .....	105
6.5 Summary .....	107
Chapter 7 Conclusion and future work .....	109
7.1 Conclusion .....	109
7.2 Future work.....	110
Reference .....	111
PUBLICATIONS .....	116



# Chapter 1 Introduction

## 1.1 Background and motivation

With the rapid development of wireless communication systems, the quality and efficiency of communication are being constantly improved. More stringent design requirements for wireless system components are raised. The design of filters requires low insertion loss, compact size, easy processing and low cost. There are many different physical structures to implement the function of filtering, like common microstrip lines (planar structure) [1]- [4], substrate integrated waveguide (SIW) [5]- [7] and waveguide [8]- [10]. Planar microstrip filters have been widely concerned and developed, because of their low cost, mature processing technology and ease of integration with chips. However, the planar filter has its own shortcomings, such as relatively large insertion loss, being susceptible to radiation loss, and low power capacity. Waveguide filter offers brilliant performance in some demanding fields, for example, in aerospace, satellite navigation, defense and other systems requiring high power. Low insertion loss, high  $Q$  value and large power capacity are the main advantages of waveguide structures. In this thesis, waveguide structures are used for all filters.

In recent years, fabrication of small rectangular waveguide components, working at millimeter-wave and terahertz, has received considerable attention. Increase of the frequency leads to the decrease in size hence high precision is needed in the process of

fabrication. For example, at 600 GHz the size of the standard waveguide is 0.1908mm  $\times$  0.38 mm. Many different machining technologies have been developed and employed to achieve high precision in the fabrication of the components. In [11]– [14], silicon deep reactive ion etching (DRIE) is employed and the operation frequency has been pushed to 1.033 THz [11]. The exploration of SU-8 photoresist technology [15] [16] [17] has been pushed into WR 1.5 band. In [17], a 3<sup>rd</sup> order filter which has 0.65 dB insertion loss and a 7.91% (53.1 GHz) bandwidth is demonstrated. It shows advantages of excellent low insertion losses, and high fabrication accuracy of SU-8. However, the multiple layer processes are complex and high-accuracy fixtures must be manufactured to make the connection with other standard waveguides. This causes additional loss and mismatch problems. Computer numerically controlled (CNC) milling is a traditional machining technology to fabricate metal waveguide components, especially at lower frequencies. Waveguide filters fabricated by CNC milling with excellent performance have been reported in [15] and [18]– [21]. [21] describes a 4<sup>th</sup> order WR 2.8-band filter which has 0.6 dB insertion loss and a 5.29% (17.99 GHz) bandwidth. Fabricating waveguide filters at such a frequency is limited by tool sizes and depth-to-diameter aspect ratios. Normally, the depth, the drill can realize, is three times of the diameter of the drill. Because of the limitation of conventional CNC milling, it is difficult to find many works in WR 1.5 band or above. Most of work are based on DRIE technique and SU-8 photoresist technology. Table 1.1 shows the comparison of recently published waveguide bandpass filters operating in frequency range from WR4 to WR 1.0 band.

**Table 1** Comparison of recently published waveguide bandpass filters operating in frequency range from WR 4 to WR 1.0 band.

Waveguide band	$f_0$ (GHz)	FBW (%)	Micromachining techniques	Filter responses	$n$	$IL$ (dB)	$RL$ (dB)	Reference (year)
WR-1.5	570	8.77%	DRIE (two pieces)	Chebyshev, no TZ	3	0.9	> 10	[11] (2012)
WR-1.5	640	6.25%	DRIE (two pieces)	Chebyshev, no TZ	4	2.5	> 9	[12] (2013)
WR-1.5	650	1.6%	DRIE (one etched and one cover)	Chebyshev, (one TZ at lower stopband and one at upper stop band)	4	2.18	> 18.42	[13] (2016)
WR-1.0	1033	2.1%	DRIE (one etched and one cover)	Chebyshev, no TZ	4	3.4	> 8	[14] (2017)
WR-3	298.6	5.36%	SU-8 (three layers)	Chebyshev, (three TZs at upper stopband)	3	0.45	> 16	[15] (2018)
WR-3	309.35	4.4%	SU-8 (three layers)	Chebyshev, (one TZ at lower stopband)	3	0.4	> 15	[16] (2013)
WR-1.5	671	7.91%	SU-8 (three layers)	Chebyshev, (one TZ at lower stopband)	3	0.65	> 11	[17] (2013)
WR-4	214.3	9.8%	CNC milling	quasi-elliptical (one TZ at lower stopband and one at upper stop band)	4	0.6	> 15	[18] (2017)
WR-3	255	13.3%	CNC milling	Chebyshev, no TZ	4	3.9	> 15	[19] (2015)
WR-3	257.7	8.77%	CNC milling	quasi-elliptical (one TZ at lower stopband and one at upper stop band)	4	0.7	> 14	[20] (2017)
WR-3	286.6	5.58%	CNC milling	Chebyshev, one TZ at upper stopband	3	0.41	> 14	[15] (2018)
WR-2.8	340	5.29%	CNC milling	Chebyshev, no TZ	4	0.6	> 20	[21] (2018)
WR-1.5	673.5	8.76%	CNC milling	Chebyshev, no TZ	3	0.5	> 14	My work

Compared with conventional micromachining technologies, additive manufacturing technologies, or 3D printing, shows promising performance in fabricating irregular shapes. Many different devices have been designed and fabricated using 3D printing techniques, such as SLA (Stereo-Lithography), SLS (Selective Laser Sintering) and FDM (Fused Deposition Modeling). SLA and SLS use laser to solidify liquid photopolymer resin or material powder. The main advantages of the SLA are its high resolution, and smooth surface roughness [22]. However, the SLA-printed devices require further metallization, which has an effect on the performance. FDM works by depositing melted plastic from a nozzle. Compared with the SLA and SLS, FDM is the least expensive technology, but it also has the worst resolution [22]. The SLM technique, also known as SLS, is widely used for fabricating metal parts from metal powders. It is also known as micro laser sintering (MLS) when micro-parts are fabricated. The twist

filter in this thesis was manufactured by MLS.

In this thesis, we will present the precision of commercial CNC milling has been improved and it is still a competitive solution to manufacturing sub-millimeter dimension waveguide structures in WR 1.5 band. A 3<sup>rd</sup> order WR 1.5 band waveguide bandpass filter is designed and fabricated. The waveguide filters with novel structures based on CNC milling still have great potentiality. To reduce the footprint of the usually bulky waveguide filters, a folded structure is presented in this work, which makes the whole filter structure more compact. To take advantage of the 3D printing technique's flexibility in manufacture, the performance of different resonators (twist and bent) are analyzed. A twist waveguide filter is designed, which integrates the filtering function and polarization rotation. To investigate the great potential of 3D printing for the devices working at 60 GHz or higher frequency, the tolerance and surface roughness are analyzed.

## **1.2 Novelty and contribution to knowledge of the thesis**

The novelty and main contribution of this thesis are:

- A WR-1.5 band (500-750 GHz) 3<sup>rd</sup> order waveguide bandpass filter is fabricated by high precision CNC machining. The results prove that the precision CNC milling is a viable technology for producing terahertz waveguide filters.
- A 4<sup>th</sup> order waveguide bandpass filters with a compact folded structure, allowing axial flange connections, are presented. A new coupling structure to increase the bandwidth has been applied. This folded structure enables highly compact waveguide filter with convenient flange connection and without sacrificing the

performance.

- Bent and twisted resonators are analyzed. A V band twist waveguide bandpass filter is designed and fabricated. Good results show the great potential of 3D printing for the devices working at 60 GHz or higher frequency.
- Triangular resonators are discussed. A X band waveguide bandpass filter with triangular resonators and irises is fabricated. The triangular resonator can realize self-supporting structure and no more additional internal supporting structure are needed.

### **1.3 Thesis overview**

This thesis includes 7 chapters. The work can be grouped into two parts: (i) computer numerically controlled (CNC) micromachined waveguide filters; (ii) 3D printed waveguide filters.

Chapter 1 contains the background of the research and the motivation. This is followed by the claim of novelty and contribution and the overview of the thesis.

Chapter 2 is devoted to the fundamental theories. It starts with a brief overview of filters. Following this, the transfer function is introduced in terms of mathematical description. Then the lowpass prototype filter, immittance inverters and elements transformation are introduced, in term of circuit. The last section is about the derivation of coupling matrix and electric (or magnetic) coupling.

Chapter 3 shows a WR-1.5 band (500-750 GHz) 3<sup>rd</sup> order waveguide bandpass filter, which has been designed and manufactured using high precision CNC metal micromachining.

Chapter 4 presents three 4<sup>th</sup> order waveguide bandpass filters with folded structure. The first two filters are working at 10 GHz. The bandwidth of the first filter is limited to the special folded structure. To increase the bandwidth, a new coupling structure is introduced and applied on the second filter. The third filter is design of a 660 GHz filter using the same folded structure.

Chapter 5 presents the performance of different bent and twist resonators. A 4<sup>th</sup> order V-band twist waveguide bandpass filter is designed and manufactured using micro laser sintering (MLS) technology. The analysis of the internal surface roughness is followed. In Chapter 6, the analysis and design of triangular resonators is reported. A 3 ploe-1-transmission zero filter with triangular cavities is designed and fabricated.

Publication and suggestions to the future work are presented at the end of this chapter.

# Chapter 2 Fundamental Filter theories

Basic concepts of filters and theories of coupling matrix are described in this Chapter. It starts with a brief overview of filter. Following this, transfer function is introduced. The mathematical description is presented. Then the lowpass prototype filter, immittance inverters and elements transformation are introduced. These are in term of circuit. The last section is about the derivation of coupling matrix and electric (or magnetic) coupling.

## 2.1 Overview of Filter

Filter is one key component in a communication system. It is used to transmit or select signals in specific frequency range. A filter can be considered as a two-port network, as shown in Figure 2.1 [24]. The wave variables  $a$  and  $b$  are introduced in Figure 2.1, where  $a$  denotes the incident waves and  $b$  denotes the reflected waves.

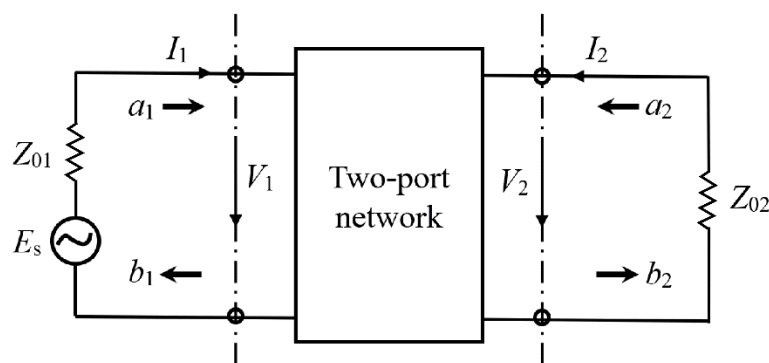


**Figure 2.1** Two-port network.  $Z_{01}$  ( $Z_{02}$ ) is the terminal impedance and  $E_s$  is the source voltage. The voltage and current are represented as  $V_1$  ( $V_2$ ) and  $I_1$  ( $I_2$ ), respectively.

The scattering parameters ( $S$  parameters) are defined in terms of the wave variables as

shown in Eq. (2.1) [24]. The parameter  $S_{11}$  and  $S_{22}$  are reflection coefficients. The parameter  $S_{21}$  and  $S_{12}$  is transmission coefficients.

$$\begin{aligned} S_{11} &= \left. \frac{b_1}{a_1} \right|_{a_2=0}, S_{12} = \left. \frac{b_1}{a_2} \right|_{a_1=0} \\ S_{21} &= \left. \frac{b_2}{a_1} \right|_{a_2=0}, S_{22} = \left. \frac{b_2}{a_2} \right|_{a_1=0} \end{aligned} \quad (2.1)$$

where  $a_n = 0$  means there is no reflection from port  $n$ .

The  $S$  parameters can be expressed as complex. Therefore,  $S_{mn} = |S_{mn}|e^{j\phi_{mn}}$  [25]. The amplitude  $|S_{mn}|$  can be defined in decibels (dB), that is  $20\log |S_{mn}|$  dB, where  $m, n= 1, 2$ .

The insertion loss  $L_A$  and the return loss  $L_R$  are defined as [25]

$$\begin{aligned} L_A &= -20 \log|S_{mn}| \quad \text{dB} \quad m, n = 1,2(m \neq n) \\ L_R &= -20 \log|S_{nn}| \quad \text{dB} \quad n = 1,2 \end{aligned} \quad (2.2)$$

The  $S$  parameters have some useful properties, like  $S_{11} = S_{22}$  and  $S_{12} = S_{21}$  for a symmetrical and reciprocal network [24]. If the network is lossless and passive, the sum of reflected power and the transmitted power should equal to the incident power [24]. That is to say,  $|S_{11}|^2 + |S_{21}|^2 = 1$ .

## 2.2 Transfer Functions

The transfer function is a mathematical expression of  $S_{21}$ . It is to describe the response characteristics in a mathematical way. The amplitude-squared transfer function for the Chebyshev response can be defined as [24]



$$|S_{21}(j\Omega)|^2 = \frac{1}{1 + \varepsilon^2 T_n^2(\Omega)} \quad (2.3)$$

where  $\varepsilon$  is ripple constant,  $T_n(\Omega)$  is characteristic function and  $\Omega$  is radian frequency variable.

If the transfer function is given, the insertion loss  $L_A$  can be expressed as

$$L_A(\Omega) = 10 \log \frac{1}{|S_{21}(j\Omega)|^2} \text{ dB} \quad (2.4)$$

Since  $|S_{11}|^2 + |S_{21}|^2 = 1$ , the reflection loss  $L_R$  can be expressed as

$$L_R(\Omega) = -10 \log[1 - |S_{21}(j\Omega)|^2] \text{ dB} \quad (2.5)$$

The ripple constant  $\varepsilon$  in Eq (2.3) is related to the passband ripple  $L_{Ar}$  (in dB) by

$$\varepsilon = \sqrt{10^{\frac{L_{Ar}}{10}} - 1}$$

If the minimum passband return loss is  $L_R$  dB, the passband ripple  $L_{Ar}$  can be defined by,

$$L_{Ar} = -10 \log(1 - 10^{0.1L_R}) \text{ dB} \quad (2.6)$$

$T_n(\Omega)$  is defined as

$$T_n(\Omega) = \begin{cases} \cos(ncos^{-1}\Omega), & |\Omega| \leq 1 \\ \cosh(ncosh^{-1}\Omega), & |\Omega| \geq 1 \end{cases} \quad (2.7)$$

A rational transfer function can be defined as

$$S_{21}(p) = \frac{N(p)}{D(p)} \quad (2.8)$$

where  $N(p)$  and  $D(p)$  are polynomials,  $p = \sigma + j\Omega$  and  $\sigma = 0$  for a lossless passive network.

The rational transfer function can be constructed by the amplitude-squared transfer function. The zeros of  $S_{21}(p)$  is the roots of  $N(p)$ . The poles of  $S_{21}(p)$  are the roots of  $D(p)$ . There are different types of functions, such as Butterworth (maximally Flat) response, Chebyshev response, Elliptic function response and so on.

### 2.3 Lowpass Prototype Filter

To realize the transfer function, low pass filter prototype is introduced here. Figure 2.2 presents two lowpass prototype of all-pole filter response [24]. There are no transmission zeros in this response.  $n$  is the filter order and the number of the reactive elements. The value of  $g_0$  is defined as 1 since the filter is normalized lowpass filter.  $g_i$  (for  $i = 1$  to  $n$ ) represents the inductance or the capacitance and  $g_{n+1}$  is the load resistance.

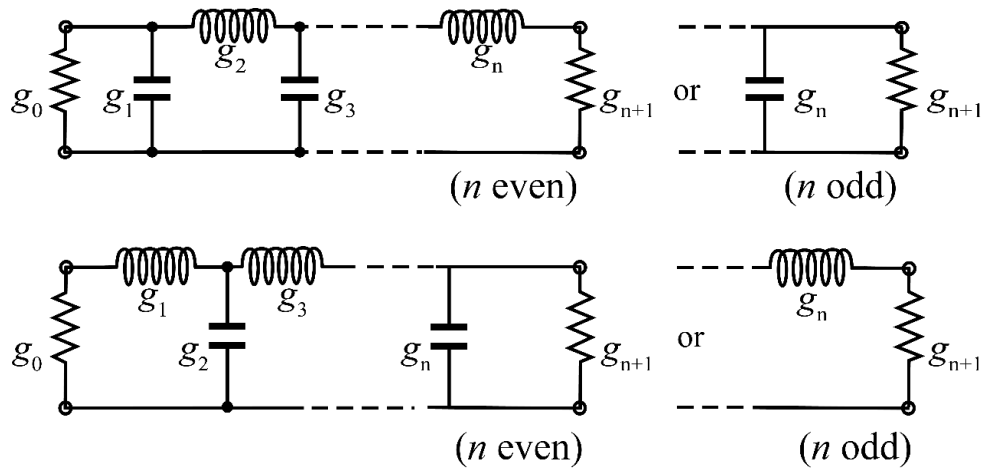


**Figure 2.2** Circuit ladder of lowpass prototype filters for all-pole filters with even order and odd order.

### 2.4 Immittance Inverters

Immittance inverters is introduced here. As we have seen in Figure 2.2, the circuit

ladder consists of shunt-connected capacitor and series-connected inductor. However, it is often desirable to use only series or only shunt elements in practical implementation [24]. This is the reason of employing the immittance inverters, which are used to convert the series-connected elements to shunt-connected elements, or vice versa. The immittance inverters include impedance inverters and admittance inverters.

The idealized impedance inverter ( $K$  inverter) is defined as [25]

$$Z_1 = \frac{K^2}{Z_2} \quad (2.9)$$

where  $Z_1$  is the impedance seen into the port and  $Z_2$  is the terminal impedance at another port.

The idealized admittance inverter ( $J$  inverter) is defined as [25]

$$Y_1 = \frac{J^2}{Y_2} \quad (2.10)$$

where  $Y_1$  is the admittance seen into one port and  $Y_2$  is the terminal admittance in another port.

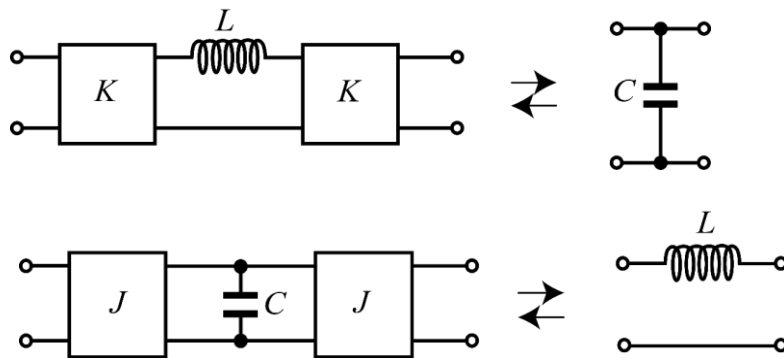


**Figure 2.3** The equivalent circuits of  $K$  and  $J$  inverters [25]

The equivalent circuits of  $K$  and  $J$  inverters are shown in Figure 2.3. The circuit ladder of Figure 2.2 can be converted to an equivalent circuit with inverters as shown in Figure 2.4 [25]. The equivalent forms use only series-connected inductor or shunt-connected capacitor, which are more convenient to implement using microwave structures. For instance, the immittance inverter can be constructed using quarter-wave transformer.

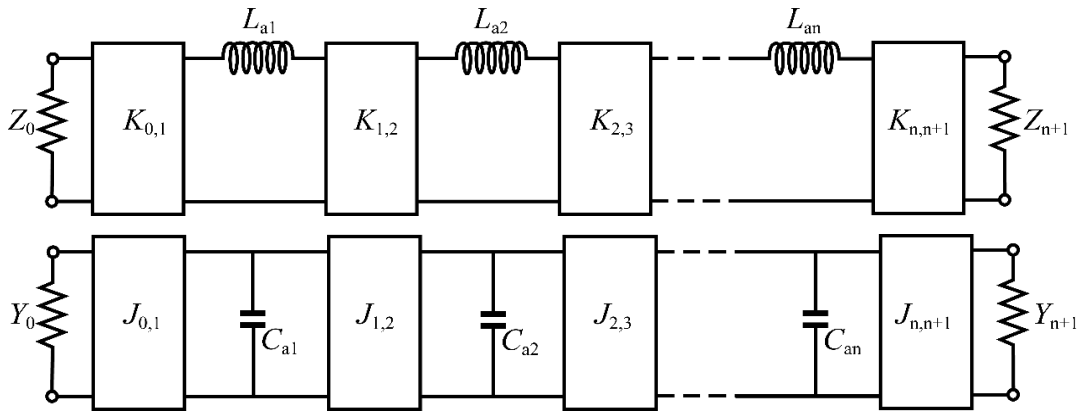


**Figure 2.4** The equivalent circuit with inverters for lowpass prototype filter.

The immittance inverter parameters  $K_{i,i+1}$  and  $J_{i,i+1}$  are specified as [25]

$$K_{0,1} = \sqrt{\frac{Z_0 L_{a1}}{g_0 g_1}}, K_{i,i+1} = \sqrt{\frac{L_{ai} L_{a(i+1)}}{g_i g_{i+1}}}, K_{n,n+1} = \sqrt{\frac{Z_{n+1} L_{an}}{g_n g_{n+1}}}$$

$$J_{0,1} = \sqrt{\frac{Y_0 C_{a1}}{g_0 g_1}}, J_{i,i+1} = \sqrt{\frac{C_{ai} C_{a(i+1)}}{g_i g_{i+1}}}, J_{n,n+1} = \sqrt{\frac{Y_{n+1} C_{an}}{g_n g_{n+1}}} \quad (2.11)$$

where the  $g_i$  values are the original prototype element values, as indicated earlier.

## 2.5 Element Transformations

The lowpass prototype filter is demonstrated in previous part. The elements values and

cutoff frequency are normalized, that is  $g_0 = 1$  and  $\Omega_c = 1$ . The other types of filters can be realized by transforming the lowpass filter. The transformation includes impedance scaling for the resistive elements and frequency transformation for the reactive elements.

The impedance scaling is by removing the normalization of resistive elements. The impedance scaling factor  $\gamma_0$  is defines as

$$\gamma_0 = \begin{cases} Z_0/g_0 & \text{for } g_0 \text{ being the resistance} \\ g_0/Y_0 & \text{for } g_0 \text{ being the conductance} \end{cases} \quad (2.12)$$

where  $Z_0$  and  $Y_0$  is source impedance and admittance, respectively.

The frequency transformation is mapping the frequency domain of the lowpass filter to a specified frequency domain of a practical filter such as a bandpass filter. The frequency transformation only affects the reactive elements. The resistive elements will not be affected.

If the lowpass filter is transformed to a bandpass filter, the frequency transformation is [24]

$$\Omega = \frac{\Omega_c}{FBW} \left( \frac{\omega}{\omega_0} - \frac{\omega_0}{\omega} \right) \quad (2.13)$$

where

$$FBW = \frac{\omega_2 - \omega_1}{\omega_0}$$

$$\omega_0 = \sqrt{\omega_1 \omega_2} \quad (2.14)$$

$\omega_0$  is the center frequency of the bandpass filter,  $\omega_1$  and  $\omega_2$  are the passband-edge frequency and  $FBW$  is the fractional bandwidth.

The lowpass prototype to bandpass transformation is shown in Figure 2.5. The inductive element in the lowpass filter can be converted to a series  $LC$  circuit in the bandpass filter. The capacitive element can be converted to a parallel  $LC$  circuit.

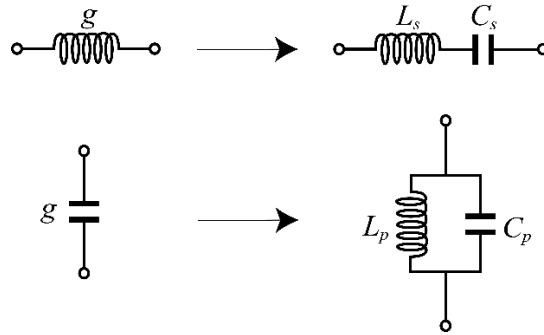


**Figure 2.5** The lowpass prototype to bandpass transformation.

The values of the elements in the bandpass filter in above figure are specified as

$$L_s = \left( \frac{\Omega_c}{FBW \omega_0} \right) \gamma_0 g$$

$$C_s = 1/(\omega_0^2 L_s)$$

$$C_p = \left( \frac{\Omega_c}{FBW \omega_0} \right) \frac{g}{\gamma_0}$$

$$L_p = 1/(\omega_0^2 C_p) \quad (2.15)$$

The circuit in Figure 2.4 can be easily transformed to bandpass filter using elements transformations. The bandpass prototype filter is shown in Figure 2.6.

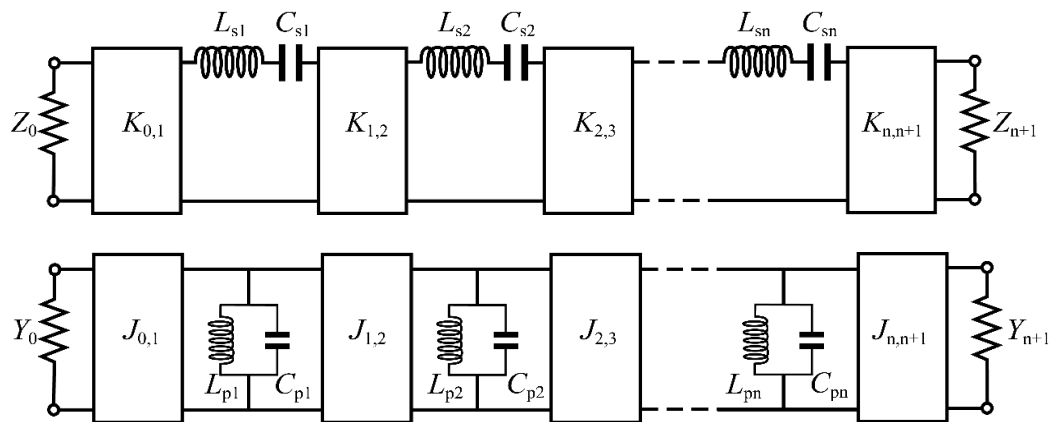


**Figure 2.6** The bandpass prototype filter

The immittance inverter parameters  $K_{i,i+1}$  and  $J_{i,i+1}$  of the bandpass filter in Figure 2.6 are specified as [25]

$$\begin{aligned}
K_{0,1} &= \sqrt{\frac{FBW \omega_0 L_{s1} Z_0}{\Omega_c g_0 g_1}}, K_{i,i+1} = \frac{FBW \omega_0}{\Omega_c} \sqrt{\frac{L_{si} L_{s(i+1)}}{g_i g_{i+1}}} \Big|_{i=1 \text{ to } n-1} \\
K_{n,n+1} &= \sqrt{\frac{FBW \omega_0 L_{an} Z_{n+1}}{\Omega_c g_n g_{n+1}}}, C_{si} = \frac{1}{\omega_0^2 L_{si}} \Big|_{i=1 \text{ to } n} \\
J_{0,1} &= \sqrt{\frac{FBW \omega_0 C_{p1} Y_0}{\Omega_c g_0 g_1}}, J_{i,i+1} = \frac{FBW \omega_0}{\Omega_c} \sqrt{\frac{C_{pi} C_{p(i+1)}}{g_i g_{i+1}}} \Big|_{i=1 \text{ to } n-1} \\
J_{n,n+1} &= \sqrt{\frac{C_{an} Y_{n+1}}{g_n g_{n+1}}}, L_{pi} = \frac{1}{\omega_0^2 C_{pi}} \Big|_{i=1 \text{ to } n}
\end{aligned} \tag{2.16}$$

## 2.6 Coupled-Resonator Circuits

Coupled-resonated circuits play a significant role in designing the RF/microwave filter. Coupling coefficients ( $k_c$ ) are introduced to represent the coupling between the coupled resonators. The coupling between the port and the adjacent resonator is defined as external quality factor ( $Q_e$ ). The general coupling matrix is introduced in 2.6.1. Some general theory of coupling is introduced in 2.6.2.

### 2.6.1 General coupling matrix

This part shows how to derive the general coupling matrix from loop equations. An uncoupled single resonator is shown in Figure 2.7. An equivalent circuit of  $n$ -coupled resonators is shown in Figure 2.8.  $n$  is the order number (the number of resonators).

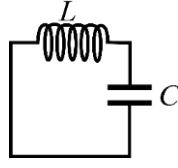


**Figure 2.7** An uncoupled single resonator.

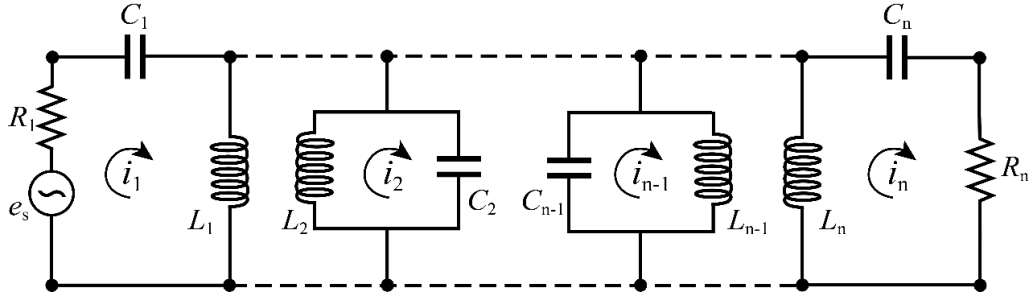


**Figure 2.8** Equivalent circuit of  $n$ -coupled resonators.  $R$ ,  $C$ ,  $L$  represents the resistance, capacitance, and inductance, respectively.  $i_n$  is the loop current and  $e_s$  is the source voltage.

Based on the sum of the voltage drops around any closed path in a network is zero (Kirchhoff's Law), the loop equations for the circuit in Figure 2.8 are as follows [24]

$$\begin{aligned}
 \left( R_1 + j\omega L_1 + \frac{1}{j\omega C_1} \right) i_1 - j\omega L_{12} i_2 \cdots - j\omega L_{1n} i_n &= e_s \\
 -j\omega L_{21} i_1 + \left( j\omega L_2 + \frac{1}{j\omega C_2} \right) i_2 \cdots - j\omega L_{2n} i_n &= 0 \\
 \dots & \\
 -j\omega L_{n1} i_1 - j\omega L_{n2} i_2 \cdots + \left( R_n + j\omega L_n + \frac{1}{j\omega C_n} \right) i_n &= 0 \quad (2.17)
 \end{aligned}$$

Convert the Eq. (2.17) to a matrix form



$$\begin{bmatrix} R_1 + j\omega L_1 + \frac{1}{j\omega C_1} & -j\omega L_{12} & \dots & -j\omega L_{1n} \\ -j\omega L_{21} & j\omega L_2 + \frac{1}{j\omega C_2} & \dots & -j\omega L_{2n} \\ \vdots & \vdots & \ddots & \vdots \\ -j\omega L_{n1} & -j\omega L_{n2} & \dots & R_n + j\omega L_n + \frac{1}{j\omega C_n} \end{bmatrix} \begin{bmatrix} i_1 \\ i_2 \\ \vdots \\ i_n \end{bmatrix} = \begin{bmatrix} e_s \\ 0 \\ \vdots \\ 0 \end{bmatrix} \quad (2.18)$$

or

$$[Z] \cdot [i] = [e]$$

where  $[Z]$  is the impedance matrix with  $n$  order.

When  $L = L_1 = L_2 = \dots = L_n$ ,  $C = C_1 = C_2 = \dots = C_n$  and  $\omega_0 = \sqrt{1/LC}$  for synchronously tuned filter [24],  $[Z]$  can be expressed as

$$[Z] = \omega_0 L \cdot FBW \cdot [\bar{Z}] \quad (2.19)$$

where  $[\bar{Z}]$  is the normalized impedance matrix.

$$[\bar{Z}] = \begin{bmatrix} \frac{R_1}{\omega_0 L \cdot FBW} + p & -j \frac{\omega}{\omega_0} \frac{L_{12}}{L} \cdot \frac{1}{FBW} & \dots & -j \frac{\omega}{\omega_0} \frac{L_{1n}}{L} \cdot \frac{1}{FBW} \\ -j \frac{\omega}{\omega_0} \frac{L_{21}}{L} \cdot \frac{1}{FBW} & p & \dots & -j \frac{\omega}{\omega_0} \frac{L_{2n}}{L} \cdot \frac{1}{FBW} \\ \vdots & \vdots & \ddots & \vdots \\ -j \frac{\omega}{\omega_0} \frac{L_{n1}}{L} \cdot \frac{1}{FBW} & -j \frac{\omega}{\omega_0} \frac{L_{n2}}{L} \cdot \frac{1}{FBW} & \dots & \frac{R_n}{\omega_0 L \cdot FBW} + p \end{bmatrix} \quad (2.20)$$

where

$$p = j \frac{1}{FBW} \left( \frac{\omega}{\omega_0} - \frac{\omega_0}{\omega} \right) \quad (2.21)$$

The external quality factors  $Q_{e1}$  and  $Q_{en}$  are defined as

$$\frac{R_i}{\omega_0 L} = \frac{1}{Q_{ei}} \quad \text{for } i = 1, n \quad (2.22)$$

The scaled external quality factors are defined as

$$q_{ei} = Q_{ei} \cdot FBW \quad \text{for } i = 1, n \quad (2.23)$$

The coupling coefficients are defined as

$$M_{ij} = \frac{L_{ij}}{L} \quad (2.24)$$

Defining the normalized coupling coefficients as

$$m_{ij} = \frac{M_{ij}}{FBW} \quad (2.25)$$

Assume  $\omega/\omega_0 \approx 1$  for a narrow-band approximation. Substituting Eq. (2.23-2.25) into Eq. (2.20), it can be simplified as

$$[\bar{Z}] = \begin{bmatrix} \frac{1}{q_{e1}} + p & -jm_{12} & \cdots & -jm_{1n} \\ -jm_{21} & p & \cdots & -jm_{2n} \\ \vdots & \vdots & \ddots & \vdots \\ -jm_{n1} & -jm_{n2} & \cdots & \frac{1}{q_{en}} + p \end{bmatrix} \quad (2.26)$$

The  $S$  parameters can be obtained by network analysis of Figure 2.8 [24].

$$S_{21} = 2 \frac{1}{\sqrt{q_{e1} \cdot q_{en}}} [\bar{Z}]_{n1}^{-1}$$

$$S_{11} = 1 - \frac{2}{q_{e1}} [\bar{Z}]_{11}^{-1} \quad (2.27)$$

For asynchronously tuned circuit, the resonating frequencies of different resonators are different. Eq. (2.26) is transformed to [24]

$$[\bar{Z}] = \begin{bmatrix} \frac{1}{q_{e1}} + p - jm_{11} & -jm_{12} & \cdots & -jm_{1n} \\ -jm_{21} & p - jm_{22} & \cdots & -jm_{2n} \\ \vdots & \vdots & \ddots & \vdots \\ -jm_{n1} & -jm_{n2} & \cdots & \frac{1}{q_{en}} + p - jm_{nn} \end{bmatrix} \quad (2.28)$$

Therefore, the general expression of  $S$  parameters is

$$S_{21} = 2 \frac{1}{\sqrt{q_{e1} \cdot q_{en}}} [A]_{n1}^{-1}$$

$$S_{11} = \pm \left( 1 - \frac{2}{q_{e1}} [A]_{11}^{-1} \right) \quad (2.29)$$

where

$$[A] = [q] + p[U] - j[m] \quad (2.30)$$

$[U]$  is an  $n \times n$  unit matrix,  $[q]$  is an  $n \times n$  matrix with all entries zero, except for  $q_{11} = 1/q_{e1}$  and  $q_{nn} = 1/q_{en}$ , and  $[m]$  is an  $n \times n$  general coupling matrix [24].

## 2.6.2 Electric and magnetic coupling

Coupling coefficients have different signs. The positive sign means the stored energy is enhanced, while the negative sign implies the stored energy is reduced. Coupling between the resonators might be resistive coupling, electric coupling, magnetic coupling or mixed coupling. In the following, electric coupling and magnetic coupling are introduced and distinguished.

For an uncoupled single resonator, we have

$$\frac{1}{j\omega C} + j\omega L = 0 \quad (2.31)$$

Hence, the resonant frequency  $f$  of the single resonator is

$$f = \frac{\omega}{2\pi} = \frac{1}{2\pi} \cdot \frac{1}{\sqrt{LC}} \quad (2.32)$$

A synchronously tuned circuit with electric coupling is shown in Figure 2.9 (a). Using an admittance inverter  $J = \omega C_m$  to represent the coupling, the equivalent circuit is shown in Figure 2.9 (b) [24].

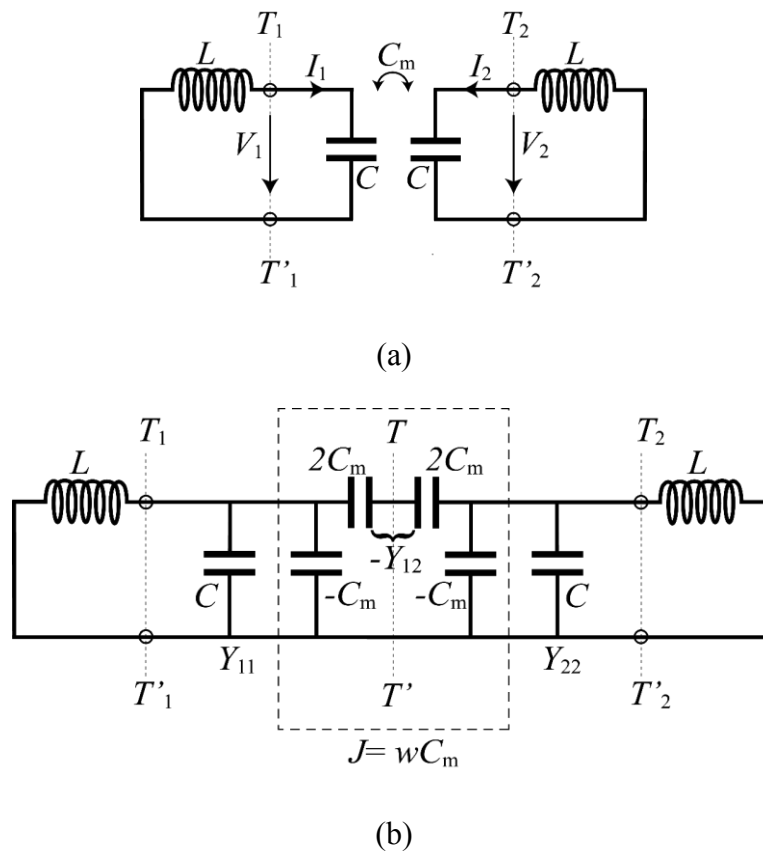


**Figure 2.9** (a) A synchronously tuned circuit with electric coupling and (b) its equivalent circuit.

If the plane T-T' in Figure 2.9 (b) is changed to an electric wall, which means short circuit, we will have

$$\frac{1}{j\omega(C + 2C_m - C_m)} + j\omega L = 0 \quad (2.33)$$

Therefore, the resonating frequency  $f_e$  is

$$f_e = \frac{1}{2\pi\sqrt{L(C + C_m)}} \quad (2.34)$$

which is smaller than the value of  $f$  in Eq. (2.32).

If the symmetry plane T-T' in Figure 2.9b is changed to a magnetic wall, which means open circuit, we will have

$$\frac{1}{j\omega(C - C_m)} + j\omega L = 0 \quad (2.35)$$

Therefore, the resonate frequency  $f_m$  is

$$f_m = \frac{1}{2\pi\sqrt{L(C - C_m)}} \quad (2.36)$$

which is larger than the value of  $f$  in Eq. (2.32).

Based on Eq. (2.34) and Eq. (2.36), the electric coupling coefficient  $k_E$  can be expressed as [24]

$$k_E = \frac{f_m^2 - f_e^2}{f_m^2 + f_e^2} = \frac{C_m}{C} \quad (2.37)$$

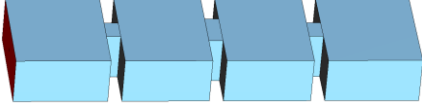
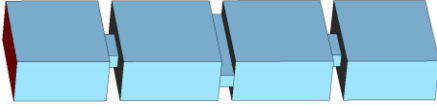
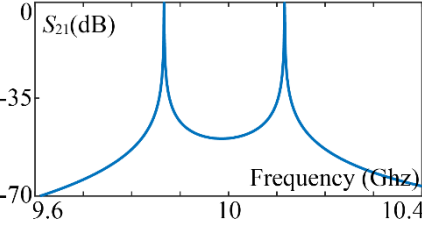
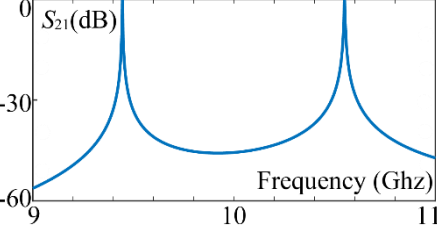
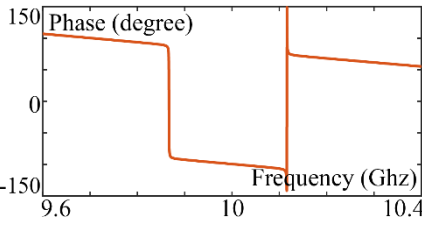
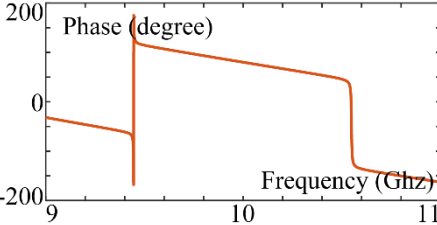
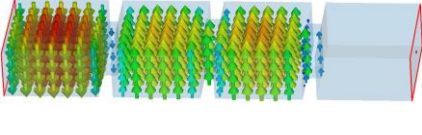
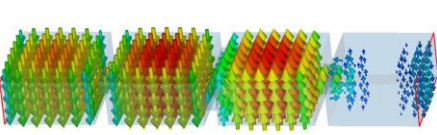
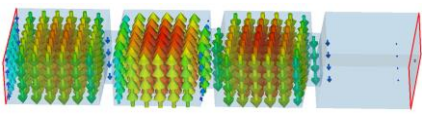
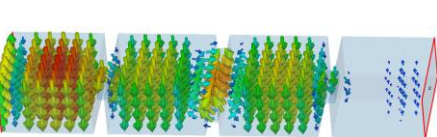
As stated above,  $f_e < f_m$  for electric coupling. However,  $f_m < f_e$  for magnetic coupling. The process of derivation is similar to previous process. The magnetic coupling coefficient  $k_M$  is stated as

$$k_M = \frac{f_e^2 - f_m^2}{f_e^2 + f_m^2} = \frac{L_m}{L} \quad (2.38)$$

The superposition of both the magnetic and electric couplings leads to mixed coupling. The magnetic and electric couplings might enhance each other or cancel each other.

In physical implementation, the resonating frequency is found by simulating the adjacent coupled resonators. To distinguish electric coupling and magnetic coupling between the adjacent resonators, simple waveguide structures using inductive/capacitive iris are simulated in CST as shown in the first row of Table 2.1. The two resonant peaks in the simulated  $S_{21}$  are the two resonating frequencies, which are proved to be  $f_m$  and  $f_e$ . Electric coupling and magnetic coupling show reverse phase performance as shown in the third row of Table 2.1. Furthermore, for the magnetic coupling, the electric fields in the two resonators have the same direction (in phase) at the lower resonant frequency and opposite direction (out of phase) at the upper resonant frequency. In other words,  $f_{even}$  is lower than  $f_{odd}$  for magnetic coupling as shown in the fourth row of Table 2.1. However,  $f_{even}$  is higher than  $f_{odd}$  for electric coupling.

**Table 2.1** Comparison between waveguide magnetic coupling and electric coupling

	Magnetic coupling	Electric coupling
Structure	 <p>(Inductive iris)</p>	 <p>(Capacitive iris)</p>
$S_{21}$		
Phase of $S_{21}$		
Electric field	 <p>(at 9.8853 GHz, in phase, even mode)</p>	 <p>(at 9.4329 GHz, out of phase, odd mode)</p>
	 <p>(at 10.123 GHz, out of phase, odd mode)</p>	 <p>(at 10.481 GHz, in phase, even mode)</p>
	$f_{even} < f_{odd}$	$f_{odd} < f_{even}$

## **2.7 Summary**

In this chapter, concepts of filters are expressed in several ways - mathematical description, circuit implementation and coupling matrix. The circuits and coupling matrix are the base for the design of filters. Different type physical structure can be employed to realize the filtering after knowing the coupling matrix. Filter designing example will be given in the next Chapter to illustrate the application of the coupling matrix approach.



# Chapter 3 WR-1.5 waveguide bandpass

## filter

In this Chapter, a WR-1.5 band (500-750 GHz) 3<sup>rd</sup> order waveguide bandpass filter has been designed and manufactured using high-precision computer numerically controlled (CNC) metal machining. The comparison between different fabrication technologies and the advantages of CNC were discussed in Chapter 1. This filter is used as a prototype to find the precision of commercial CNC milling machine. Section 3.1 is devoted to present the design of the 3<sup>rd</sup> order waveguide filter. Section 3.2 and Section 3.3 present the method to extract the external quality factor ( $Q_e$ ) and the coupling coefficients ( $\kappa_c$ ) from EM simulation, respectively. Section 3.4 shows the simulation results. The sensitivity analysis is also presented. Section 3.5 describes the fabrication and measurement of this filter. The following Section 3.6 reports yield analysis of this filter. The final Section 3.7 is summary.

### 3.1 Design of the 3<sup>rd</sup> order waveguide filter

In the following, a 3<sup>rd</sup> order waveguide filter is designed as an example. The diagram of the filter structure is shown in Figure 3.1. There are three coupled resonators operating in the TE<sub>101</sub> mode. All the couplings are realized via inductive irises. The curved corner should be taken into consideration, because the corners of cavities cannot be at right angle for CNC milling. The radius of milling cutter is 0.05 mm, which is the

smallest size provided by the manufacturer. Therefore, the resonators in Figure 3.1 have round corners with 0.05 mm radius.

This filter is designed using the coupling matrix approach described in Chapter 2. It is designed to have a Chebyshev response with a center frequency of 660 GHz, a fractional bandwidth of 5 %. The passband ripple  $L_{Ar}$  is 0.043dB. The frequency band was chosen based on the requirements for a high-precision radar application.

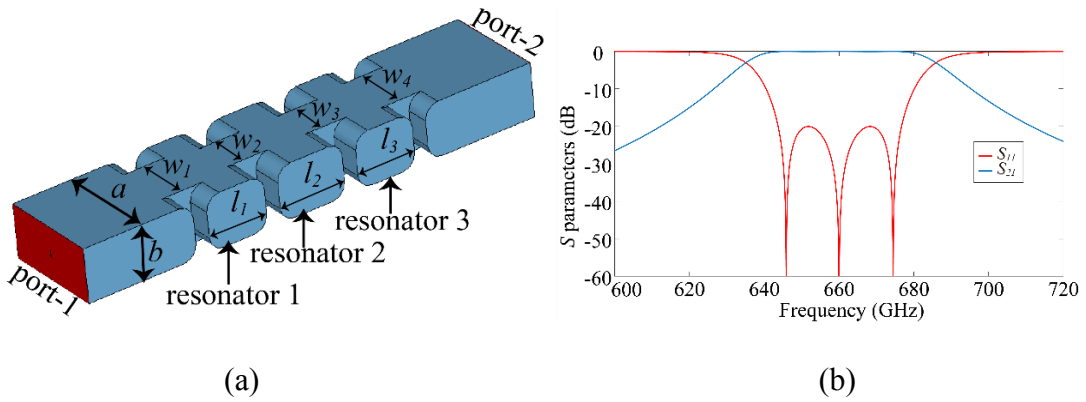


**Figure 3.1** (a) The air model of the 3<sup>rd</sup> order filter ( $a= 0.381$  mm,  $b= 0.1905$  mm). (b) Ideal responses of this bandpass filter from coupling matrix.

According to the equation in previous chapter, the external quality factor ( $Q_e$ ) and coupling matrix  $M_{n \times n}$  are:

$$Q_{e1} = Q_{e3} = 17.0316,$$

$$M = \begin{bmatrix} 0 & M_{12} & 0 \\ M_{21} & 0 & M_{23} \\ 0 & M_{32} & 0 \end{bmatrix} = \begin{bmatrix} 0 & 0.0516 & 0 \\ 0.0516 & 0 & 0.0516 \\ 0 & 0.0516 & 0 \end{bmatrix} \quad (3.1)$$

Due to the symmetry of the structure, the external quality factors at two ports are the same as shown in Eq. (3.1). Furthermore, the coupling coefficients  $M_{12}$  and  $M_{23}$  are

equal, which means the coupling at these two irises are the same. The iris between the waveguide port and the adjacent resonator controls the external quality factor ( $Q_e$ ). The iris between resonators 1 and 2 (or resonators 2 and 3) controls the coupling coefficient  $k_{c12}$  (or  $k_{c23}$ ). Section 3.2 and 3.3 present the method of extracting  $Q_e$  and  $k_c$  in full-wave electromagnetic (EM) simulation.

### 3.2 Calculation of external quality factors

The width of the input/output coupling irises ( $w_1$  or  $w_4$ ) are determined by simulating the first resonator (or the third resonator) as shown in Figure 3.2 (a).

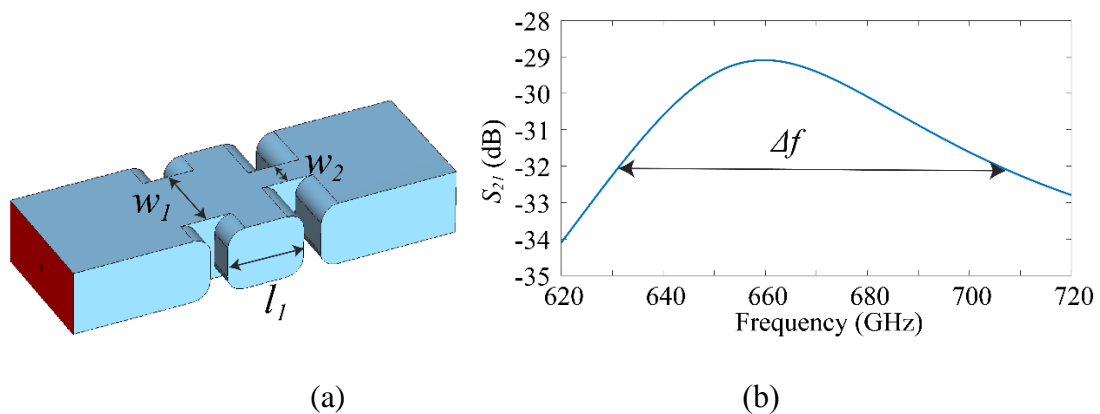


**Figure 3.2** (a) The air model of the first resonator. (b)  $S_{21}$  of the structure shown in (a).

Coupling on the one side must be weak coupling. Therefore, the value of  $w_2$  is set as 0.08 mm to make sure the weak coupling.  $w_1$  is adjusted to control the input coupling. The center frequency  $f_0$  of the passband can be moved to 10 GHz by adjusting the length of the resonator ( $l_1$ ) as shown in Figure 3.2 (b). The external quality factor can be calculated from

$$Q_e = \frac{f_0}{\Delta f} \quad (3.2)$$

$\Delta f$  is the 3 dB-bandwidth which can be obtained directly from Figure 3.2 (b). Each value of  $w_1$  corresponds to an external quality factor  $Q_e$ . Table 3.1 shows the relationship between  $w_1$  (or  $w_4$ ) and  $Q_e$ . The relationship can be seen clearly in Figure 3.3.

**Table 3.1** The relationship between  $w_1$  (or  $w_4$ ) and  $Q_e$ .

$w_1(w_4)$ (mm)	0.196	0.198	0.200	0.205	0.210	0.212
$BW$ (GHz)	28.15	29.50	33.72	39.35	46.71	49.93
$f_0$ (GHz)	660.63	660.1	661.06	659.95	659.71	661.1
$Q_e$	28.58	23.16	20.62	16.77	14.13	13.25

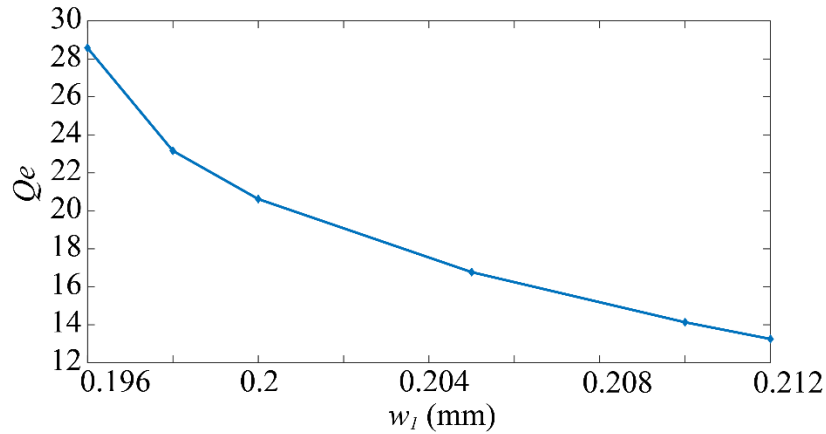


**Figure 3.3** The relationship between  $w_1$  (or  $w_4$ ) and  $Q_e$ .

### 3.3 Calculation of inter-resonator couplings coefficients

The inter-resonator coupling is mainly controlled by the iris between the adjacent two resonators. The value of  $w_2$  ( $w_3$ ) are determined by simulating the first and the second resonators as shown in Figure 3.4 (a). The values of  $w_1$  and  $w_3$  is designed as 0.08 mm to make sure the coupling from the feed port is weak coupling. The center frequency  $f_0 = (f_1 + f_2)/2$  should be kept as 10 GHz. The coupling coefficient  $k_{c12}$  ( $k_{c23}$ ) can be calculated from

$$k_c = \frac{f_2^2 - f_1^2}{f_2^2 + f_1^2} \quad (3.3)$$

$f_1$  and  $f_2$  are the two resonant peaks as shown in Figure 3.4 (b). The relationship between  $k_{c12}$  ( $k_{c23}$ ) and  $w_2$  ( $w_3$ ) is shown in Table 3.2 and Figure 3.5.

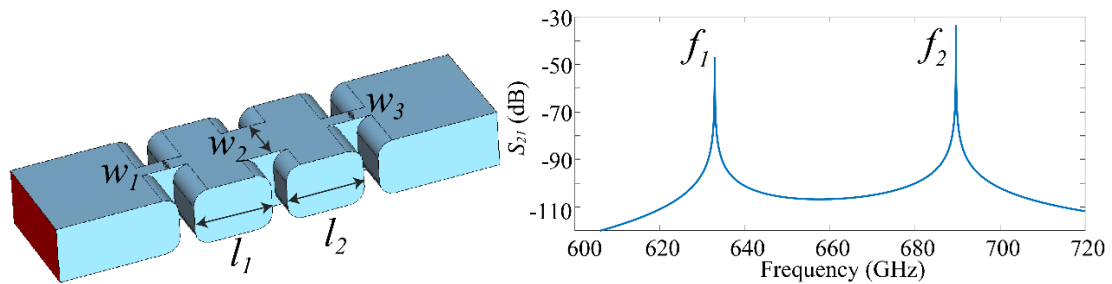


**Figure 3.4** (a) The model of the second and the third resonators. (b)  $S_{21}$  of the structure shown in (a).

**Table 3.2** The relationship between  $k_{c12}$  ( $k_{c23}$ ) and  $w_2$  ( $w_3$ ).

$w_2(w_3)$ (mm)	0.151	0.152	0.153	0.1535	0.154	0.155
$f_1$ (GHz)	676.7	676.91	676.944	677.016	642.648	644.97
$f_2$ (GHz)	644.45	643.94	643.152	642.912	677.28	681.14
$f_0$ (GHz)	659.3	659.11	660.048	659.964	659.96	661.49
$k_{c12}$ ( $k_{c23}$ )	0.0488	0.0499	0.05116	0.05164	0.05244	0.0545

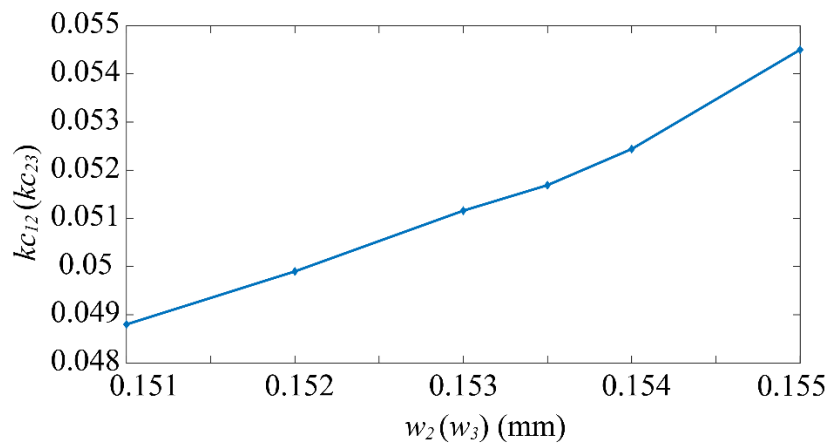


**Figure 3.5** The relationship between  $k_{c12}$  ( $k_{c23}$ ) and  $w_2$  ( $w_3$ ).

### 3.4 Simulation and sensitivity analysis

#### 3.4.1 Simulation results

The initial values of all parameters can be estimated from Figure 3.3 and Figure 3.5 as shown in the first row of Table 3.3. Full-wave simulation and optimization are carried out by CST Microwave Studio. The optimized dimensions of the filter are given in the second row of Table 3.3.

**Table 3.3** Initial and optimized values of all parameters in the filter.

<b>Dimensions</b>	$w_1$ ( $w_4$ )	$w_2$ ( $w_3$ )	$l_2$ ( $l_4$ )	$l_3$
<b>Initial (mm)</b>	0.2047	0.1534	0.2139	0.24
<b>Optimized (mm)</b>	0.2051	0.1519	0.2131	0.2414

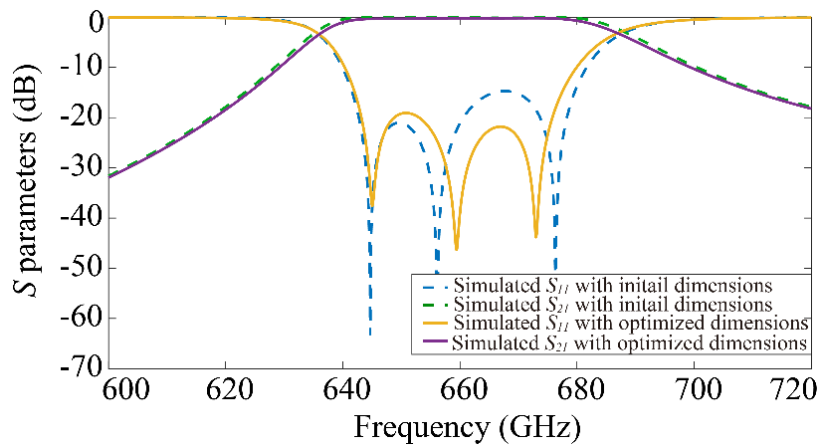


**Figure 3.6** The comparison between the initial results and the optimized results.

The comparison between the initial results and the optimized results is shown in Figure 3.6. The filter is electroplated in gold with a nominal conductivity of  $4.10 \times 10^7$  S/m used in the optimized simulation. The optimized filter is centered at 661.5 GHz with a 7.56 % 3-dB bandwidth (50.01 GHz). The maximum return loss is 19.1 dB, and the minimum insertion loss is 0.23 dB.

### 3.4.2 Sensitivity analysis

The design of the waveguide filter is presented in the above Sections. Because of the high frequency, the filter is sensitive to small manufacturing tolerance. Therefore,

sensitivity analysis before the fabrication is very necessary for the filter working in Terahertz. Sensitivity of  $S$  parameters with respect to changes of a model parameter  $p$  can be defined as [26]

$$sensitivity = \frac{\partial S}{\partial p} \approx \frac{\Delta S}{\Delta p} = \frac{S(p+\Delta p) - S(p)}{\Delta p} \quad (3.4)$$

The sensitivity helps estimate new  $S$  parameters due to the small changes of the parameter. Suppose the model parameter  $p$  changes by a small quantity  $\Delta p$ , equation (3.5) can be considered a reasonable approximation, which is equivalent to the 1<sup>st</sup> order Taylor expansion.

$$S(p+\Delta p) = S(p) + sensitivity \cdot \Delta p \quad (3.5)$$

Traditional approaches require multiple 3D simulations to derive the various parameter dependencies. A sensitivity analysis is implemented in CST MWS transient solver. The newly implemented sensitivity analysis will be capable of evaluating the  $S$  parameter dependencies on various model parameters based on one simulation in CST MWS transient solver. All further evaluations for different model parameters can be derived without redoing the full-wave simulation. The first step of the sensitivity analysis in CST is to pick faces and define face constrains in tool dialog, the second step is active the sensitivity analysis in solver dialog. The following analysis is based on the sensitivity analysis in CST.

In the process of manufacturing, the milling cutter is vertical to the split plane (E-plane). This is illustrated in Figure 3.7. The cutter moves in X, Y, Z direction to mill the depth, height, and length of the cavity, respectively.



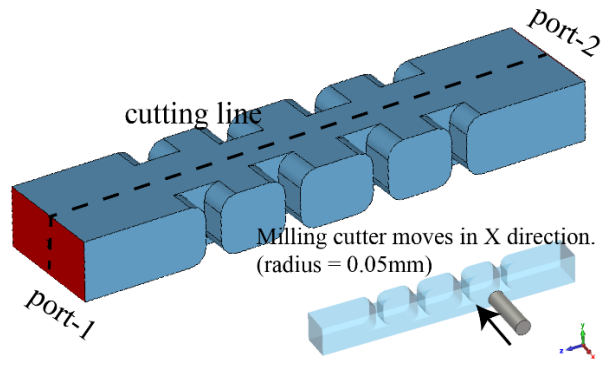


**Figure 3.7** Filter with cutting line and half of filter. (The milling cutter moves in X direction which refers to milling depth.)

If the perturbation tolerance for each depth in X direction is represented by parameter  $D_1$ - $D_{14}$ . Each parameter represents the displacement in X direction of the specified face, including the iris face and the cavity face. The parameters are presented in Figure 3.8.

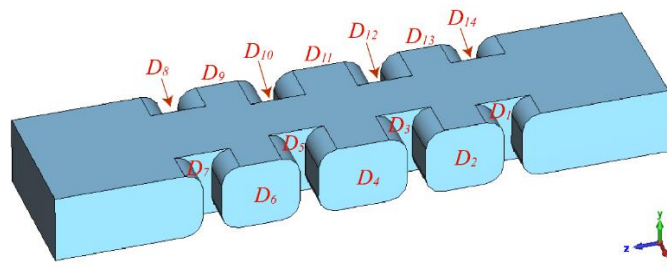


**Figure 3.8** Parameters  $D_1$ - $D_{14}$  which represents the face displacement in X direction of the specified face.

After single simulation, the magnitude of derivative of  $S_{21}$  parameters for parameters  $D_1$ - $D_{14}$ ,  $\left| \frac{\partial S_{21}}{\partial D_1} \right|$  to  $\left| \frac{\partial S_{21}}{\partial D_{14}} \right|$ , are directly presented in CST. Based on the structural symmetry, the study on parameters  $D_1$ - $D_4$  is sufficient for sensitivity analysis of the whole device as shown in Figure 3.9. These four parameters can represent other parameters at symmetrical and center symmetrical location. For example, the performance of  $D_1$  is

the same as that of  $D_7$ ,  $D_8$ , and  $D_{14}$ . The yellow dashed line is  $\left|\frac{\partial S_{21}}{\partial D_1}\right|$ . The green dash-dot line is  $\left|\frac{\partial S_{21}}{\partial D_2}\right|$ . The red solid line is  $\left|\frac{\partial S_{21}}{\partial D_3}\right|$ . The blue dot line is  $\left|\frac{\partial S_{21}}{\partial D_4}\right|$ .

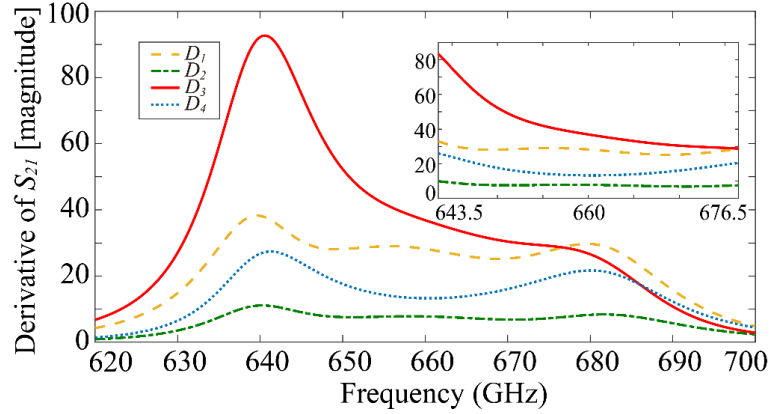


**Figure 3.9** Magnitude of derivative of  $S_{21}$  parameters for parameters  $D_1$ - $D_4$ .

As shown in Figure 3.9 sensitivity of each parameter is different at different frequency. The inset figure is the enlarged view over the passband where

$$\left|\frac{\partial S_{21}}{\partial D_3}\right| > \left|\frac{\partial S_{21}}{\partial D_1}\right| > \left|\frac{\partial S_{21}}{\partial D_4}\right| > \left|\frac{\partial S_{21}}{\partial D_2}\right| \quad (3.6)$$

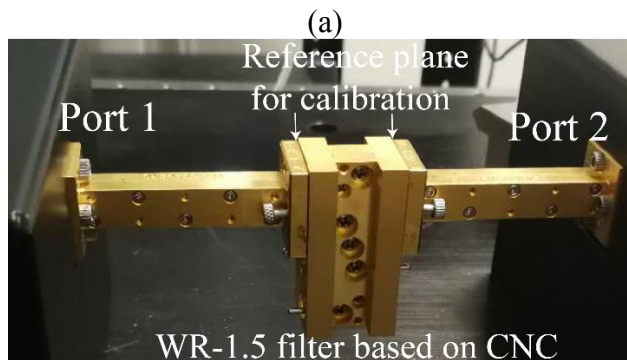
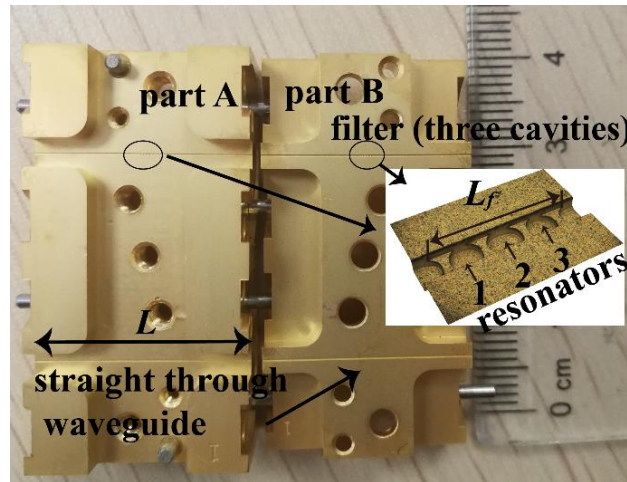
The red solid line  $\left|\frac{\partial S_{21}}{\partial D_3}\right|$  is at the top, which means  $D_3$  is the most sensitive parameter.

As defined in Figure 3.8,  $D_3$  represents the face displacement in X direction of the middle iris  $w_3$ . In other words,  $w_3$  is the most sensitive parameter to the dimension accuracy. The side iris  $D_1$  is the second one. The side resonator  $D_2$  has the lowest sensitivity. Therefore, the sensitivity of irises is larger than cavities. The iris and cavity at middle are more sensitive than the iris and cavity on the sides.

### 3.5 Fabrication and measurement

Computer numerical controlled (CNC) milling is a traditional machining technology which has been used to fabricate metal waveguide components. Millimeter wave waveguide components fabricated by CNC milling perform excellently as demonstrated in a lot of previous work.

After simulation, the filter is fabricated using high-precision MAKINO CNC milling machine and electroplated with 2  $\mu\text{m}$  gold. The nominal tolerance of this CNC machine is 5  $\mu\text{m}$ . A CNC machined block is shown in Figure 3.10 (a). The filter is split into part A and part B along the E-plane of the waveguide to minimize the effect of the cut on the insertion loss. The enlarged figure in Figure 3.10 (a) is the E-plane view of three cavities. It is half of the resonator. The length of the filter ( $L_f$ ) is only 0.96 mm. However, to accommodate the UG387 standard flanges at the input and output, a waveguide section of 9.52 mm ( $L$ ) is added between the filter and the test ports, which leads to additional losses. For correction of the losses from the long waveguide section, a straight waveguide of 20 mm is also fabricated alongside the filter. It is used to estimate and then remove the effect of the waveguide extension from the measurement of the insertion loss of the filter.



(a) Photograph of the fabricated filter along cutplane (E-plane). The view of resonator is shown in the inset ( $L = 20$  mm,  $L_f = 0.96$  mm). (b) Test setup for the filter.

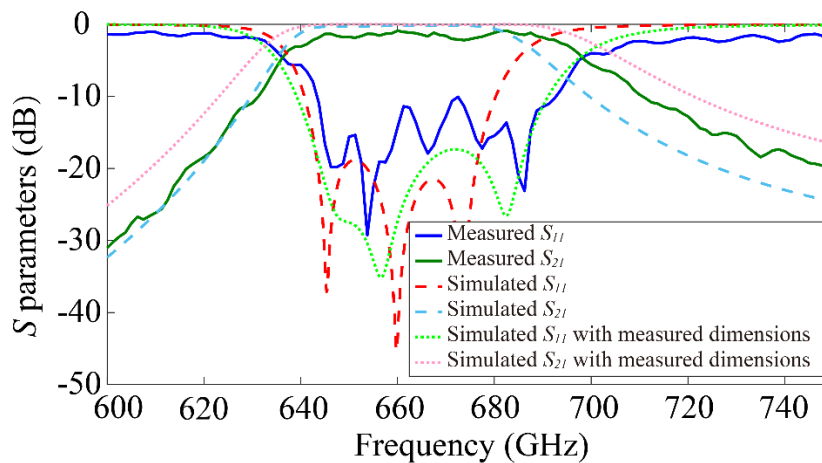


Figure 3.11 Simulated and measured response of the filter.

The  $S$  parameter measurement was carried out using a Keysight VNA network analyzer with a pair of VDI (Virginia Diodes, Inc.) WR-1.5 waveguide heads as shown in Figure 3.10 (b). These heads are up converter heads, which have standard waveguide dimensions and work from 500- 750 GHz. The measured filter exhibits a 7.29 % (48.7 GHz) bandwidth at a center frequency of 667.5 GHz as shown in Figure 3.11. The minimum insertion loss in passband is measured to be 0.87 dB and the return loss is better than 10 dB across the whole passband. The simulated response is shown together with the measured results in Figure 3.11. The measurements are in reasonably good agreement with the simulations. The center frequency of the filter is shifted upwards by around 7.5 GHz and the bandwidth is slightly larger than designed. This frequency discrepancy is mainly due to smaller-than-designed dimensions of the resonators and larger irises between adjacent resonators. The small ripples seen in the  $S_{11}$  response are most probably caused by the non-perfect connection between the filter and waveguide ports.

The dimensions of the manufactured filter were measured using a confocal microscope (ZEISS Smart Proof 5), and the results are shown in Table 3.4. The filter is split to part A and part B, which are measured separately.  $D_{measured}^A$  and  $D_{measured}^B$  in Table 3.4 is the measured dimension for part A and part B, respectively. Note that all the lengths ( $l_1, l_2, l_3$ ) are smaller than designed and all the widths ( $w_1, w_2, w_3, w_4$ ) are larger than designed. From the machine point of view, the milling cutter moves deeper in the vertical direction (X-direction) as shown previously in Figure 3.7. When re-simulated using the measured dimensions, the filter's performance agrees much better with the measurements as shown in Figure 3.11.

**Table 3.4** Comparison between the designed and measured dimensions.

	$D_{designed}$ ( $\mu\text{m}$ )	$D_{measured}^A$ ( $\mu\text{m}$ )	$D_{measured}^B$ ( $\mu\text{m}$ )	$D_{measured}^A - D_{designed}$ ( $\mu\text{m}$ )	$D_{measured}^B - D_{designed}$ ( $\mu\text{m}$ )
$l_1$	213.1	190.0	199.0	-23.1	-14.1
$l_2$	241.4	207.0	226.0	-34.4	-15.4
$l_3$	213.1	184.0	197.0	-29.1	-16.1
$w_1$	205.1	219.3	213.6	14.2	8.5
$w_2$	151.9	169.4	162.9	17.5	11
$w_3$	151.9	168.5	162.8	16.6	10.9
$w_4$	205.1	219.4	216.7	14.3	11.6

### 3.6 Yield analysis

Fabrication tolerances lead to performance deviation from the specification. Therefore, a yield analysis is performed based on the manufacturing tolerance. Yield percentage is defined as the ratio of the qualified number over the total quantity as given below [26] .

$$\text{Yield percentage} = \frac{\text{number of passed}}{\text{total quantity}} \quad (3.7)$$

This percentage can be estimated directly in CST after a sensitivity analysis for model parameters. There is no need to perform additional 3D simulations when the parameters vary in a small range. In CST, assuming the tolerance is 2.5  $\mu\text{m}$ , the qualification criteria is that the return loss is higher than 10 dB over 643.5- 676.5 GHz, the yield percentage of the filter would be 92.4 %. An alternative way to depict this is shown in Figure 3.12 where a set of sweep results with maximum dimensional variation of 2.5  $\mu\text{m}$  are shown as grey curves. Note if the assumed tolerance rises to 10  $\mu\text{m}$  then the yield reduced to 62.7%. The red dashed curve in Figure 3.12 is the simulated  $S_{11}$  parameter with the designed dimensions

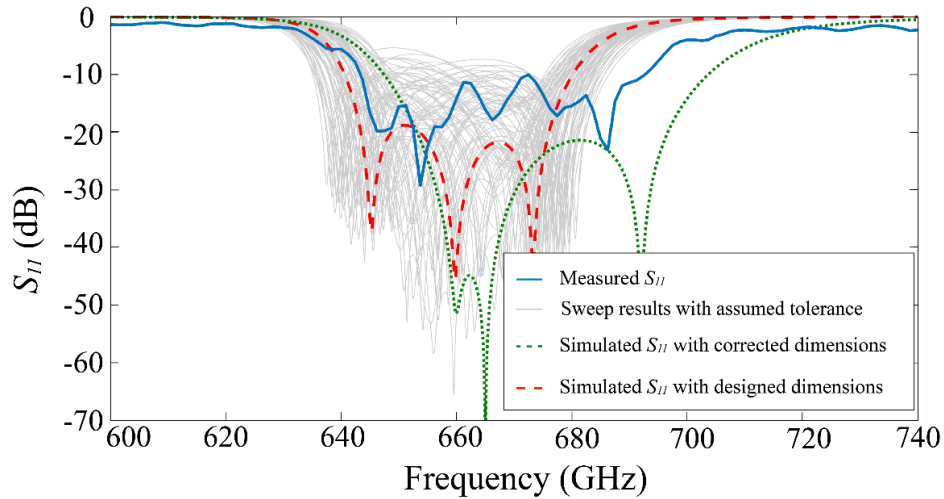


**Figure 3.12** The  $S_{11}$  parameter with the designed dimensions (red dashed curve) and the  $S_{11}$  parameter with corrected dimensions (green solid curve). The grey curves are the sweep results with assumed tolerance of  $2.5 \mu\text{m}$ . The blue curve is the measured  $S_{11}$ .

The real dimensional difference between the as-fabricated device and the design is much larger than the assumed tolerance of  $2.5 \mu\text{m}$  in this case. As shown in Table 3.4, the average difference in length is about  $-22 \mu\text{m}$  and  $13 \mu\text{m}$  in width. Of course, this is for only two devices and not statistically significant. Nevertheless, it is not surprising to see that the yield percentage drops to 24.9 % using the same selection criterion. The low percentage is mainly due to the frequency shift upwards caused by the generally smaller-than-designed resonators.

If we repeat the simulation using the average measured dimensions (i.e., reducing the lengths by  $22 \mu\text{m}$  and increasing the width by  $13 \mu\text{m}$ ), the passband of the filter will be shifted to 653.1 - 696.7 GHz. The  $S_{11}$  parameter with corrected dimensions is shown as green dotted curve in Figure 3.12. If we use this frequency range as the selection criteria, the yield percentage becomes 78.6% under the average measured tolerance.

### **3.7 Summary**

One example of designing a Chebyshev filter is presented in this Chapter. It begins with coupling matrix calculation. Then the method of extracting external quality factor and coupling coefficients in EM simulation is introduced. This is followed by the simulated results and sensitivity analysis. Then the filter is fabricated by high precision CNC machining. Reasonably good agreement between the measurement and simulated results shows that the precision CNC milling is a viable technology for producing terahertz waveguide filters. However, machine tolerance would significantly reduce the yield of production. In the final part of this Chapter, yield analysis is presented. Higher fabrication accuracy and tighter tolerance control is needed for high yield in the fabrication of terahertz waveguide devices.



# Chapter 4 Folded Waveguide Bandpass

## Filter

### 4.1 Introduction

Reasonably good agreement between the measurement and simulated results in Chapter 3 shows that the precision computer numerical control (CNC) milling is a viable technology for producing terahertz waveguide filters. However, the long waveguide section in that filter leads to additional losses. To reduce the loss of waveguide, the filter needs to be shortened by applying folded structure, which can make the whole structure more compact. This is the reason why the filters with folded structure need to be developed.

In this chapter, 4<sup>th</sup> order waveguide bandpass filters with folded structure are designed. Filter-I has been designed with a 0.7 % (0.07 GHz) bandwidth at the center frequency of 10 GHz. Limited to the structure of Filter-I, the bandwidth is narrow. To increase the bandwidth, a new coupling structure with steps is introduced. Based on the new coupling structure, Filter-II is designed with a 2.66 % (0.266 GHz) bandwidth at the center frequency of 10 GHz. This filter is fabricated by CNC milling and exhibits a 3.66% (0.366 GHz) 3 dB-bandwidth at the center frequency of 10.00 GHz. The minimum passband insertion loss is measured to be 0.20 dB and the measured return loss is better than 9.82 dB across the whole passband. To improve the performance, tuning is considered. The tuned filter is centered at 10.00 GHz. The return loss is better

than 16.47 GHz and the minimum insertion loss is 0.19 dB, which are in reasonable agreement with the simulations.

Typical requirements for satellite systems call for filtering functions with sharp cut-off slopes, which can be achieved by introducing transmission zeros at finite frequency [24]. There are many approaches to realize transmission zeros. Geometrically, the cross couplings between non-adjacent resonators can realize transmission zeros [27]. Electrically, exciting multiple modes in certain cavities can also realize transmission zeros [28]. Another method is using extracted pole resonator [29]. Cross coupling may be implemented by folding the direct coupled filter in either the E-plane [30], [31] or H-plane [32] and carving an aperture in the common wall between the corresponding resonators. However, the special folded structure of Filter-II realizes two transmission zeros without aperture in the common wall, which not only simplifies the designing process, but also the technological fabricating process.

Noteworthy, the port-to-port distance of Filter-II is about half wavelength. Compared with presented waveguide folded filters in literature [18], [20], [33], the structure in this work is more compact along the port-to-port axis.

## **4.2 Design of the original X band folded filter-I**

The diagram of the folded filter working at 10 GHz is shown in Figure 4.1. There are four coupled resonators each operating in the  $TE_{101}$  mode and direct coupled together with the topology shown in Figure 4.2. Input and output waveguide ports are facing each other. The whole filter will be split into two halves along the middle cutting-plane

in the process of fabricating. This filter is designed using the coupling matrix approach described in [24]. It is designed to have a Chebyshev response with a center frequency of 10 GHz, a bandwidth of 0.7 %, and a return loss in the passband of 20 dB.

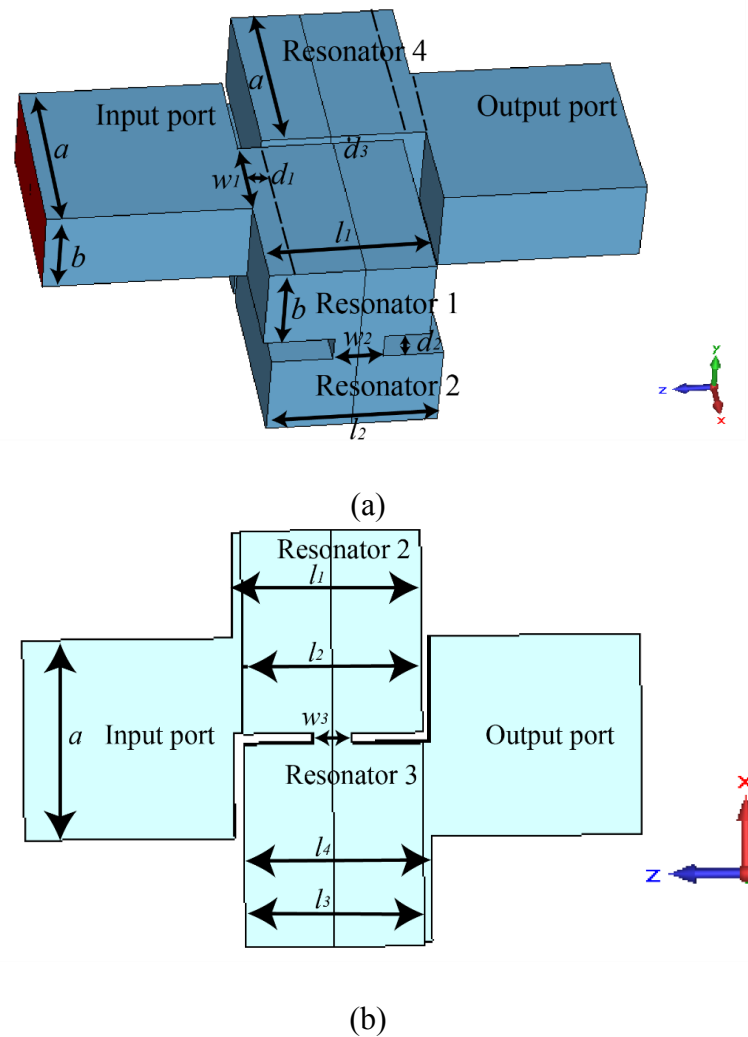


**Figure 4.1** (a) The diagram of the folded filter working at 10 GHz. (b) The bottom view of the filter.  $a= 22.86$  mm,  $b= 10.16$  mm.

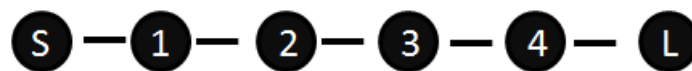


**Figure 4.2** Topology of the folded filter

To meet the specification, the external quality factor and the coupling coefficients are calculated to be  $Q_e = 133.1$ ,  $k_{12} = k_{34} = 0.0064$ , and  $k_{23} = 0.0049$ .

The diagram of the first resonator is shown in Figure 4.3 (a). The relationship between  $Q_e$  and  $w_1$  is shown in Table 4.1 and Figure 4.3 (b). The width of  $w_1$  is limited by the structure ( $0 \leq w_1 < a/2$ ). The value of  $w_2$  is designed as a small value to make sure weak coupling at this port.

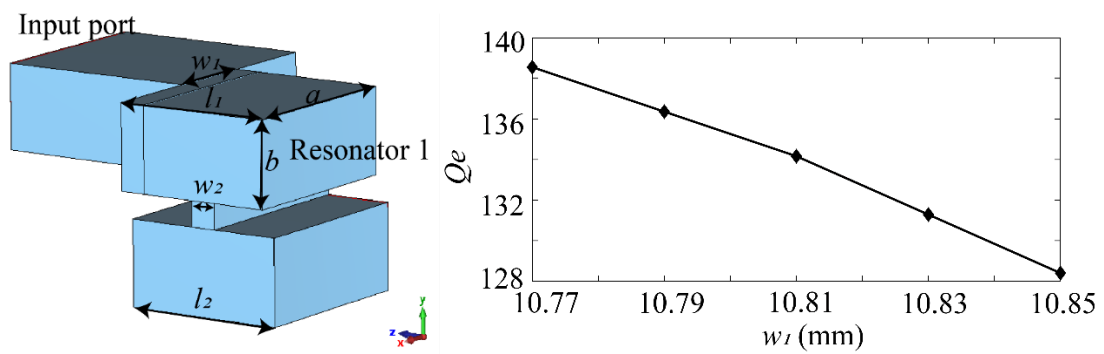


**Figure 4.3** (a) The diagram of resonator 1 used to extract the external quality factor  $Q_e$ .

(b) The relationship between  $Q_e$  and  $w_1$ .

**Table 4.1** The relationship between  $Q_e$  and  $w_1$ .

$w_1$ (mm)	10.85	10.83	10.81	10.79	10.77
$l_1$ (mm)	16.02	16.02	16.03	16.03	16.04
$f_0$ (GHz)	10.00	10.00	10	10.00	10.00
$\Delta f$ (GHz)	0.078	0.076	0.074	0.073	0.072
$Q_e$	128.40	132.29	134.37	136.36	138.55

The structure shown in Figure 4.4 (a) is used to find the relationship between  $k_{12}$  and  $w_2$ . The relationship is shown in Table 4.2 and Figure 4.4 (b). The values of  $w_1$  and  $w_3$  are small to make sure weak coupling at two ports.

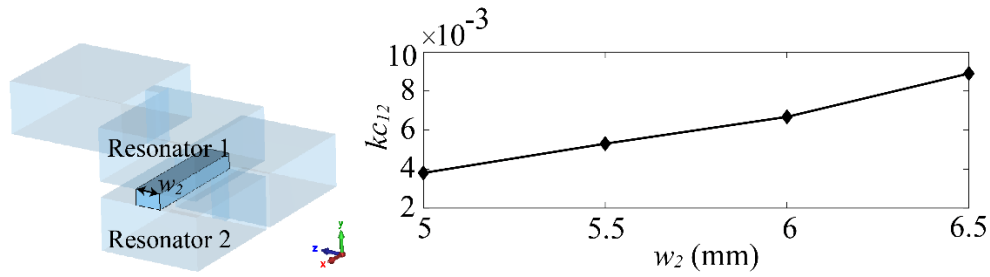


**Figure 4.4** (a) The diagram of resonator 1 and resonator 2. (b) The relationship between  $k_{12}$  and  $w_2$ .

**Table 4.2** The relationship between  $k_{12}$  and  $w_2$ .

$w_2$ (mm)	5	5.5	6	6.5
$l_1$ ( $l_2$ ) (mm)	20.1	20.2	20.25	20.31
$f_1$ (GHz)	9.99	9.97	9.97	9.97
$f_2$ (GHz)	10.03	10.03	10.04	10.06
$f_0$ (GHz)	10.01	10.00	10.01	10.01
$k_{c12}$ (GHz)	0.0038	0.0053	0.0067	0.0089

The structure shown in Figure 4.5 (a) is used to find the relationship between  $k_{23}$  and  $w_3$ . The relationship is shown in Table 4.3 and Figure 4.5 (b).

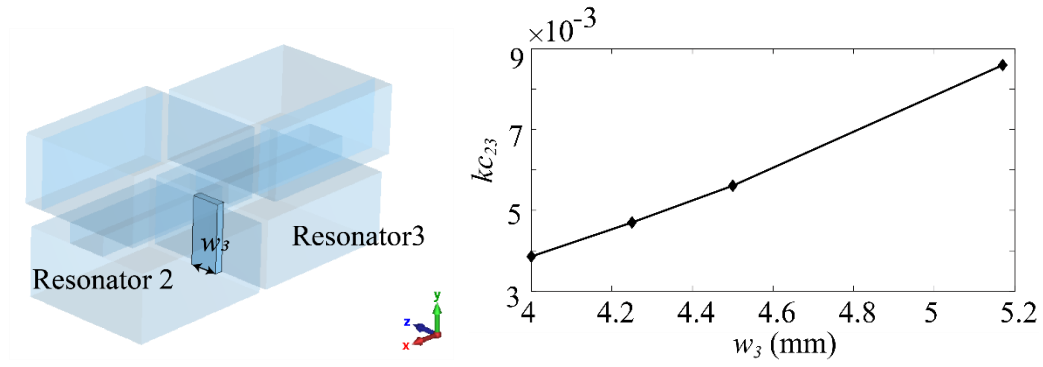


**Figure 4.5** (a) The diagram of resonator 2 and resonator 3. (b) The relationship between  $k_{c23}$  and  $w_3$ .

**Table 4.3** The relationship between  $k_{c23}$  and  $w_3$ .

$w_3$ (mm)	4.0	4.25	4.5	5.17
$l_2$ ( $l_3$ ) (mm)	19.81	19.8	19.79	19.7
$f_1$ (GHz)	9.99	9.98	9.97	9.96
$f_2$ (GHz)	10.03	10.03	10.03	10.05
$f_0$ (GHz)	10.01	10.00	10.00	10.00
$k_{c23}$	0.0039	0.0047	0.0056	0.0086

Based on the calculation above, the initial values for all the parameters in the filter can be obtained as shown in the first row of Table 4.4. After optimization, the values of the parameters in the filter are shown in the second row of Table 4.4. The comparison between initial results and optimized results are shown in Figure 4.6.

**Table 4.4** Initial and final values for parameters in the filter.

	$w_1$ (mm)	$w_2$ (mm)	$w_3$ (mm)	$l_1$ ( $l_4$ ) (mm)	$l_2$ ( $l_3$ ) (mm)
<b>Initial</b>	10.82	5.90	4.30	16.43	20.20
<b>Final</b>	10.84	5.86	4.42	16.45	20.16

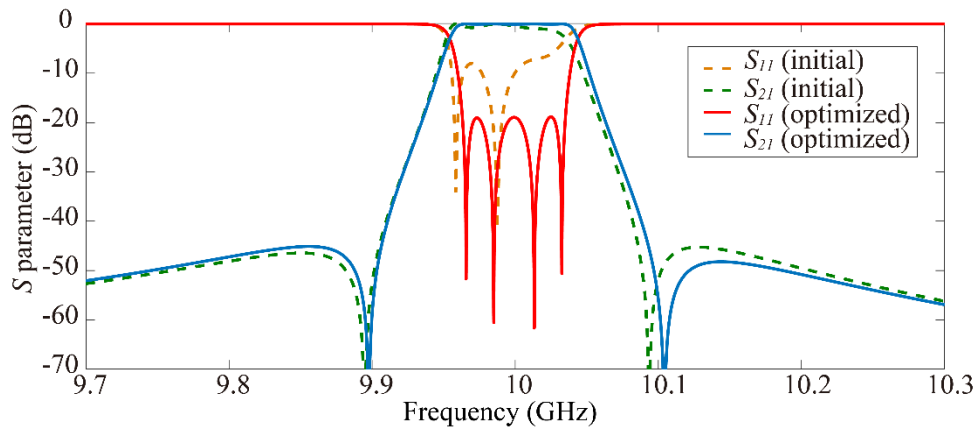


**Figure 4.6** Simulated  $S$  parameters with the initial values and the results after optimization.

After changing the background material to Aluminum, the  $S$  parameters are shown in Figure 4.7. The filter is centered at 10.00 GHz with a 0.72% bandwidth. The insertion loss in passband is about 0.36 dB and the return loss is better than 19.0 dB across the whole passband.

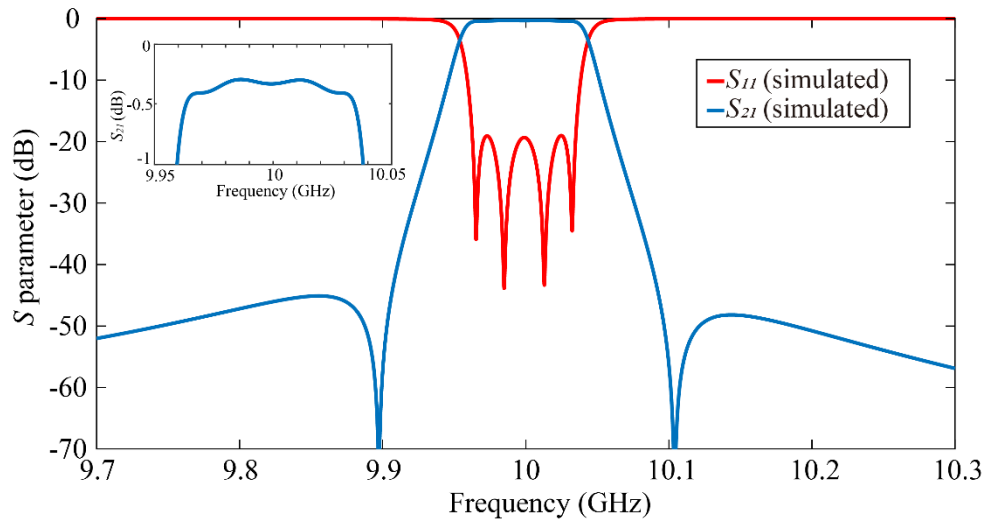


**Figure 4.7** Simulated  $S$  parameters when the background material is Aluminum. The insertion loss of the passband is enlarged.

The current distribution in  $Z$  direction is shown in Figure 4.8. There is some current along the cutting plane, but the current minima are still largely around the plane. Therefore, splitting the device from the middle is not expected to lead to large losses.

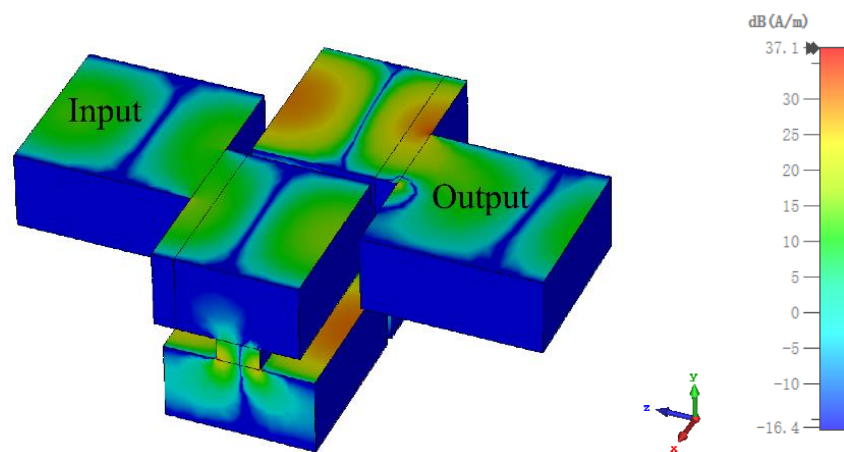


**Figure 4.8** Current distribution at different times.



### 4.3 Connection with steps

In Chapter 4.2, the waveguide port is connected to the first resonator directly as shown in Figure 4.1. The bandwidth is limited by the size of the overlap between the port and the adjacent resonator. If the same coupling structure is applied on the filter working at higher frequency, the small bandwidth leads to strict requirement on fabrication accuracy, which increases the difficulty. To increase the bandwidth, the structure can be modified by adding steps between the port and the adjacent resonator as shown in Figure 4.9. The blue model is the air inside the filter. Three steps are shown clearly. The number of steps and the dimensions of steps are analyzed as followed.

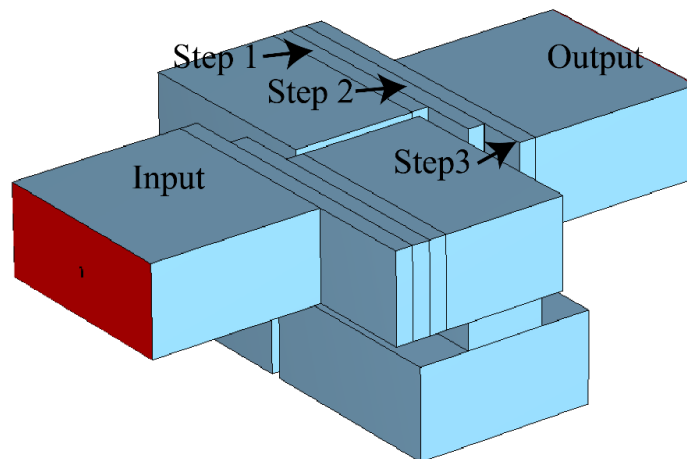


**Figure 4.9** The diagram of the improved folded filter with new coupling structure.

The coupling structures with one step and two steps are shown in Figure 4.10 (a) and (b) respectively. The performances of these two different coupling structures are compared in this part. The connection with two steps is proved that it can realize larger bandwidth than the connection with only one step.

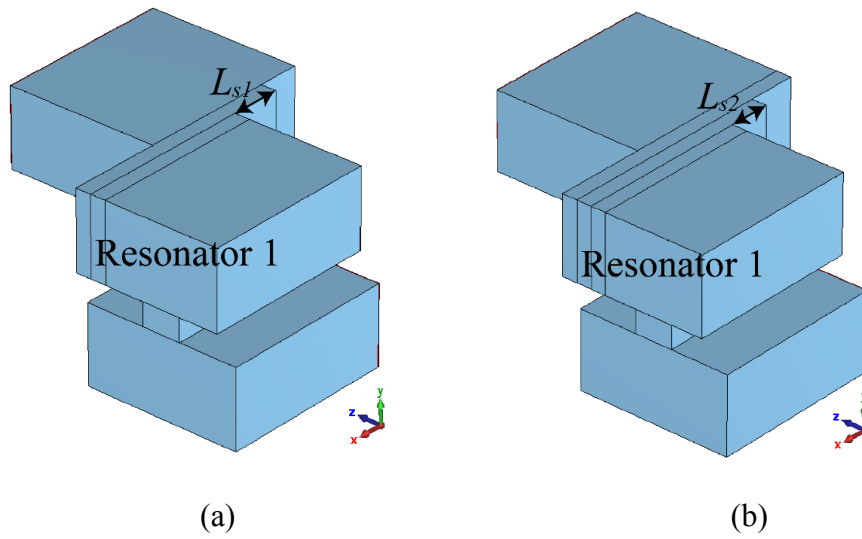


**Figure 4.10** (a) The connections with one step. (b) The connections with two steps.

The length of the step  $L_s$  has an effect on the external quality factor  $Q_e$  and hence affects the bandwidth. For the first structure shown in Figure 4.10 (a), the relationship between  $L_{s1}$  and  $Q_e$  is shown in Table 4.5.

**Table 4.5** The relationship between  $L_{s1}$  and  $Q_e$ .

$L_{s1}$ (mm)	0.04	0.05	0.06	0.07	0.08	0.1	0.12	0.14
$f_0$ (GHz)	660	660	660.03	660	660.02	660.01	660	660
$\Delta f$ (GHz)	6.19	6.35	6.49	6.58	6.66	6.69	6.68	6.62
$\Delta f/f_0$ (%)	0.94	0.96	0.98	1.00	1.01	1.01	1.01	1.00
$Q_e$	106.67	103.93	101.69	100.35	99.13	98.59	98.83	99.63

For the second structure shown in Figure 4.10 (b), the relationship between  $L_{s2}$  and  $Q_e$  is shown in Table 4.6.

**Table 4.6** The relationship between  $L_{s2}$  and  $Q_e$ .

$L_{s2}$ (mm)	0.04	0.06	0.08	0.10	0.12	0.14
$f_0$ (GHz)	660.00	659.98	659.95	660.01	660.00	659.99
$\Delta f$ (GHz)	12.03	12.55	12.86	12.93	12.88	12.81
$\Delta f/f_0$ (%)	1.82	1.90	1.95	1.96	1.95	1.94
$Q_e$	54.86	52.57	51.34	51.05	51.25	51.52

To compare the performance, the data in Table 5 and Table 6 are plotted together shown in Figure 4.11. The blue curve is for the connection with one step. The red curve is for the connection with two steps. The connection with two steps can realize lower external quality factor  $Q_e$ . Therefore, to get a larger bandwidth, two steps can be applied between the port and the adjacent resonator.

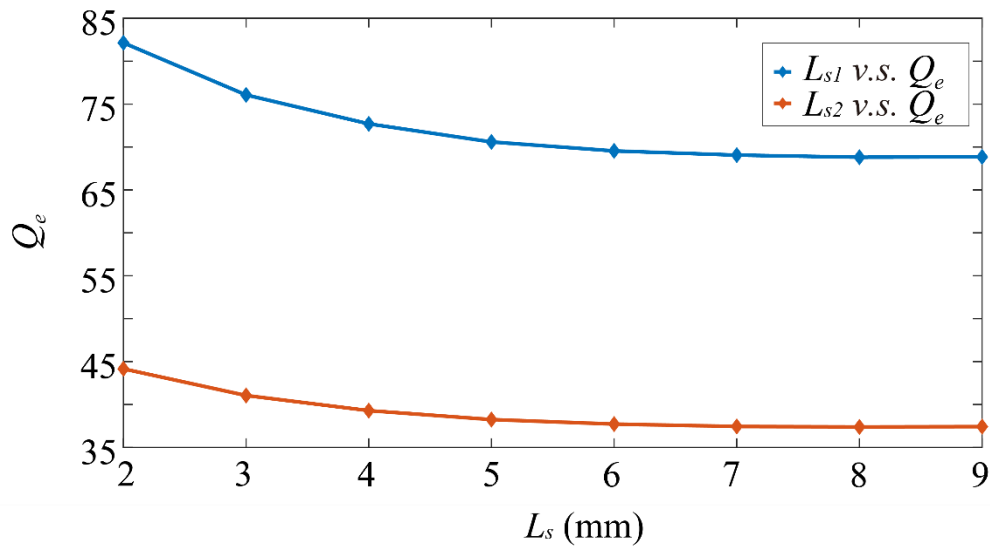


**Figure 4.11.** The comparison between two different connections.

As shown in Figure 4.11, the value of  $Q_e$  decreases at first then level off. More energy

is transferred to the resonator from the port as the length of step ( $L_s$ ) increases. However, the step cannot increase the bandwidth when the edge of step is near to the edge of port. Normally, the minimum  $Q_e$  is used to realize maximum bandwidth. However it's hard to find the exact minimum  $Q_e$  by several times of simulations. Therefore, an approximated minimum  $Q_e$  is used in the following design.

## 4.4 Improved X band folded filter-II

### 4.4.1 Design of the filter

The coupling structure with two steps was proved that it can realize larger bandwidth than direct coupling. This coupling structure is applied to a filter working at X-band. The filter-II works at 10 GHz with 2.66% bandwidth. The external quality factor and the coupling coefficients are shown in Table 4.7.

**Table 4.7** Filter specification for the filter working at 10 GHz.

$Q_e$	35.015
$kc_{12}, kc_{34}$	0.024
$kc_{23}$	0.019

**Table 4.8** the relationship between  $L_s$  and  $Q_e$

$L_s$ (mm)	2	4	5	6	8	9.5
$f_0$ (GHz)	10.00	10.00	10.00	10.00	10.00	10.00
$\Delta f$ (GHz)	0.25	0.28	0.29	0.29	0.30	0.30
$Q_e$	40.06	35.61	34.60	34.11	33.76	33.76

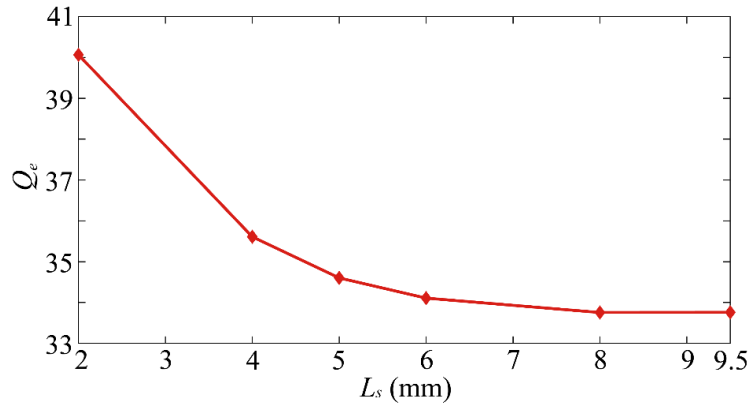


**Figure 4.12** The relationship between  $L_s$  and  $Q_e$ .

**Table 4.9** The relationship between  $w_1$  and  $kc_{12}$  ( $kc_{34}$ ).

$w_1$ (mm)	6	7	8	9	10
$f_1$ (GHz)	9.97	9.94	9.91	9.88	9.84
$f_2$ (GHz)	10.05	10.07	10.09	10.12	10.17
$f_0$ (GHz)	10.01	10.01	10.00	10.00	10.00
$kc_{12}$ ( $kc_{34}$ )	0.0082	0.012	0.018	0.024	0.032

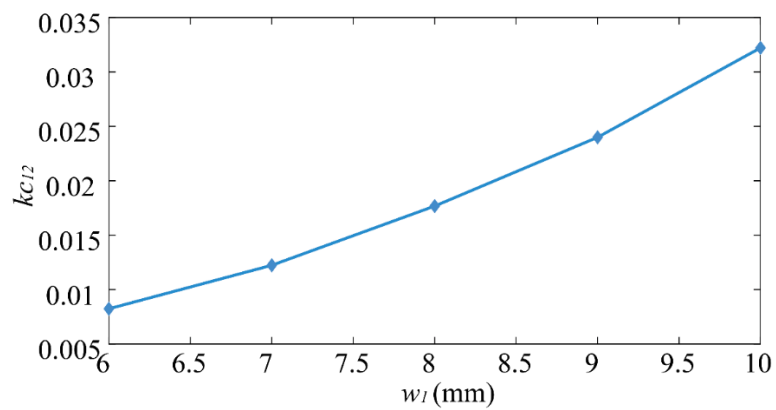


**Figure 4.13** The relationship between  $w_1$  and  $kc_{12}$  ( $kc_{34}$ ).

**Table 4.10** the relationship between  $w_2$  and  $kc_{23}$

$w_2$ (mm)	4	5	6	7	8
$f_1$ (GHz)	9.98	9.97	9.95	9.92	9.88
$f_2$ (GHz)	10.01	10.04	10.06	10.09	10.12
$f_0$ (GHz)	9.9982	10.00	10.00	10.00	10.00
$kc_{23}$	0.0032	0.0064	0.011	0.017	0.025

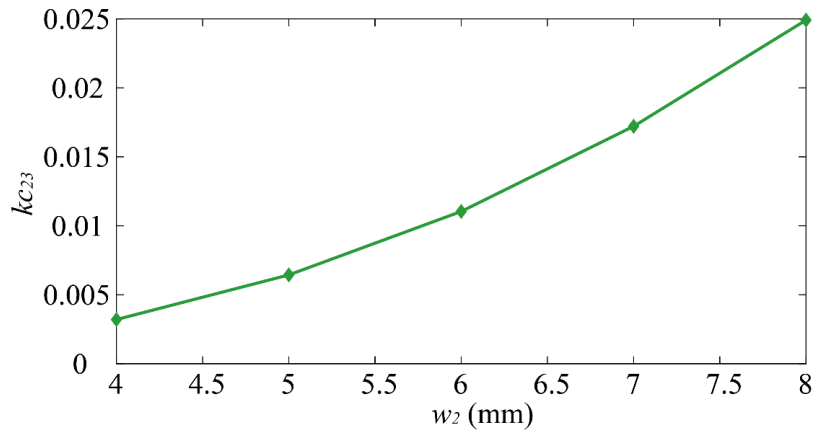


**Figure 4.14** The relationship between  $w_2$  and  $kc_{23}$ .

Based on Table 4.8- 4.10 and Figure 4.12- 4.14, the initial dimensions of all the main parameters can be estimated. The initial values for  $L_s$ ,  $w_1$  and  $w_2$  can be obtained as shown in the first row of Table 4.11. The dimensions are optimized in CST. The optimization goal of  $S_{21}$  is set below -20 dB. The second row shows the final values after optimization.

**Table 4.11** The initial values for all the parameters.

parameters	$L_s$	$w_1$	$w_2$	$l_1 (l_4)$	$l_2 (l_3)$
<b>Initial (mm)</b>	4.59	9.02	7.18	13.80	20.55
<b>Final (mm)</b>	5.04	8.83	7.50	13.71	20.45

The initial responses are shown as dashed lines in Figure 4.15. The responses after optimization are plotted as solid lines in Figure 4.15. The filter shows a 2.67% (0.267 GHz) bandwidth at the centre frequency of 10.00 GHz. The return loss is better than 19.26 dB across the whole passband.

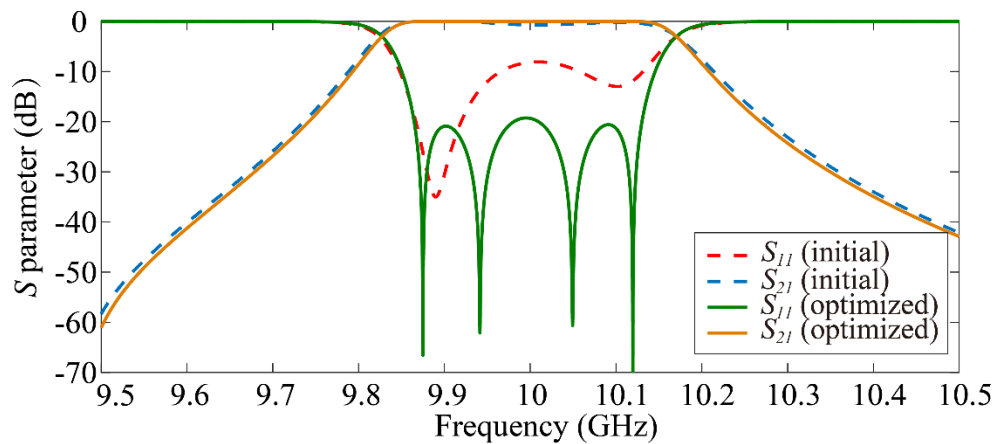


**Figure 4.15** The  $S$  parameters for the filter with initial values. And the  $S$  parameters after optimization.

If the cutting plane of the filter interrupt the surface current, the loss of the filter will be large. Therefore, the current minima in propagation direction ( $Z$  direction) should be designed as the cutting lines. The current distributions along  $Z$  direction are shown in Figure 4.16. Resonator 1 (3) and resonator 2 (4) are aligned. The cutting plane can be

designed as staggered as shown in Figure 4.16. The filter will be split into two halves along the red cutting line.

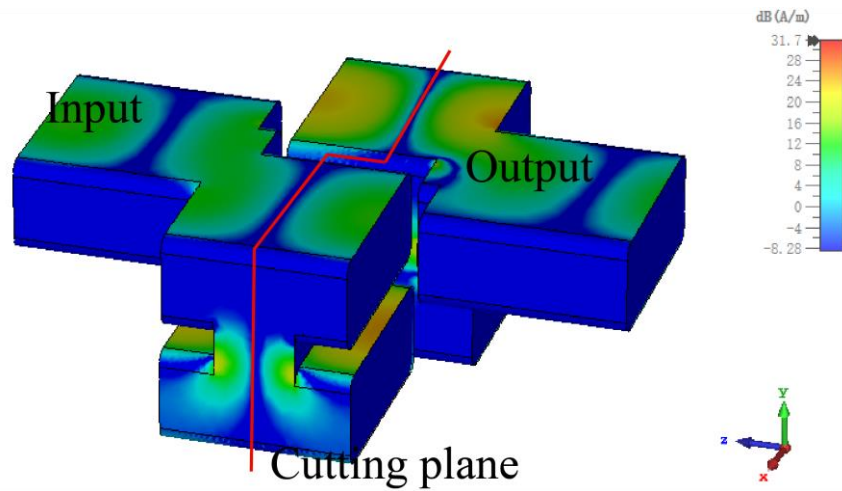


**Figure 4.16** The current distribution in along z direction.

Aluminum with a conductivity of  $3.56 \times 10^7$  S/m is used in the simulation. The results are shown in Figure 4.17. The filter shows a 2.67 % (0.267 GHz) bandwidth at the centre frequency of 10.00 GHz. The return loss is better than 19.46 dB across the whole passband. The minimum passband insertion loss is about 0.15 dB.

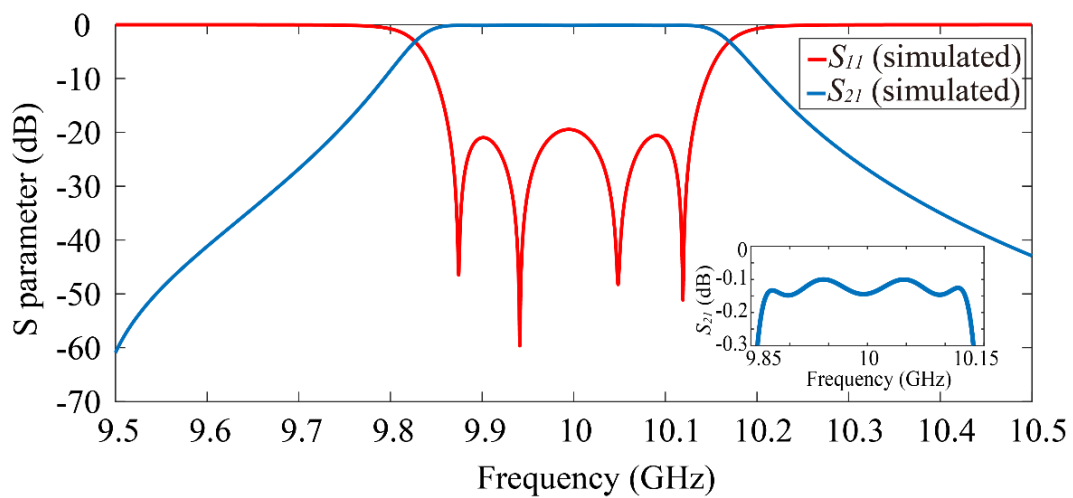


**Figure 4.17** The  $S$  parameters when the background material is aluminum.



#### 4.4.2 Fabrication and Measurement

The filter is fabricated by CNC. Figure 4.18 shows the manufactured filter. The filter is split into two halves along the staggered cutting line. The enlarged view of the waveguide port is shown in Figure 4.18 (b). The step between the port and adjacent resonator can be seen clearly. Half of the manufactured filter is shown in Figure 4.19.

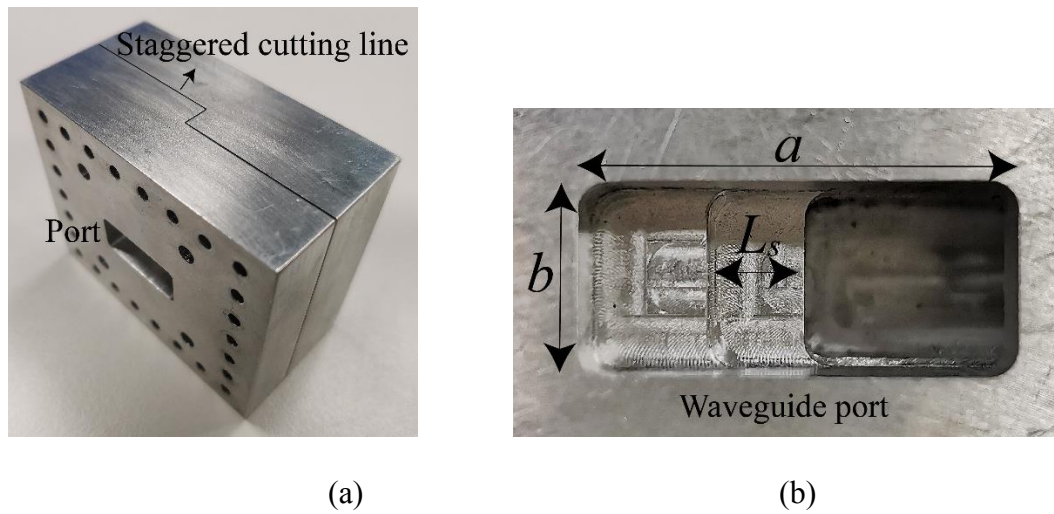


**Figure 4.18** (a) Photograph of the fabricated folded BPF. (b) The enlarged view of the waveguide port.

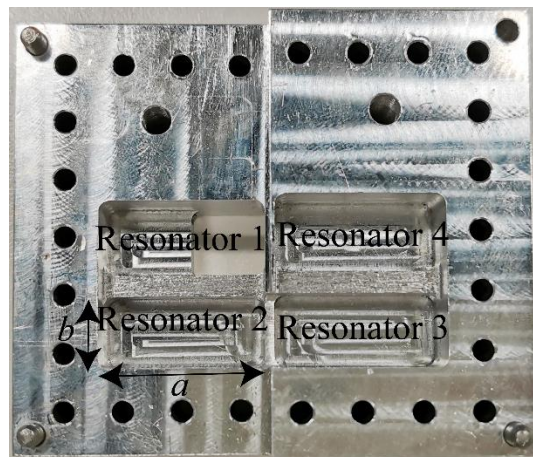


**Figure 4.19** Half of the manufactured filter. Another piece is central symmetric to this one.

The  $S$  parameter measurements of the folded filter were carried out using a Keysight VNA network analyzer. The filter has been measured with a 3.66% (0.366 GHz) 3 dB-bandwidth at the center frequency of 10.00 GHz. The minimum passband insertion loss ( $IL$ ) is measured to be 0.20 dB and the measured return loss ( $RL$ ) is better than 9.82 dB across the whole passband. The comparison between the measured responses and the simulated responses is shown in Figure 4.20.

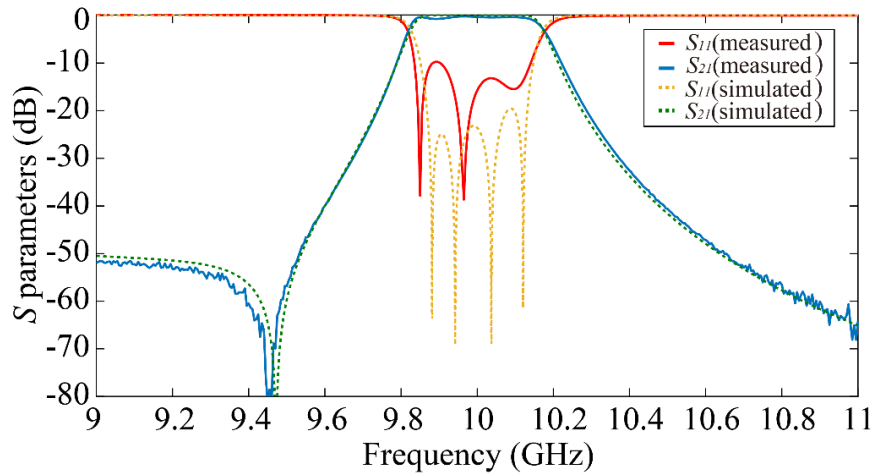


**Figure 4.20** The comparison between the measured responses and the simulated responses.

The normalized coupling matrix corresponding to the measured responses is extracted using CST. The extracted normalized  $n+2$  coupling matrix is

$$M_{extracted} = \begin{bmatrix} 0 & 1.01 & 0 & 0 & 0 & 0 \\ 1.01 & -0.29 & 0.95 & 0 & 0 & 0 \\ 0 & 0.95 & 0.04 & 0.73 & 0 & 0 \\ 0 & 0 & 0.73 & 0.04 & 0.95 & 0 \\ 0 & 0 & 0 & 0.95 & -0.29 & 1.01 \\ 0 & 0 & 0 & 0 & 1.01 & 0 \end{bmatrix},$$

$n$  represents the order of the filter, which is 4 in this case.

Based on the coupling matrix, the parameters in the designed model are adjusted to fit the measured  $S$  parameters. The comparison between the fitting curves and the

measured responses is shown in Figure 4.21. The fitting curves have a good agreement with the measured responses, which means the fitting dimensions are reliable in simulation. The original designed dimensions, the fitting dimensions and the physical measured dimensions are shown in Table 4.12. The dimensions are measured three times using depth micrometer and the values in Table 4.12 are the average values. The precision of the depth micrometer is 0.01mm. The fitting dimensions and the measured dimensions are not same, the maximum difference is 9  $\mu\text{m}$ .

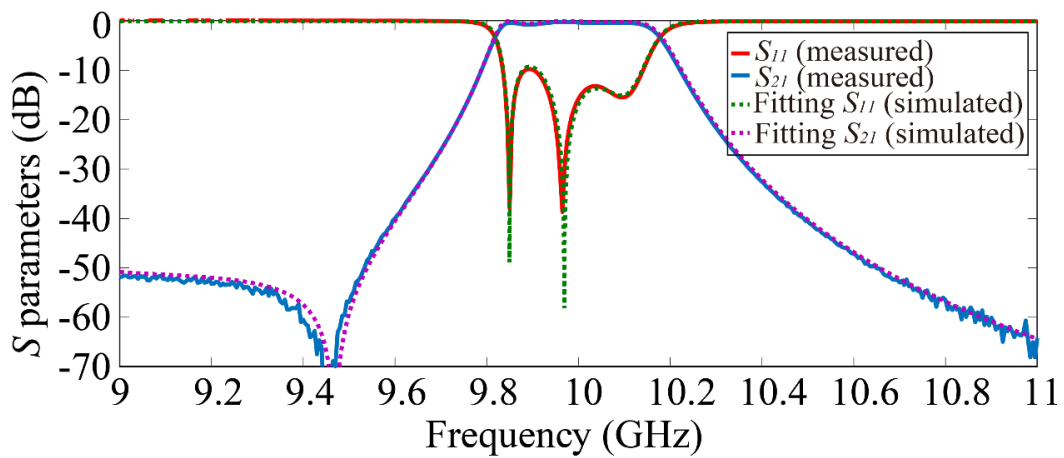


**Figure 4.21** The comparison between the fitting curves and the measured responses.

**Table 4.12** The designed dimensions, the fitting dimensions and the measured dimensions.

	$w_1$ ( $w_3$ ) (mm)	$w_2$ (mm)	$l_1$ ( $l_4$ ) (mm)	$l_2$ ( $l_3$ ) (mm)	$L_s$ (mm)
<b>Design dimensions</b>	8.83	7.50	13.71	20.45	5.04
<b>Fitting dimensions</b>	8.93	7.58	13.62	20.48	5.00
<b>Measured dimensions</b>	8.85	7.53	13.73	20.46	5.09

### 4.4.3 Tuning and measurement

To fulfill the specification, tuning is considered. Based on the model with fitting dimensions shown in Table 4.12, tuning screws are added at different locations.

The tuning screws are added at the middle of the 1<sup>st</sup> and the 4<sup>th</sup> resonators as shown in Figure 4.22. It is impossible to directly drill two thin cylindrical holes on the top surface. Because there is a long distance between the filter structure to the top surface as shown in Figure 4.19. Therefore, the tuning holes should be drilled on the cutting plane of the filter when the two halves of the filter have not been assembled. The cross section is square.

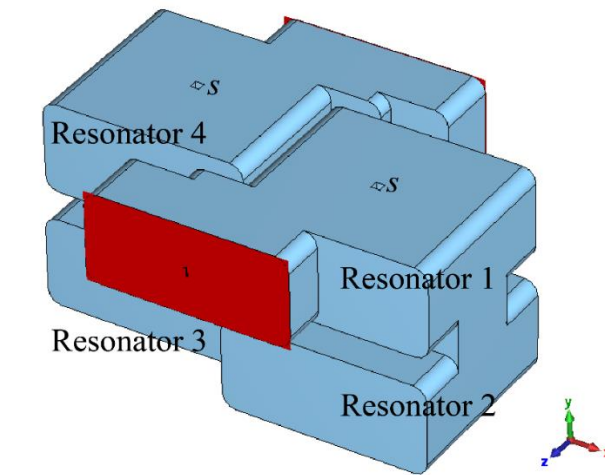


**Figure 4.22** Filter model with tuning screws at the middle of the 1<sup>st</sup> and the 4<sup>th</sup> resonators.

The normalized  $n+2$  coupling matrix of this filter is

$$M_{screw1} = \begin{bmatrix} 0 & 1.05 & 0 & 0 & 0 & 0 \\ 1.05 & 0.05 & 0.99 & 0 & 0 & 0 \\ 0 & 0.99 & 0.06 & 0.74 & 0 & 0 \\ 0 & 0 & 0.74 & 0.06 & 0.99 & 0 \\ 0 & 0 & 0 & 0.99 & 0.05 & 1.05 \\ 0 & 0 & 0 & 0 & 1.05 & 0 \end{bmatrix}$$

Compared  $M_{screw1}$  with  $M_{extracted}$  shown in Chapter 4.4.2, the main difference is that the value of  $M_{11}$  ( $M_{55}$ ) changes from -0.29 to 0.05. In other words, the tuning screws at the middle of the 1<sup>st</sup> and the 4<sup>th</sup> resonator have a big effect on the value of  $M_{11}$  ( $M_{55}$ ).

The tuning screws are added at the iris between the 1<sup>st</sup> and the 2<sup>nd</sup> resonators as shown in Figure 4.23.

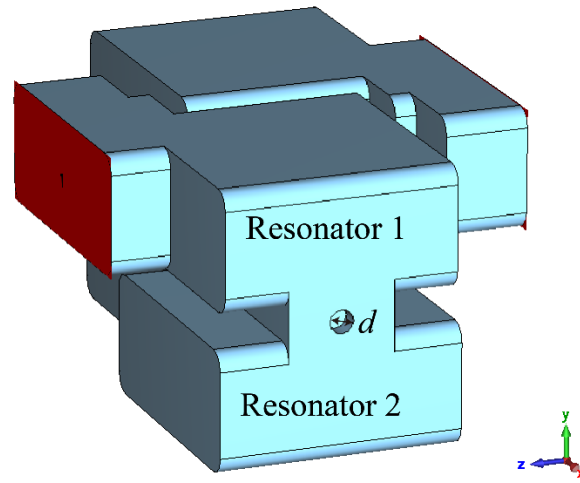


**Figure 4.23** Filter model with tuning screws between the 1<sup>st</sup> and the 2<sup>nd</sup> resonators.

The normalized  $n+2$  coupling matrix of this filter is

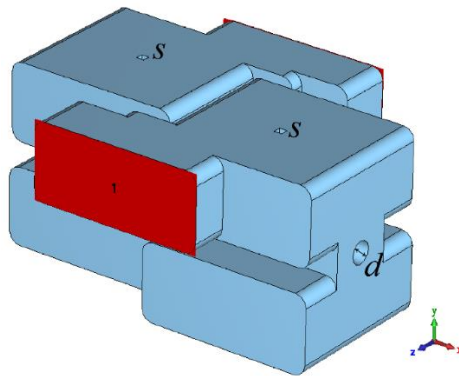
$$M_{screw2} = \begin{bmatrix} 0 & 1.01 & 0 & 0 & 0 & 0 \\ 1.01 & -0.31 & 0.94 & 0 & 0 & 0 \\ 0 & 0.94 & 0.02 & 0.73 & 0 & 0 \\ 0 & 0 & 0.73 & 0.02 & 0.94 & 0 \\ 0 & 0 & 0 & 0.94 & -0.31 & 1.01 \\ 0 & 0 & 0 & 0 & 1.01 & 0 \end{bmatrix}$$

$n$  is the order of the filter, which is 4 in this matrix.

Compared  $M_{screw2}$  with  $M_{extracted}$  shown in Chapter 4.4.2, the value of  $M_{12}$  ( $M_{21}$ ) changes

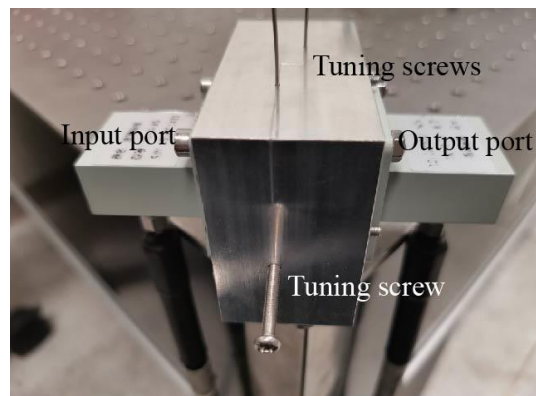
from 0.95 to 0.94. That is to say, the tuning screws between the 1<sup>st</sup> and the 2<sup>nd</sup> resonators influence the value of  $M_{12}$  ( $M_{21}$ ).

Figure 4.24 shows the filter with screws at the location introduced in Figure 4.22 and Figure 4.23. Taking the fabrication into consideration, the cross sections of the screws at the middle of the 1<sup>st</sup> and the 4<sup>th</sup> resonator are designed as squares (1mm \* 1mm).



**Figure 4.24** Filter model with tuning screws. (The optimized size of the screws are 1mm\*1mm\*1.2mm and  $\phi$  3mm\* 4mm)

Figure 4.25 is the measurement of the fabricated filter with tuning screws. The comparison of simulated responses and the measured responses are shown in Figure 4.26.



**Figure 4.25** The fabricated filter with tuning screws.

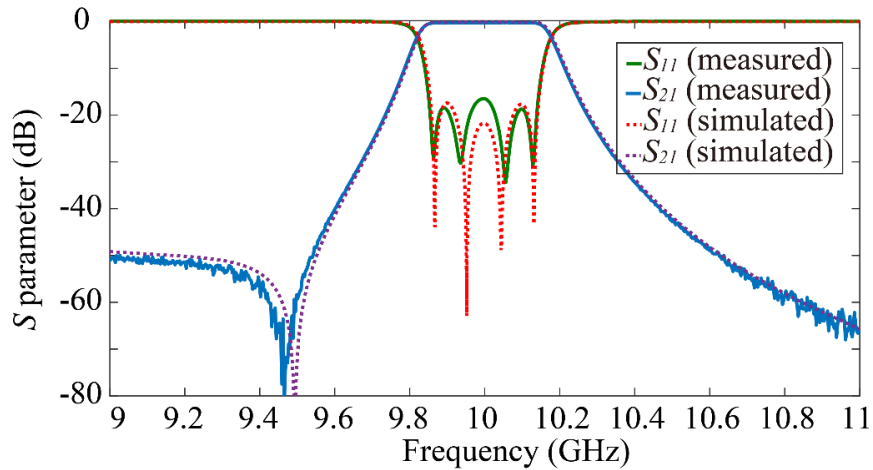


**Figure 4.26** The comparison of the simulated responses and the measured responses.

The measured filter is centered at 10.00 GHz. The return loss is better than 16.47 GHz and the minimum insertion loss is 0.19 dB. The measured responses are in good agreement with the simulations.

#### 4.5 Design of the WR-1.5 band folded filter

Steps coupling structure was introduced and proved that it can increase the bandwidth in previous parts. However, more steps lead to another problem, which is presented in this part. A filter is designed at a centre frequency of 660 GHz with 1.36 % bandwidth as shown in Table 4.13.

The diagram of the folded filter with three-steps and the top view are shown in Figure 4.27. The thickness of the middle iris  $t$  is increased to 0.1 mm. The thickness of each step in the coupling structure  $d_2$  is 0.03 mm.  $d_3$  is 0.05 mm.

**Table 4.13** Filter specification for the 4<sup>th</sup> order folded filter

Order	4
Bandwidth /GHz	10
$f_0$ /GHz	660
$S_{11}$ (dB)	-20
$Q_e$	61.47
$kc_{12}, kc_{34}$	0.0138
$kc_{23}$	0.0106

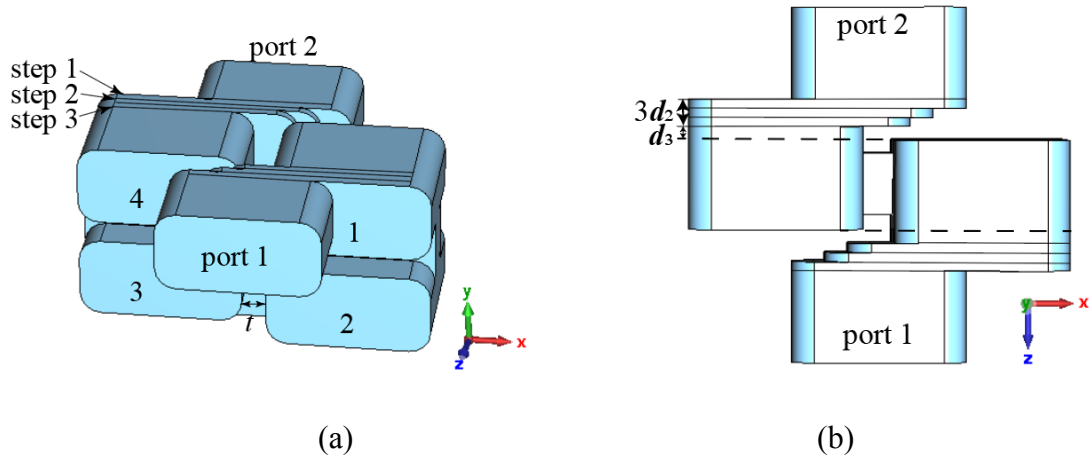


**Figure 4.27** The diagram of the improved filter with three-steps

In the process of design, this structure is proved that it cannot realize the value of  $kc_{23}$ . In other word, the coupling between the 2<sup>nd</sup> resonator and the 3<sup>rd</sup> resonator is too weak. The diagram of the 2<sup>nd</sup>, 3<sup>rd</sup> resonators and the top view are shown in Figure 4.28.



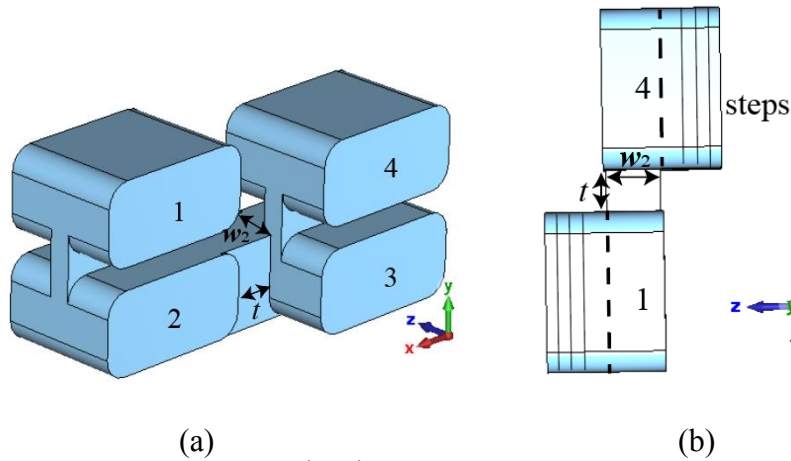


**Figure 4.28** The diagram of the 2<sup>nd</sup>, 3<sup>rd</sup> resonators and the top view.

The relationship between the width of the middle iris  $w_2$  and the coupling coefficient  $kc_{23}$  can be obtained using the structure shown in Figure 4.28. The largest  $w_2$  is about 0.13 mm. The coupling coefficient  $kc_{23}$  is only 0.0026 when  $w_2$  is set as the largest value. The  $S_{21}$  parameter is shown in Figure 4.29.

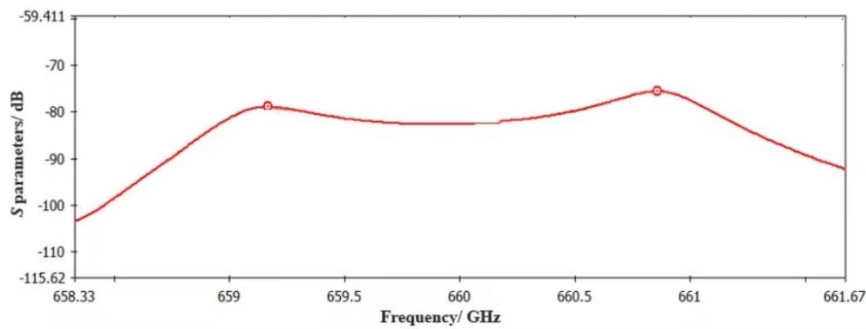


**Figure 4.29**  $S_{21}$  parameter corresponding to particular  $kc_{23}$  (0.0026)

There are two reasons which lead to the weak coupling between the 2<sup>nd</sup> resonator and the 3<sup>rd</sup> resonator. The first reason is the thickness of the middle iris  $t$  is too large (0.1 mm). The second reason is more steps in the coupling structure make the centers of the 1<sup>st</sup> and the 4<sup>th</sup> resonator not aligned as shown in Figure 4.28. The centers of the 2<sup>nd</sup> and

3<sup>rd</sup> are not aligned either. The overlap between the 2<sup>nd</sup> resonator and the 3<sup>rd</sup> resonator limits the coupling coefficient  $kc_{23}$ .

To prove the first reason, the thickness of the middle iris  $t$  is reduced to 0.08 mm. The  $S_{21}$  parameters are shown in Figure 4.30. The red curve is for the thickness  $t$  is 0.1 mm. The green curve is for the thickness  $t$  is 0.08 mm. Larger coupling coefficient  $kc_{23}$  can be obtained using 0.08 mm, compared with 0.1 mm. It means smaller thickness  $t$  can obtain larger  $kc_{23}$ .

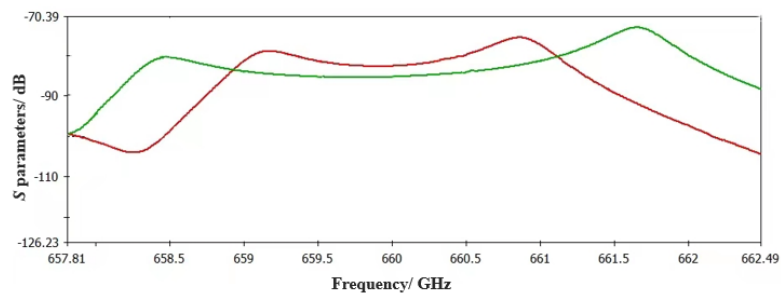


**Figure 4.30**  $S_{21}$  parameters to calculate  $kc_{23}$  when  $t$  is 0.1 mm (red) and 0.08 mm (green).

To prove the second possible reason, the thickness of each step  $d_2$  is reduced to 0.02 mm. The  $S_{21}$  parameters are shown in Figure 4.31. It shows thinner steps can obtain larger  $kc_{23}$ .

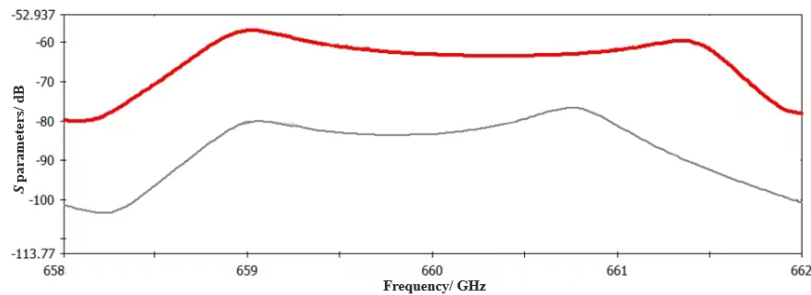


**Figure 4.31**  $S_{21}$  parameters to calculate  $kc_{23}$  when  $d_2$  is 0.02 mm (red) and 0.03 mm (gray)

Based on the analysis above, two methods can be applied to increase the coupling between the second and the third resonator. The first method is to reduce the thickness of the middle iris  $t$ . The second method is to reduce the thickness of each step  $d_2$ .

The original value of  $d_2$  is 0.03mm and  $d_3$  is 0.05mm as mentioned at the beginning of this section. For the improved filter, the thickness of each step  $d_2$  is reduced to 0.02 mm,  $d_3$  is 0.03 mm and the thickness of the middle iris  $t$  is set as 0.07 mm. The relationship between the value of  $Q_e$  and the length of step  $l_s$  is shown in Table 4.14 and Figure 4.32.

**Table 4.14** the relationship between  $Q_e$  and  $l_s$

$l_s/\text{mm}$	0.02	0.04	0.06	0.08
$l_1/\text{mm}$	0.1878	0.1880	0.1881	0.1882
$f_0/\text{GHz}$	660.08	659.98	659.99	660
$BW/\text{GHz}$	9.0814	9.4481	9.6698	9.7538
$Q_e$	72.6848	69.8532	68.2527	67.6659

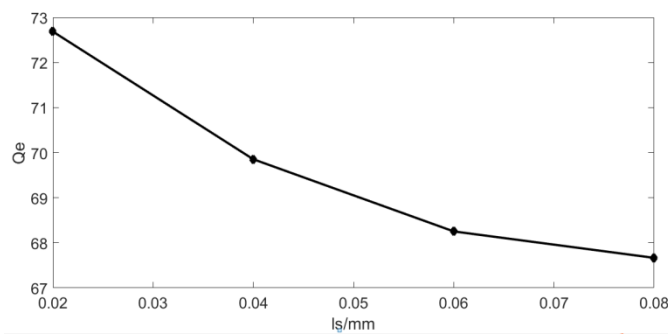


**Figure 4.32** the relationship between  $Q_e$  and  $l_s$

Therefore, the 20 dB return loss bandwidth is assumed as 9 GHz in filter specification as shown in Table 4.15. The external quality factor and coupling coefficients are also

shown. The final values for all the parameters in the filter are shown in Table 4.16. The optimized  $S$  parameters are shown in Figure 4.33. The filter is measured at a centre frequency of 659.91 GHz with 1.416% bandwidth (9.34 GHz).

**Table 4.15** Filter specification for the improved filter

Order	4
Bandwidth /GHz	9
$f_0$ /GHz	660
$S_{11}$ /dB	-20
$Q_e$	68.3024
$kc_{12}, kc_{34}$	0.0124
$kc_{23}$	0.0096

**Table 4.16** The final values for all the parameters

Parameters	$d_2$	$d_3$	$t$	$l_s$	$l_{s2}$	$w_1$	$w_2$	$l_1, l_4$	$l_2, l_3$
Final values/mm	0.02	0.03	0.07	0.068	0.118	0.1112	0.1375	0.1945	0.2875

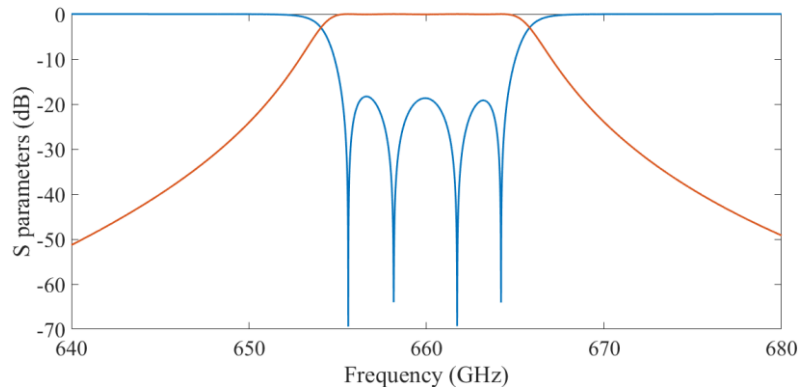


**Figure 4.33** The optimized  $S$  parameters for the improved filter.

A 4<sup>th</sup> order folded waveguide filter working at 660 GHz is designed in this part. The filter shows good performance. However, after considering the tolerance of the commercial CNC machining, this filter has not been fabricated.

## **4.6 Summary**

In this Chapter, three 4<sup>th</sup> order waveguide bandpass filters with a compact folded structure are presented. Filter in Design-I has been designed with a 0.7% bandwidth at the center frequency of 10 GHz. To increase the bandwidth, a new coupling structure with steps is introduced to the filter in Design-II. A 2.66% bandwidth can be achieved. The minimum passband insertion loss is measured to be 0.2 dB and the return loss is better than 9.8 dB across the whole passband. To improve the performance, tuning is implemented. The tuned filter in Design-II is centered at 10.0 GHz. The return loss is better than 16.5 dB and the minimum insertion loss is 0.19 dB, which are in good agreement with the simulations. In Design-III, the folded filter is designed at 660 GHz with a 9 GHz bandwidth.

# Chapter 5 3D printed bent and twisted filters at U/V-band

## 5.1 Introduction

In recent years, three-dimensional (3D) printing has attracted strong research interests. 3-D printing presents attractive benefits on flexibility in structural and material selection. In contrast to filters fabricated by conventional milling technologies, some 3D printed filters can be manufactured in a single piece (monolithic build) without assembly [34]. A number of different 3D printing technologies have been introduced in Chapter 1. Future earth observation missions, aimed at atmospheric studies, require groundbased radiometers with high performance. Broadband channels between 51-57 GHz are used in temperature sounding for tropospheric profile. The frequency range for U band is from 40 GHz to 60 GHz. The frequency range for V band is from 50 GHz to 75 GHz. Both bands can cover the passband range (51-57 GHz). Therefore, U/V band filters are designed and fabricated.

This chapter will first analyze the bent and twisted resonators so a filter can be designed. Resonators bent in the H-plane, E-plane and twist resonators are analyzed in Section 5.2.1 to Section 5.2.3. A bent filter working at U band is designed in Section 5.3. Twisted filters with different bent angles are compared in Section 5.3.1. Filters with different twist angles are compared in Section 5.3.2. Section 5.3.3 describes methods to suppress spurious modes. A prototype twist filter working at V band is demonstrated in Section 5.4. The original filter and the gold coated filter are compared. The effect of

internal surface roughness is analyzed.

Similar 3D printed twisted waveguide filters were reported in literature but at lower frequency bands: K-band (15-22 GHz) [34] and Ka-band [35]. The proposed 3D printed filter outperforms other V-band filters manufactured by other technologies such as groove gap waveguides in [36] and substrate integrated waveguide (SIW) filter in [37]. Such filters exhibited high insertion losses with minimum of 1.1 dB and 5.7 dB, respectively. Planar V-band microstrip filters were also reported with substrates: GaAs [38], low temperature co-fired ceramic (LTCC) and alumina substrates [39] and liquid crystal polymer (LCP) substrates [40]. Such filters have high insertion losses at V-band but suitable for compact system-on-package design.

## **5.2 Resonators**

The shape of resonator has an effect on the natural quality factor  $Q_0$ . To compare the performance of different resonators, several factors should be considered, including the center frequency, the distance between the fundamental mode and the first high order mode, the distribution of electrical field and the natural quality factor  $Q_0$ . Resonators bent in the H-plane, E-plane and twist resonators are analyzed in this section.

### **5.2.1 Resonators bent in the H-plane**

Four H-plane bend resonators are compared with the same center length but different bend angles of  $0^\circ$ ,  $30^\circ$ ,  $60^\circ$ , and  $90^\circ$ .

The distributions of electrical fields for different resonators are shown in Figure 5.1. The fundamental mode in each resonator is  $TE_{101}$  and the first high order mode is  $TE_{102}$ . The comparison of frequency is shown in Table 5.1.

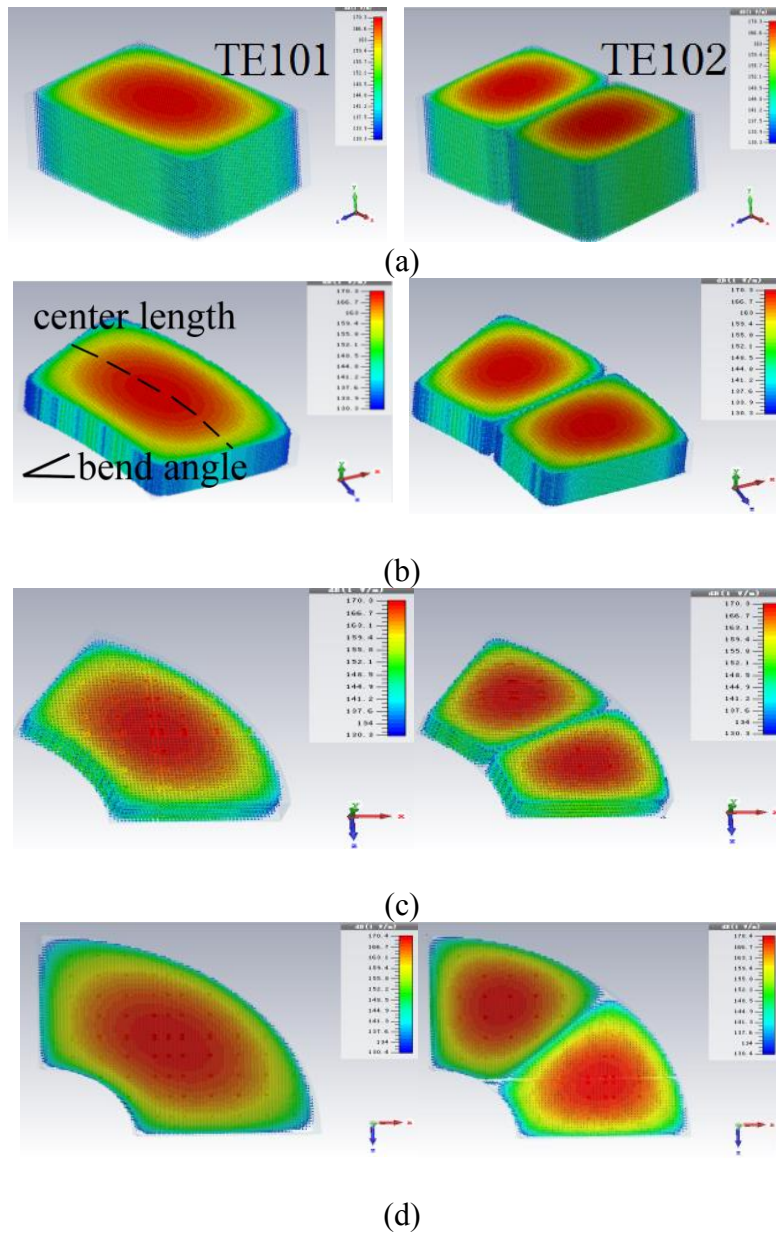


**Figure 5.1** The distributions of electrical fields for resonators. The fundamental mode and the first high order mode of the resonators with (a) 0° (b) 30° (c) 60° and (d) 90° bent in the H-plane.



**Table 5.1** The comparison of frequency for the four H-plane bent resonators.

	$f_{\text{mode1}}/\text{GHz}$	$f_{\text{mode2}}/\text{GHz}$	Ratio ( $f_{\text{mode2}}/f_{\text{mode1}}$ )
0°	7.730	10.502	1.3586
30°	7.733	10.504	1.3583
60°	7.757	10.562	1.3616
90°	7.771	10.583	1.3619

The fundamental mode frequency ( $f_{\text{mode1}}$ ) increases slightly with bend angle. The frequency ratio between the fundamental mode and the first high order mode ( $f_{\text{mode2}}$ ) become marginally greater as the angle increases, except at 30°. The comparison of quality factor  $Q_0$  is shown in Table 5.2. The conductivity used in the simulation is  $5.8 \times 10^7$  S/m. The quality factor  $Q_0$  has no apparent tendency as the angle increases.

**Table 5.2** The comparison of quality factor  $Q_0$  for the four H-plane bent resonators

	$Q_0$ of mode 1	$Q_0$ of mode 2
0°	7522	9534
30°	7933	9826
60°	7556	9396
90°	7571	9329

### **5.2.2 Resonators bent in the E-plane**

Four bent resonators in E-plane are compared with the same center length but different bend angles of  $0^\circ$ ,  $30^\circ$ ,  $60^\circ$  and  $90^\circ$ .

The distributions of electrical fields for different resonators are shown in Figure 5.2.

The fundamental mode in each resonator is  $TE_{101}$  and the first high order mode is  $TE_{102}$ .

The comparison of frequency is shown in Table 5.3.

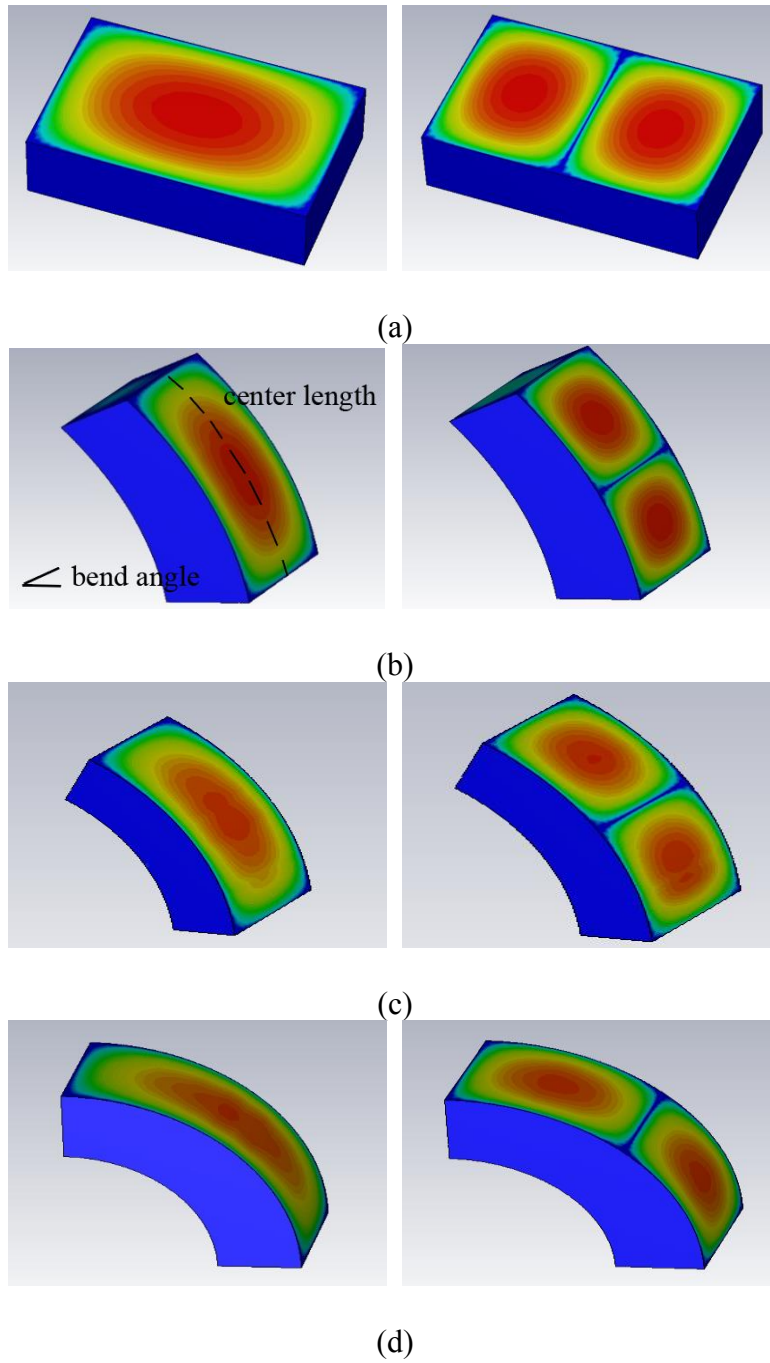


**Figure 5.2** The distributions of electrical fields for resonators bent in E-plane. The fundamental mode and the first high order mode of resonators with (a)  $0^\circ$  (b)  $30^\circ$  (c)  $60^\circ$  and (d)  $90^\circ$  bent in the E-plane.

**Table 5.3** The comparison of frequency for four resonators bent in E-plane.

	$f_{\text{mode1}}/\text{GHz}$	$f_{\text{mode2}}/\text{GHz}$	Ratio ( $f_{\text{mode2}}/f_{\text{mode1}}$ )
0°	7.730	10.502	1.3586
30°	7.727	10.507	1.3598
60°	7.722	10.498	1.3595
90°	7.730	10.488	1.3568

The frequency of the fundamental mode has a slight change without a monotonic tendency. The frequency of the first high order mode becomes smaller as the bend degree increases. The frequency ratio between the fundamental mode and the first high order mode becomes smaller with the degree increasing, except the straight resonator. Table 5.4 shows the comparison of quality factor  $Q_0$  for the four E-plane bent resonators. The conductivity is  $5.8 \times 10^7$  S/m. The quality factor  $Q_0$  has no obvious tendency as the bend degree increases. Compared with the H-plane bent resonators in Table 5.2, the E-plane bent resonators has larger quality factors.

**Table 5.4** The comparison of quality factor  $Q_0$  for the four E-plane bent resonators

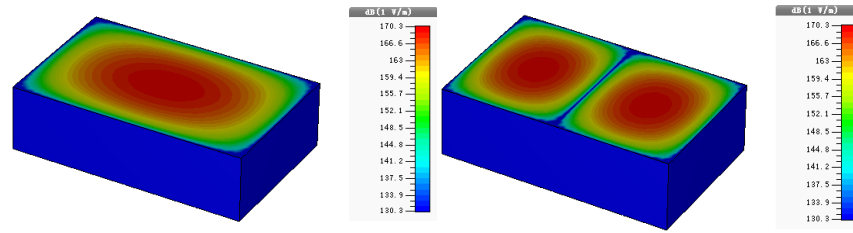
	$Q_0$ of mode 1	$Q_0$ of mode 2
0°	7522	9534
30°	7944	9806
60°	7790	9727
90°	7801	9659

### 5.2.3 Twisted resonators

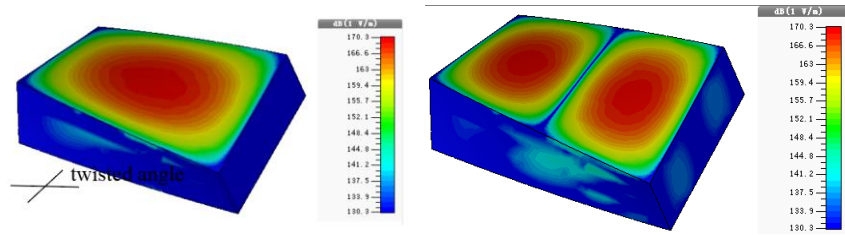
Four twist resonators are compared with the same center length but different twist angles of 0°, 30°, 60° and 90°.

The distributions of electrical fields for different resonators are shown in Figure 5.3.

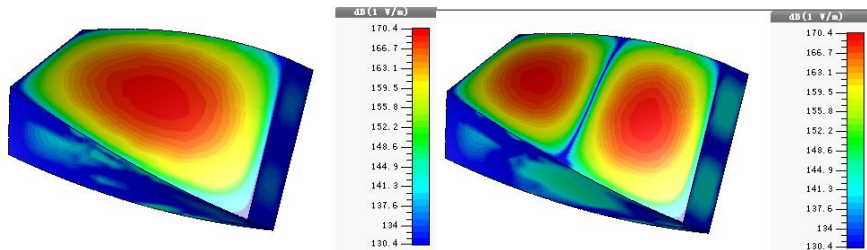
The fundamental mode in each resonator is excited by  $TE_{101}$  and the first high order mode is excited by  $TE_{102}$ . The comparison of different mode is shown in Table 5.5.



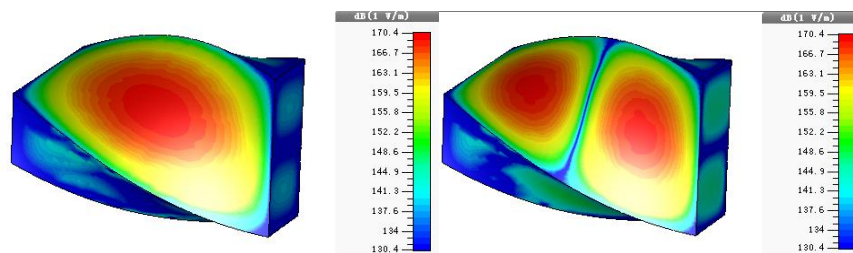
(a)



(b)



(c)



(d)

**Figure 5.3** The distributions of electrical fields for resonators. The fundamental mode and the first high order mode of resonators with (a)  $0^\circ$  (b)  $30^\circ$  (c)  $60^\circ$  and (d)  $90^\circ$  twist.

**Table 5.5** The comparison of frequency for the four twisted resonators

	$f_{\text{mode1}}/\text{GHz}$	$f_{\text{mode2}}/\text{GHz}$	Ratio ( $f_{\text{mode2}}/f_{\text{mode1}}$ )
0°	7.730	10.502	1.3586
30°	7.746	10.493	1.3546
60°	7.796	10.476	1.3438
90°	7.895	10.480	1.3274

The fundamental mode frequency has an increase in frequency with twist angle. The frequency ratio between the fundamental mode and the first high order mode become smaller with the twist degree increasing.

The comparison of quality factor  $Q_0$  is shown in Table 5.6. The conductivity is  $5.8 \times 10^7$  S/m. The quality factor  $Q_0$  has no tendency as the twist degree increases. However, based on previous tables, the quality factors of twist resonators are smaller than the E/H-plane bent resonators obviously. It means the E/H-plane bent structure has smaller effect than the twist structure.

**Table 5.6** The comparison of quality factor  $Q_0$  for the four twist resonators

	$Q_0$ of mode 1	$Q_0$ of mode 1
0°	7522.1	9533.7
30°	5663.9	8766.0
60°	6995.3	7405.0
90°	6456.2	7441.3

### 5.3 U band waveguide bandpass filter

The 4<sup>th</sup> order filter is designed to have a Chebyshev response with a center frequency of 54 GHz, a bandwidth of 11.11% (6 GHz), and a return loss in the passband of 20 dB. Both U and V bands can cover the passband range (51-57 GHz). However, the standard size of the waveguide ports for U band and V band are different. To decrease the difficulty of fabrication, large size is considered at first. The U band rectangular waveguide is applied to this filter, with 4.7752 mm × 2.3876 mm in cross section.

#### 5.3.1 Design of the twist filter

A twist filter is designed, and the effect of round corners is considered at the end. The configuration of the internal structure is shown in an air model of Figure 5.4. The twist filter is composed of four equally and sequentially rotated TE<sub>101</sub> waveguide resonators. The uniform twist angle  $Ta$  is 22.5° for each twist cavity. The total twist angle for the filter is 90° which gives orthogonal polarizations between the two ports. Sharp corners



are assumed at this stage of the design.

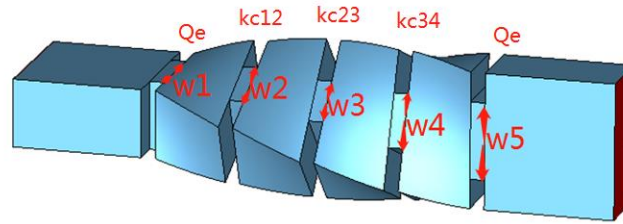


**Figure 5.4** Configuration of the internal structure of the U-band twist filter

This filter is designed using the coupling matrix approach described in [24]. To meet the specification, the external quality factor  $Q_e$  and coupling coefficients are calculated to be  $Q_{e1} = Q_{e5} = 8.3826$ ,  $k_{12} = k_{34} = 0.1013$ ,  $k_{23} = 0.0778$ . Figure 5.5 (a) shows the relationship between  $Q_{e1}$  (or  $Q_{e5}$ ) and  $w_1$  (or  $w_5$ ) of the inductive iris at the source and load. The coupling coefficient  $k_{12}$  (or  $k_{34}$ ) can be controlled by widths  $w_2$  and  $w_4$  respectively, as shown in Figure 5.5 (b). The coupling coefficient  $k_{23}$  can be controlled by widths  $w_3$  as shown in Figure 5.5 (b). The initial dimensions of the twist filter can be obtained. The final responses are shown in Figure 5.6 after optimization.

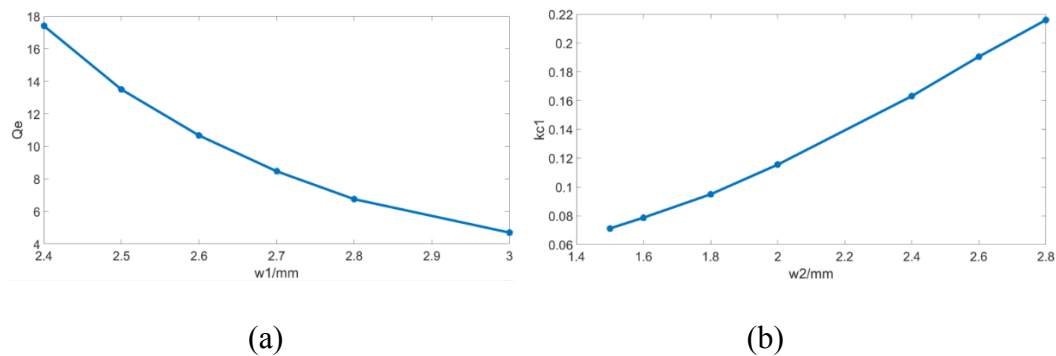


**Figure 5.5** (a) External quality factor  $Q_{e1}$  (or  $Q_{e5}$ ) versus the dimension  $w_1$  (or  $w_5$ ). (b) Coupling coefficients  $k$  versus the widths  $w$

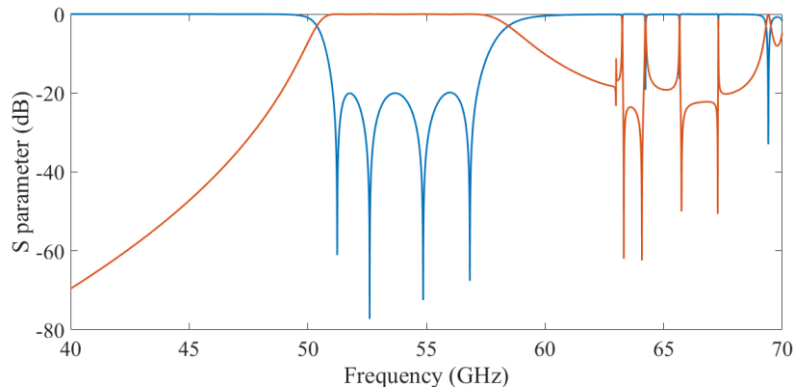


**Figure 5.6** The final responses of the twist filter

As shown in Figure 5.6, the filter is centred at 54.10 GHz with an 11.26% bandwidth (6.091 GHz). It is also shown that some spurious transmission peaks occur at around 65 GHz. These unwanted transmission peaks are because of the high order modes in each cavity.

In practical fabrication process, the corners and edges are close to round because of some internal supporting structure. Round corners and edges are added for the twist waveguide filter as shown in Figure 5.7. The radius of the corner in the cavities is 0.5 mm. The radius of the corner in iris is 0.15 mm. The optimized results are shown in Figure 5.8. The filter is centred at 54.11 GHz with an 11.29% bandwidth (6.11 GHz). The return loss is better than 20.52 dB in the passband.

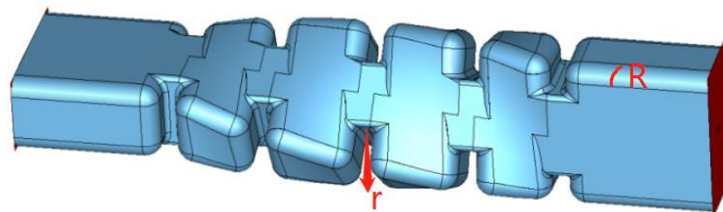


**Figure 5.7** Configuration of the internal structure of the twist filter with round corners and edges

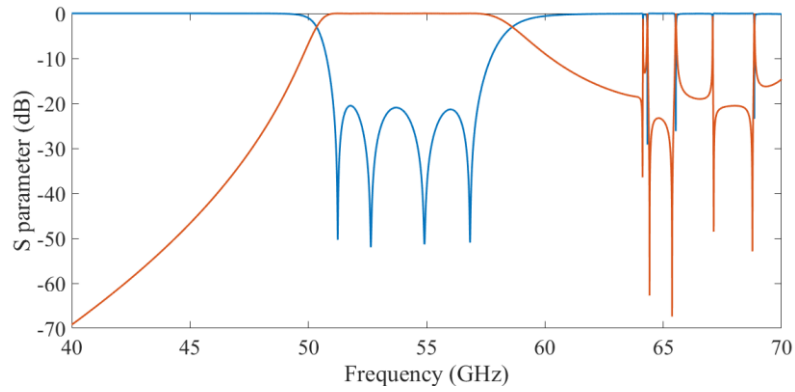


**Figure 5.8** Optimized  $S$  parameters for the twist filter with round corners and edges

### 5.3.2 Twist filter with different bent angle

Based on the previous results, the internal structure of a waveguide bandpass filter consisting of a  $90^\circ$  uniform bend and a uniform  $90^\circ$  twist is given in Figure 5.9. The  $S$  parameters are shown in Figure 5.10. Bending has slight effect on the performance, no more optimization is needed. The filter is centred at 54.11 GHz with an 11.22% bandwidth (6.07 GHz). The return loss is better than 20.62 dB in the passband.

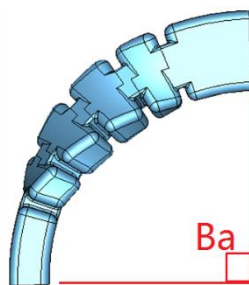


**Figure 5.9** Configuration of the internal structure of the twist filter with a uniform  $90^\circ$  bend

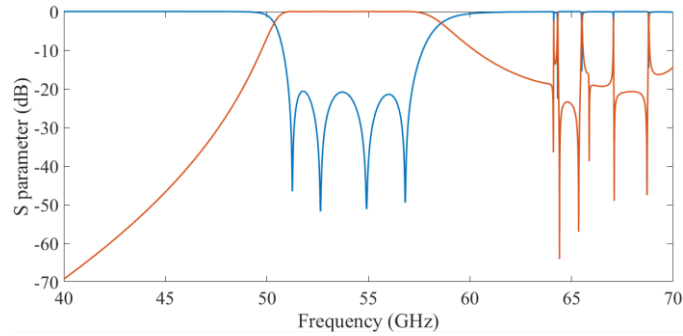


**Figure 5.10**  $S$  parameters for the twist filter with a uniform  $90^\circ$  bend

To compare the performance of filters with different bend angles, the filters in Figure 5.4 are bent with different angles. Round corners are not considered here to reduce the complexity of calculation. Figure 5.11 (a) shows the internal structure of a waveguide bandpass filter consisting of an H-plane  $90^\circ$  uniform bend and a uniform  $90^\circ$  twist. Figure 5.11 (b) shows the internal structure of the filter consisting of a  $180^\circ$  uniform bend and a uniform  $90^\circ$  twist.

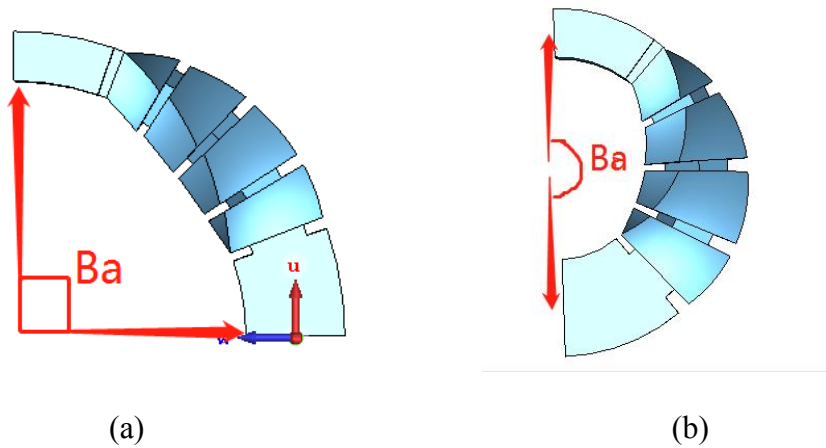


**Figure 5.11** The internal structures of waveguide bandpass filters. (a) Filter consisting of a  $90^\circ$  uniform bend and a uniform  $90^\circ$  twist. (b) Filter consisting of a  $180^\circ$  uniform bend and a uniform  $90^\circ$  twist.

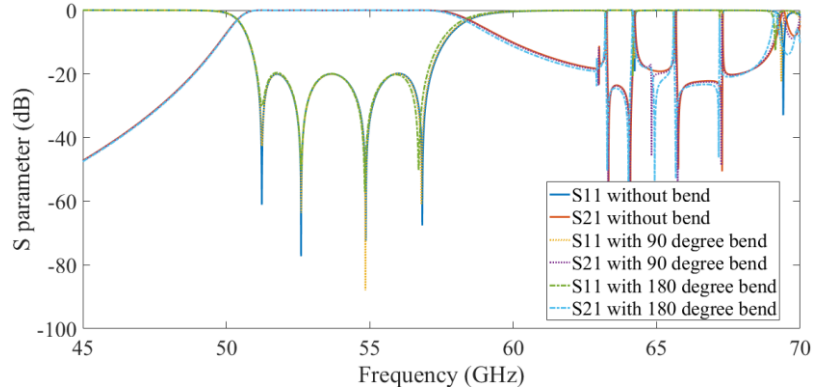


**Figure 5.12** The  $S$  parameters for the filters with  $0^\circ$  bend (straight),  $90^\circ$  bend and  $180^\circ$  bend angles.

The  $S$  parameters for the filters with  $0^\circ$  bend (straight),  $90^\circ$  bend and  $180^\circ$  bend are compared in Figure 5.12. Different bend angles do not change the bandwidth and center frequency dramatically.

### 5.3.3 Different twist angles of each cavity

For the filters in above section, the twist angle for each cavity  $Ta_1 = Ta_2 = Ta_3 = Ta_4 = 22.5^\circ$  as shown in Figure 5.4. Keeping the total twist angle  $90^\circ$ , here I have changed the twist angle of each cavity to find how the twist angle affects the bandwidth and the center frequency.

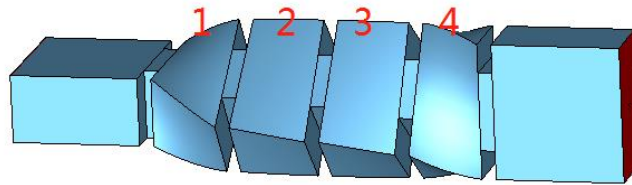


**Figure 5.13** Configuration of the internal structure of the twist filter ( $Ta_1 = Ta_4 = 35^\circ$ ,  $Ta_2 = Ta_3 = 10^\circ$ )

The green curve in Figure 5.14 is the  $S_{11}$  for the filter with  $Ta_1 = Ta_2 = Ta_3 = Ta_4 = 22.5^\circ$ .

The red curve is the  $S_{11}$  for the filter with  $Ta_1 = Ta_4 = 10^\circ$ ,  $Ta_2 = Ta_3 = 35^\circ$ . The black curve is the  $S_{11}$  for the filter with  $Ta_1 = Ta_4 = 35^\circ$ ,  $Ta_2 = Ta_3 = 10^\circ$ , which structure is shown in Figure 5.13.

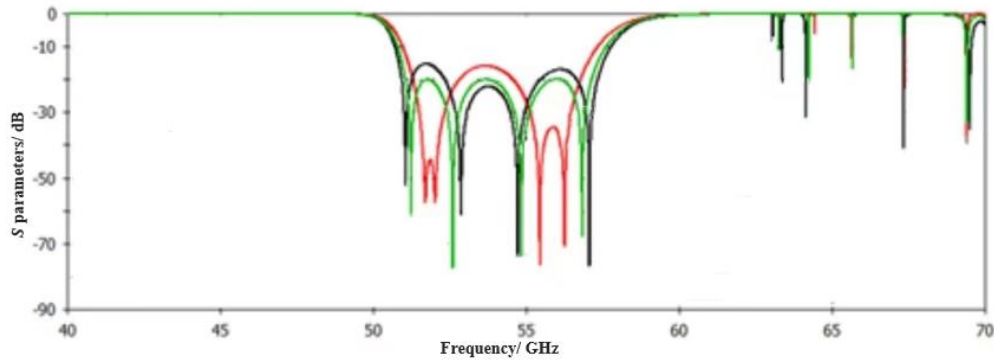


**Figure 5.14** The  $S_{11}$  for the filters with different twist cavities

The twist angle does not change the center frequency dramatically, because the center frequency is mainly controlled by the length of cavity. However, it has an effect on the reflection poles. Larger twist angle for the middle two resonators makes the middle two poles away from each other.

### 5.3.4 Suppress the spurious modes

As shown in above sections, the designed filters show poor performance above the passband. Methods are introduced to improve the stopband performance for the filter. By using a  $90^\circ$  twisted coupling geometry in a waveguide filter [41], the stopband rejection was improved because of the reduced coupling strength of the spurious  $TM_{211}$  mode. Mathematically defined super-ellipsoid resonators presented in [42] and [43] show excellent selectivity performance. Spherical resonator bandpass filter is designed with spurious suppression by cutting slots [44]. It is achieved by interrupting surface current of the spurious modes with slots. This method is applied to the twist filter.

The surface current distributions at different frequencies of a twist straight filter are shown in Figure 5.15. Figure 5.15 (a) is the surface current distribution in the passband. The current direction at the middle of port is parallel the propagation direction. Figure 5.15 (b) is the surface current distribution out of the passband. The current direction is vertical to the propagation direction. The slots are appropriately arranged on the cavity shells to ensure that the spurious  $TE_{01}$  mode is suppressed and the fundamental  $TE_{101}$  mode is not disturbed. The slots are parallel to the  $TE_{101}$  mode surface current but intersect the currents of the spurious mode as shown in Figure 5.16. The  $S$  parameters for the twist filter with slots are shown in Figure 5.17. Compared with the filter without slots, the stopband performance is much improved. There are still some small ripples around 65 GHz. This is because the slots cannot realize perfect suppression.

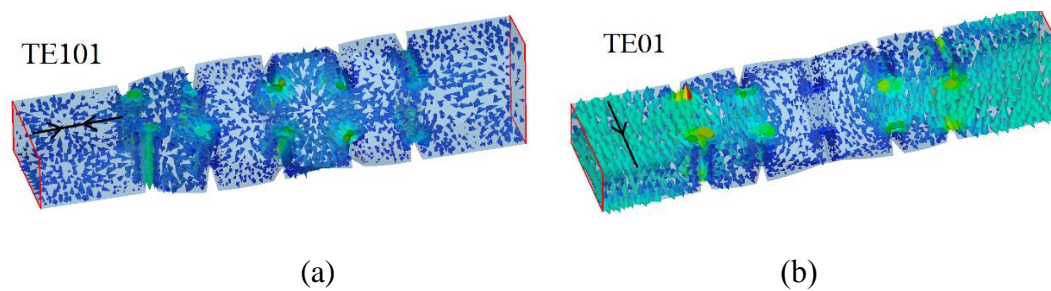


**Figure 5.15** Surface current distributions at (a) 54 GHz and (b) 63.256 GHz

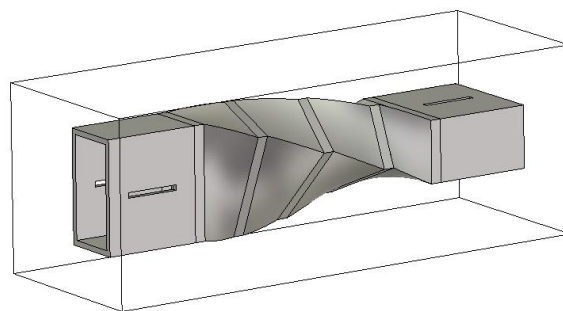


**Figure 5.16** Cavity shells for the 4<sup>th</sup> order twist filter with slots on ports

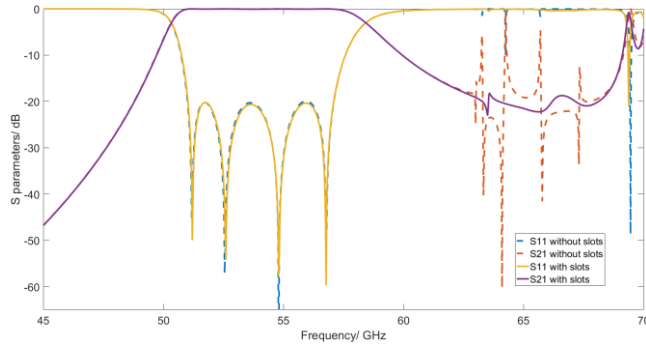


**Figure 5.17** The comparison of  $S$  parameters between the filter with and without slots.

In the fabrication process, additional support structures are needed to connect the flange and the waveguide port. As shown in Figure 5.16, the slots are on the waveguide ports, which lead to difficulty for adding support structure on the ports. In the following, two different slot structures are compared. The slots are on the middle of each resonator in Figure 5.18 (a). The optimized results are shown in Figure 5.18 (b). The slot is along the middle line in Figure 5.19 (a). The optimized results are shown in Figure 5.19 (b). The slot along the middle line shows better stopband performance after comparison.

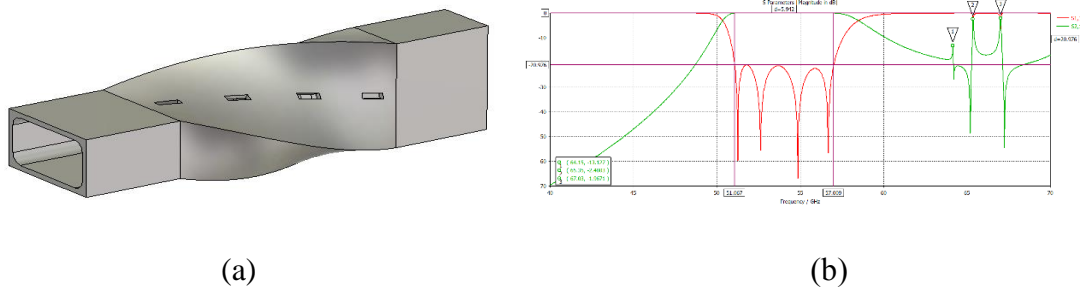


**Figure 5.18** (a) Cavity shell for the smooth twist filter with slots on the resonators. (b)  $S$  parameters for the smooth twist filter with slots on the resonators.



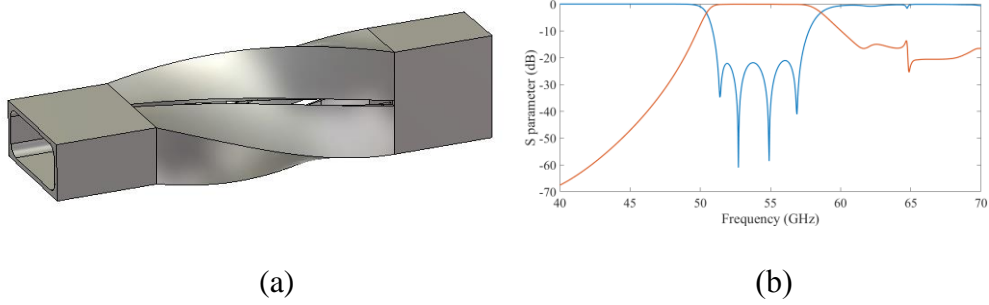


**Figure 5.19** (a) Cavity shell for the smooth twist filter with slots along the middle line. (b)  $S$  parameters for the smooth twist filter with slots on the middle line.

For the filter in Figure 5.19, the width of the middle slot slightly influences the performance. The passband has a slight right shift as the width increases. The  $S$  parameters for the filter with different slot widths (0.1 - 0.5 mm) are shown in Figure 5.20.

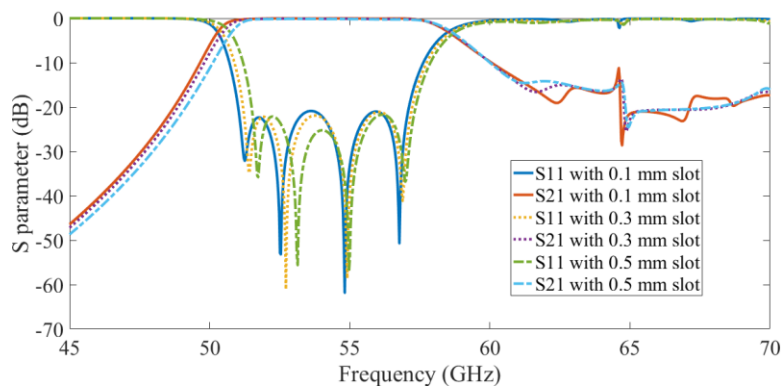


**Figure 5.20**  $S$  parameters for the filter with different slot widths

## 5.4 V band waveguide bandpass filter

Another possible reason for the spurious modes is that the passband is too close to the upper band edge of the U band (40 - 60 GHz). For a standard waveguide, only the wave in specific frequency range can pass the waveguide with few losses. There are lots of

spurious passband at the outside of working passband. Therefore, a filter working at 60 GHz (V band) is re-designed and fabricated.

#### 5.4.1 Design and measurement

The bandwidth is designed to be 3 GHz. To meet the specification, the external quality factor  $Q_e$  and coupling coefficients are calculated to be  $Q_{e1} = Q_{e5} = 18.63$ ,  $k_{12} = k_{34} = 0.0456$ ,  $k_{23} = 0.035$ . Figure 5.21 (a) shows the relationship between  $Q_{e1}$  (or  $Q_{e5}$ ) and  $w_1$  (or  $w_5$ ) of the inductive iris at the source and load. The coupling coefficient  $k_{12}$  (or  $k_{34}$ ) can be controlled by widths  $w_2$  and  $w_4$  respectively, as shown in Figure 5.21 (b). The coupling coefficient  $k_{23}$  can be controlled by widths  $w_3$  as shown in Figure 5.21 (b). The initial dimensions of the twist filter can be obtained. The final responses are shown in Figure 5.22 after optimization.

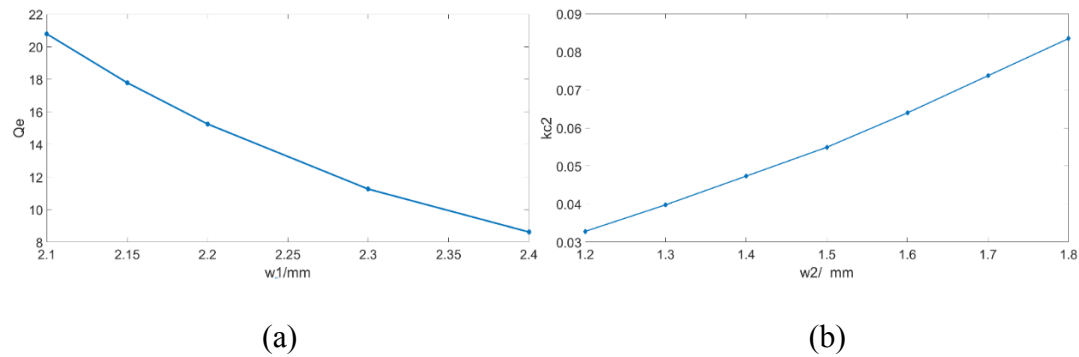


**Figure 5.21** (a) External quality factor  $Q_{e1}$  (or  $Q_{e5}$ ) versus the dimension  $w_1$  (or  $w_5$ ). (b) Coupling coefficients  $k$  versus the widths  $w$ .

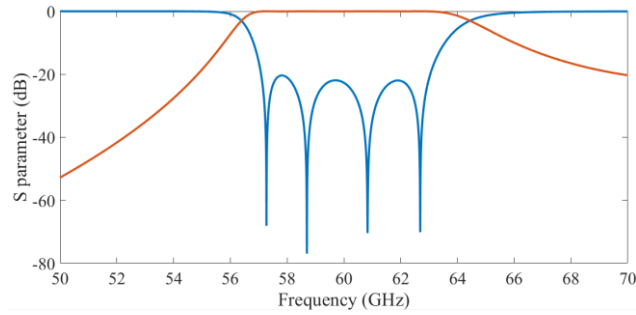


**Figure 5.22** The optimized responses of the V band filter.

Round corners and edges are added for the twist waveguide filter as shown in Figure 5.23. The radius of the corner in cavity is 0.5 mm. The radius of the corner in iris is 0.2 mm.

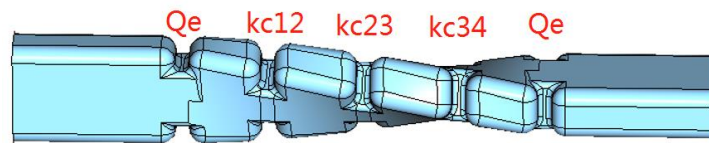


**Figure 5.23** Configuration of the internal structure of the twist filter with round corners.

This filter is manufactured using MLS (micro laser sintering) process by external company (3D MicroPrint GmbH, <http://www.3dmicroprint.com/>). The material is stainless steel 316L. The laser power is 50W and the spot-size is  $25\mu\text{m}$ . Powder particles with grain size of  $D_{90} < 5\mu\text{m}$  are used and the layer thickness is  $7\mu\text{m}$ . The photograph of the original filter is shown in Figure 5.24 (a). The measurement is shown in Figure 5.24 (b). To reduce the losses, a gold plating with nickel undercoat was applied to improve the performance. The thickness of gold is about  $3\mu\text{m}$ . Figure 5.24 (c) is the filter after gold coating.

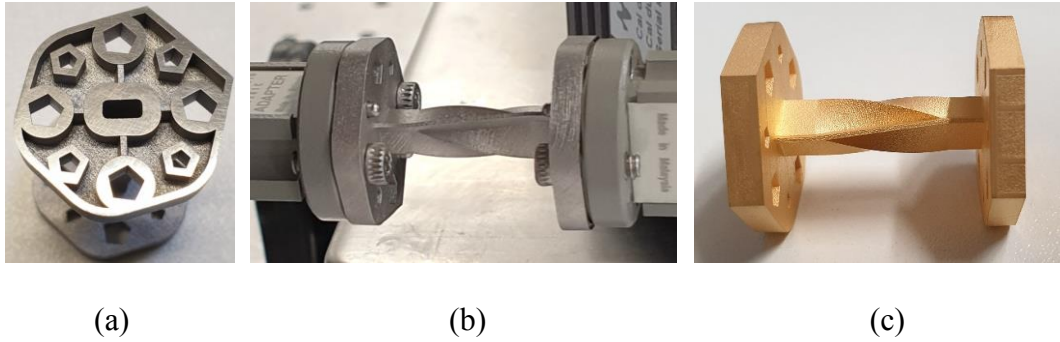


**Figure 5.24** (a) The photograph of the original filter. (b) The measurement of the original filter. (c) The photograph of the gold coated filter.

The original filter and the gold coated filter are measured using VNA without any tuning. The measured results of the original filter are the dash-dot lines shown in Figure 5.25. The filter is centred at 60.17 GHz. The return loss is better than 18.65 dB in the passband. The minimum insertion loss is 1.33 dB. The measurements have a good agreement with simulated results. The difference is because the low conductivity of the printed material (stainless-steel) and the surface roughness. The measured results of the gold coated filter are shown as the solid lines in Figure 5.25. The filter is centred at 60.49 GHz. The return loss is better than 16.4 dB in the passband. The minimum insertion loss is 0.32 dB. Compared with the original filter, the passband of the gold coated filter moves up about 325 MHz. It is due to the gold cladding inside the filter structure. It makes the cavities of filter slightly smaller than before. The insertion loss of the gold coated filter is reduced dramatically, which proves the low conductivity of the printed material is the main reason of the high insertion loss of the original filter.

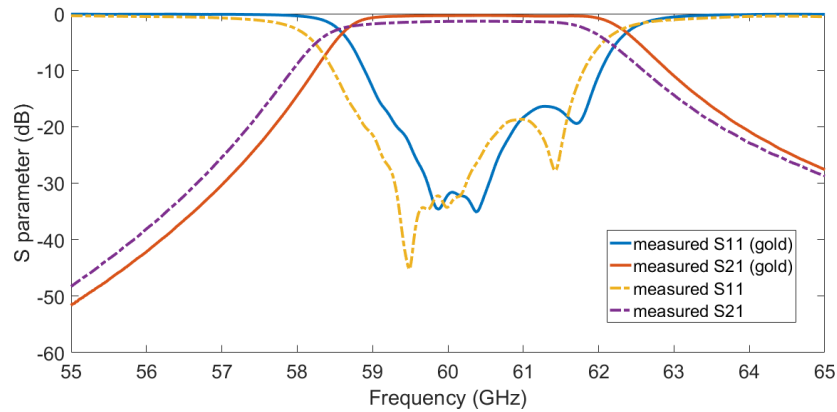


**Figure 5.25** The comparison between the measured results of the original filter and the gold coated filter.

#### 5.4.2 Analysis of internal surface roughness

The internal surface roughness is estimated. The first step is using the parameter calculator in CST to get the effective electric conductivity of stainless-steel and gold. The effective conductivity is calculated by conductivity and surface roughness. The electrical conductivity of stainless-steel is  $1.35 \times 10^6$  S/m and that of gold is  $4.56 \times 10^7$  S/m. Surface roughness can be set as a predicted value in the calculator. Then the effective conductivity can be obtained. The second step is using the effective conductivity, obtained from above step, in filter simulation. The surface roughness should be set as zero in simulation, because the effective conductivity is used. The third step is comparing the insertion loss of simulated results with the measured results. The simulated insertion loss should be the same as the measured insertion loss when the predicted surface roughness in step 1 is the same as the real surface roughness.

After many time prediction and simulation, the internal surface roughness is estimated about  $1.4 \mu\text{m}$  for the original filter and the gold coated filter. The surface roughness

degraded the stainless-steel conductivity to  $6.35 \times 10^5$  S/m from theoretical conductivity of  $1.35 \times 10^6$  S/m. The surface roughness degraded the gold conductivity to  $1.17 \times 10^7$  S/m from theoretical conductivity of  $4.56 \times 10^7$  S/m. Figure 5.26 (a) shows the comparison between the measured responses of the original filter and the simulated responses with  $1.4 \mu\text{m}$  internal surface roughness. The minimum insertion loss of the simulated results is 1.32 dB which is comparable to the measured insertion loss (1.33 dB).

The measured responses of the gold coated filter and the simulated responses with  $1.4 \mu\text{m}$  internal surface roughness is shown in Figure 5.26 (b). The minimum insertion loss of the simulated results is 0.36 dB which is again close to the measured insertion loss of the gold coated filter.

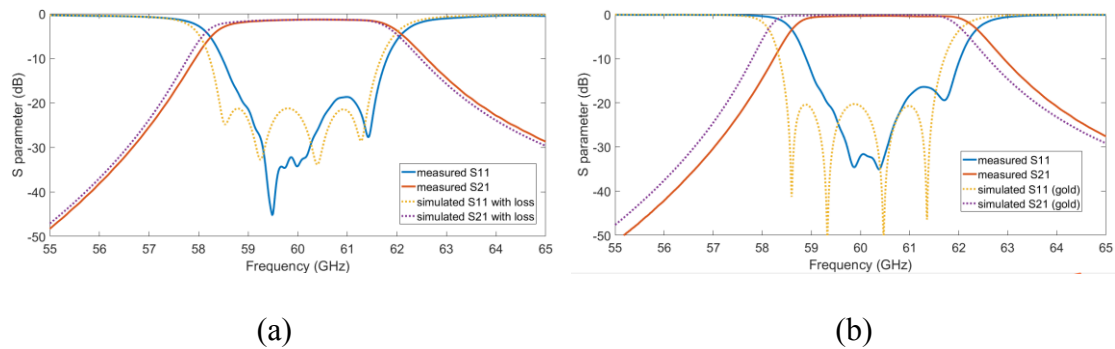


**Figure 5.26** The comparison between the measured results and the simulated results with  $1.4 \mu\text{m}$  surface roughness for (a) original filter and (b) gold coated filter.

The surface roughness was measured as  $2.2 \mu\text{m}$  using Alicona G4 InfiniteFocus optical system at different locations on the outside surface of the filter and the average value was taken. The simulation results in Figure 5.27 show a minimum insertion loss of 1.6 dB for the original stainless steel filter, which is close to the measured insertion loss of

1.3 dB. However, the simulated insertion loss is a little bit larger than the measured insertion loss, which means the real internal surface roughness is smaller than outside surface roughness  $2.2 \mu\text{m}$ .

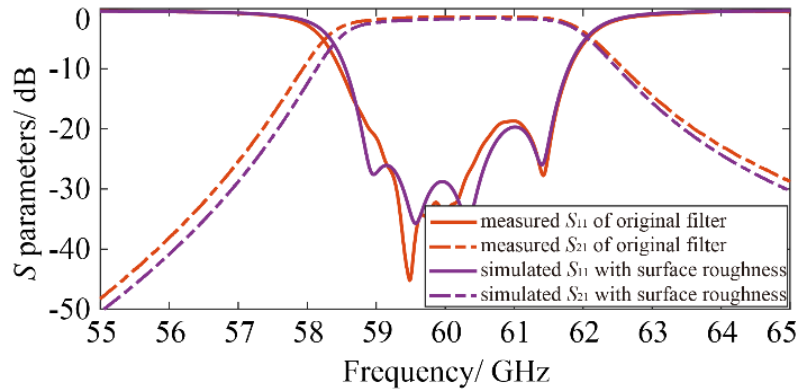


**Figure 5.27** The comparison between the measured results and the simulated results with  $2.2 \mu\text{m}$  surface roughness for original filter.

## 5.5 Summary

After analyzing the performance of different bent and twist resonators, a U-band filter is designed. Filters with different bent angles are compared. Spurious modes are suppressed by cutting slots on the shell. After that, a V band filter is designed and fabricated. The measurement is good. However, the low conductivity of the material and internal surface roughness lead to large losses. Therefore, the original filter is coated with gold. The measured results have a good agreement with the simulated results. The results in this chapter show the great potential of 3D printing for the devices working at 60 GHz or higher frequency.

# Chapter 6 Triangular resonators and waveguide bandpass filters

The benefits of 3D printing technology have been shown in Chapter 5. In the process of manufacturing the filter, there will be an inclined angle between the filter and the horizontal platform to avoid overhang structure and internal support structures. However, it still requires external support structures. As shown in Figure 6.1, the blue lines represent the supporting materials outside the filter in Chapter 5.

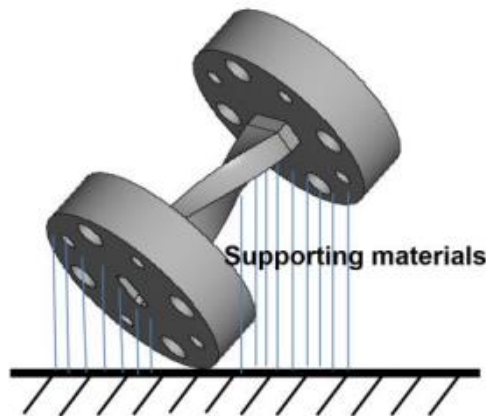


**Figure 6.1** Diagram of the filter with supporting structures in fabrication process.

These additional support structures will be no longer needed if the resonators are triangular with appropriate angle range. As shown in Figure 6.2, the specific angle  $\theta$  between the side walls and horizontal platform should be between  $45^\circ$  and  $60^\circ$ . In literature, there are many works about microstrip triangular-patch resonator. In [45] and [46], single-mode operates in the triangular-patch resonator. In [47] and [48], dual-modes operates in the triangular-patch resonator. However, there are few works about



waveguide triangular resonator [49]. The main reason is the fabrication difficulty of waveguide triangular resonators using traditional technologies. Recently, the application of 3D printing makes the fabrication of waveguide triangular resonators become easier. In this Chapter, a feasibility study of waveguide triangular resonators is presented and a 3<sup>rd</sup> order waveguide bandpass filter with isosceles triangular resonators is manufactured using 3D printing technology. Section 6.1 is devoted to comparing the performance of different triangular resonators. Section 6.2 presents the design of a 2<sup>nd</sup> order waveguide filter, which is improved and revised to a 3<sup>rd</sup> order filter as demonstrated in Section 6.3. The analysis of the 3<sup>rd</sup> order filter is also presented in Section 6.3. Section 6.4 shows the fabrication and measured results. Finally, Section 3.5 describes the fabrication and measurement of this filter.

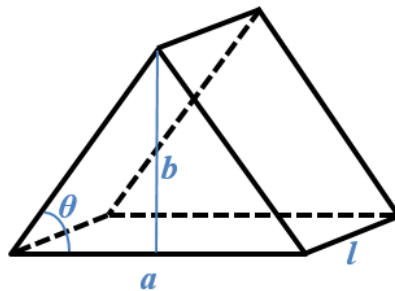


**Figure 6.2** Diagram of the isosceles triangular resonator.  $a$ ,  $b$ , and  $l$  are the width, height, and length of resonator, respectively.

## 6.1 Triangular resonators

Isosceles triangular resonators are special because of the symmetric shape, which reduce the difficulty to analyze the electric field and other performance. In the following, different isosceles triangular resonators ( $\theta = 45^\circ, 50^\circ, 55^\circ$  and  $60^\circ$ ) with the same length and volume are analyzed. The electric fields of the fundamental mode, the 1<sup>st</sup> and the

2<sup>nd</sup> high order mode of different isosceles triangular resonators are shown in Figure 6.3. As shown in Figure 6.3 (a)-(c), mode 1 and mode 2 of the isosceles triangular resonators are two degenerate modes. Mode 3 is a TM mode which is parallel to the transmission direction and might not be excited in a real filter. One can also observe in Figure 6.3 (d) that the direction of the two degenerate modes of the equilateral triangular resonator can be rotated to each other by  $\pm 60^\circ$ . In theoretical, the work frequencies of the degenerate modes are the same.

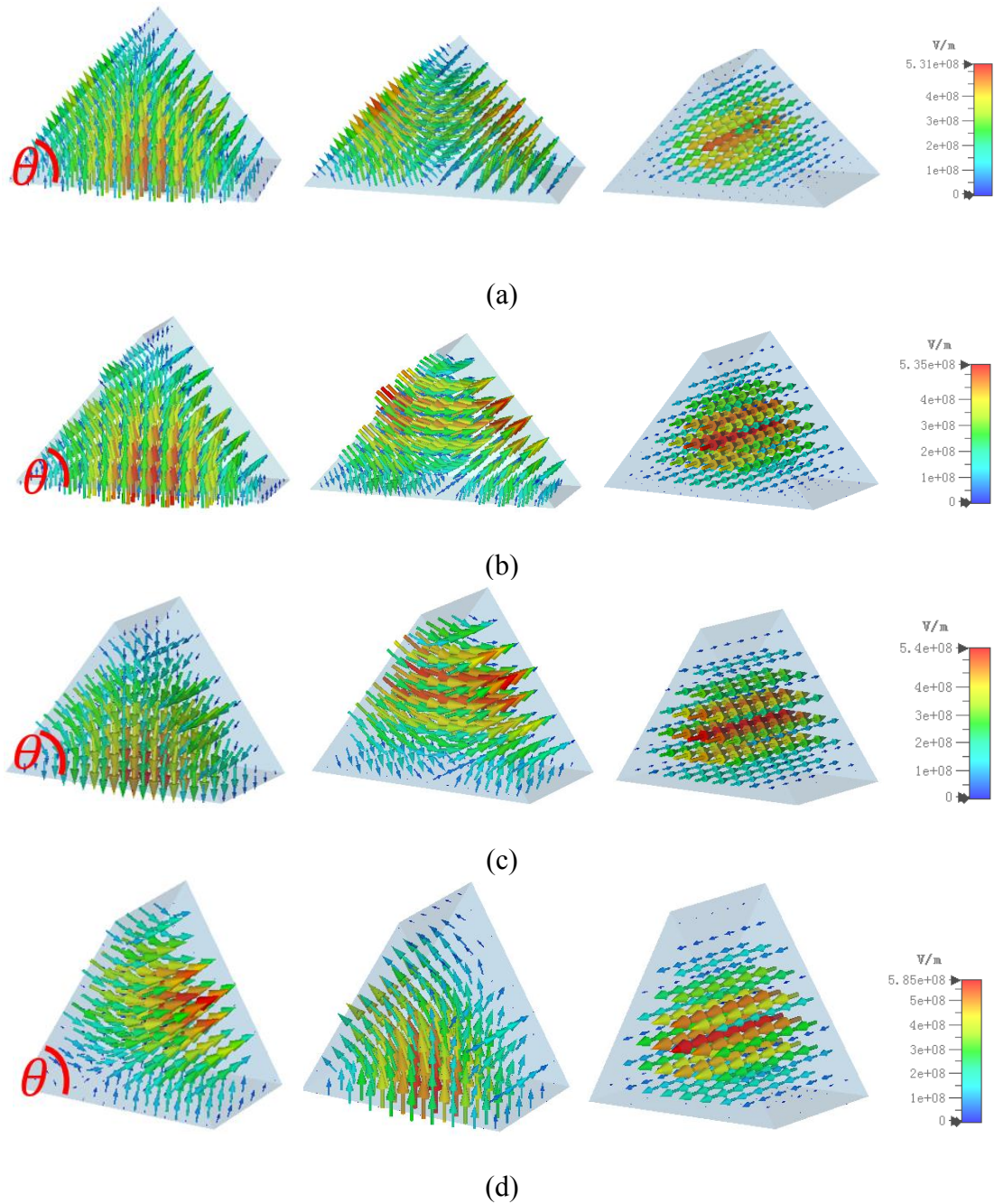


**Figure 6.3** The electric fields of the fundamental mode, the 1<sup>st</sup> and the 2<sup>nd</sup> high order mode of isosceles triangular resonators with (a)  $\theta = 45^\circ$ , (b)  $\theta = 50^\circ$ , (c)  $\theta = 55^\circ$  and (d)  $\theta = 60^\circ$ .

**Table 6.1** The frequency and quality factor of different isosceles triangular resonators ( $\theta = 45^\circ, 50^\circ, 55^\circ, 60^\circ$ ). Copper is used to calculate the value of  $Q$ .

Degree	Mode 1 frequency (GHz)	Mode 2 frequency (GHz)	Mode 3 frequency (GHz)	$Q$ of mode 1	$Q$ of mode 2	$Q$ of mode 3
45°	12.62	14.47	15.80	6457.6	6474.7	8014.9
50°	12.92	14.35	15.47	6706.5	6962.1	8167.9
55°	13.26	14.05	15.26	6926.0	7190.5	8258.0
60°	13.65	13.65	15.19	7126.3	7125.3	8289.0

The frequency and quality factor of each mode in different resonators are shown in Table 6.1. Copper (electric conductivity is  $5.8 \times 10^7$  S/m) is used to calculate the quality factor in parameter calculator in CST. Figure 6.4 and Figure 6.5 plot the frequency and quality factors, respectively.

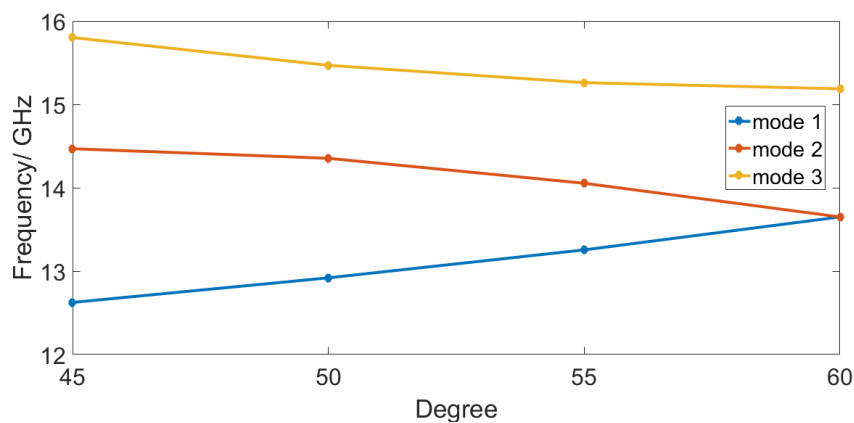


**Figure 6.4** The frequency of the fundamental mode, the 1<sup>st</sup> and the 2<sup>nd</sup> high mode in different isosceles triangular resonators.

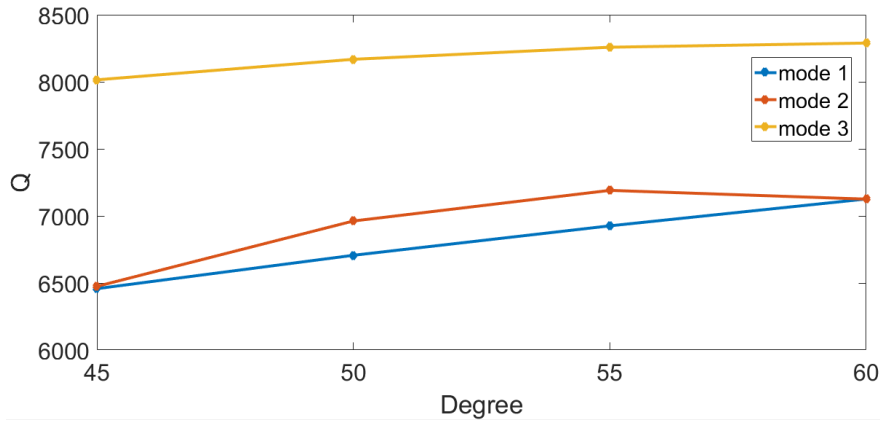


**Figure 6.5** The quality factor of each mode in different isosceles triangular resonators.

As shown in Figure 6.4, the frequency of mode 1 and mode 2 are the same in equilateral triangular resonator ( $\theta = 60^\circ$ ). This mode will be split into two modes [17] by breaking the symmetry of the equilateral into isosceles triangular resonators ( $\theta = 45^\circ, 50^\circ, 55^\circ$ ). The quality factor of mode 1 and mode 2 are nearly equal when the angle is  $45^\circ$  and  $60^\circ$ .

Comparing with the standard rectangular resonator with the same volume, the equilateral triangular resonator shows smaller quality factors as shown in Table 6.2. Aluminium (electric conductivity is  $3.56 \times 10^7$  S/m) is used to calculate the quality factor.

**Table 6.2** Quality factor of the standard rectangular resonator and equilateral triangular resonator with the same volume. Aluminium is used in calculation.

Shape of resonator	$Q$ of mode 1	$Q$ of mode 2	$Q$ of mode 3
Rectangular	5822.3	5903.2	7330.0
Equilateral triangular	5584.6	5582.1	6494.9

## 6.2 Design of the 2<sup>nd</sup> order BPF

As shown in Figure 6.4, the frequency of the fundamental mode, the 1<sup>st</sup> high order mode, and the 2<sup>nd</sup> high order mode are separated in isosceles triangular resonators ( $\theta = 45^\circ$ ). It is easy to design a 2<sup>nd</sup> order filter utilizing the fundamental mode. The diagram of the filter is shown in Figure 6.6. The whole structure is symmetrical along  $Z$  direction and all the irises and resonators are isosceles right triangular ( $\theta = 45^\circ$ ).

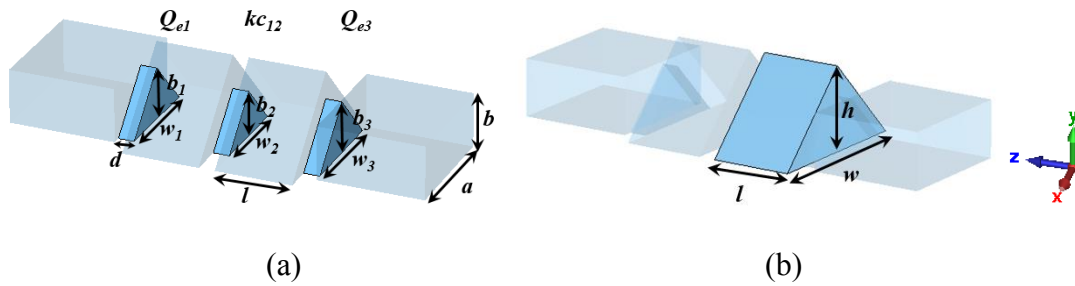


**Figure 6.6** Diagram of the 2<sup>nd</sup> order filter. (a) The triangular irises. (b) The isosceles right triangular resonators ( $\theta = 45^\circ$ ).  $a = 22.86$  mm,  $b = 10.16$  mm.

The 2<sup>nd</sup> order filter is designed to have a Chebyshev response with a center frequency of 10 GHz, a bandwidth of 5% (0.5 GHz), and a return loss in the passband of 20 dB. The external quality factor  $Q_e$  and coupling coefficients are calculated to be  $Q_{e1} = Q_{e3} = 13.297$ ,  $kc_{12} = 0.0831$ . The design process is the same as the filter designed in previous chapters. The optimized dimensions are shown in Table 6.3. The simulated results are shown in Figure 6.7. The center frequency of the passband is at 9.99 GHz. However, there is an undesired passband near the designed passband, which appears because the TM modes in the resonator are close to the passband.

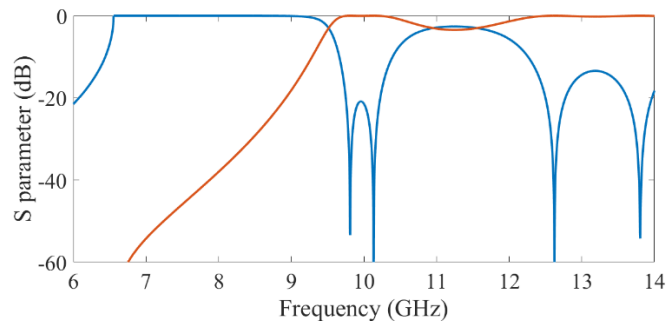


**Figure 6.7** The simulated results of the 2<sup>nd</sup> order filter with isosceles triangular resonators ( $\theta = 45^\circ$ ).

**Table 6.3** The optimized dimensions of the 2<sup>nd</sup> order filter with isosceles triangular resonators ( $\theta = 45^\circ$ ).

$w_1$ ( $w_3$ ) (mm)	$w_2$ (mm)	$b_1$ ( $b_3$ ) (mm)	$b_2$ (mm)	$d$ (mm)	$l$ (mm)	$h$ (mm)	$w$ (mm)
19.6	17.1	9.8	8.55	3	14.4	15	30

### 6.3 Design of the 3<sup>rd</sup> order BPF

Because there is an undesired spurious passband near the designed passband due to the high order mode, improvements in selectivity are needed to combat the undesired passband. As shown in Section 6.1, transforming the equilateral into isosceles triangular resonators can be considered as a slight change. The mode will be split into two modes when the resonator changes from equilateral to isosceles. The angle  $\theta$  or the height of resonator  $h$  have a big effect on the split of modes. When  $\theta$  is close to  $60^\circ$ , the split of mode is smaller. In the 2<sup>nd</sup> order filter, isosceles right triangular resonators are used ( $\theta = 45^\circ$ ). The height of resonator  $h$  is adjusted to change the passband.

As the height increases, the high order mode shift to lower frequency and near to the fundamental mode. A new passband appears around the center frequency when the triangle is approximate equilateral triangle ( $h = 25$  mm) as shown in Figure 6.8.

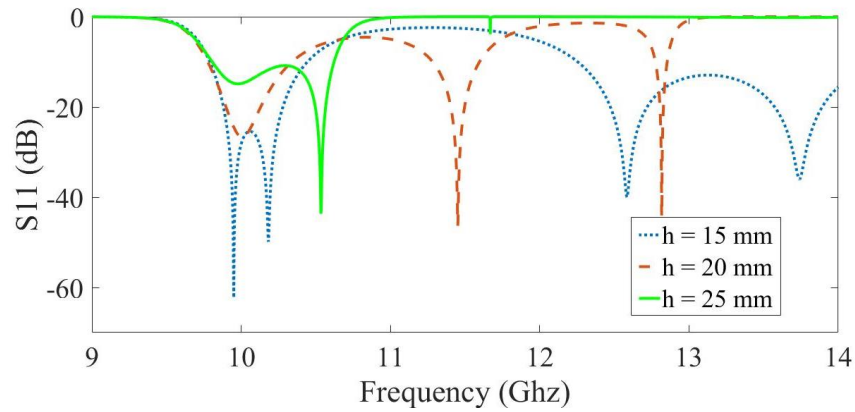


**Figure 6.8** Simulated  $S_{11}$  with different height of resonator  $h$ .

The diagram of the 3<sup>rd</sup> order filter is shown in Figure 6.9. The whole structure is symmetrical. The  $\theta$  is close to  $60^\circ$  and the triangles are close to equilateral. The width of the middle iris  $w_2$  is adjusted to change the coupling between the modes. After optimization, the simulated results are shown in Figure 6.10. This filter has 3 poles and one transmission zero near the passband, which has good selectivity. The filter is centred at 10.04 GHz with an 8.50% bandwidth (0.85 GHz). The return loss is better than 18.83 dB in passband. The optimized dimensions are shown in Table 6.4.



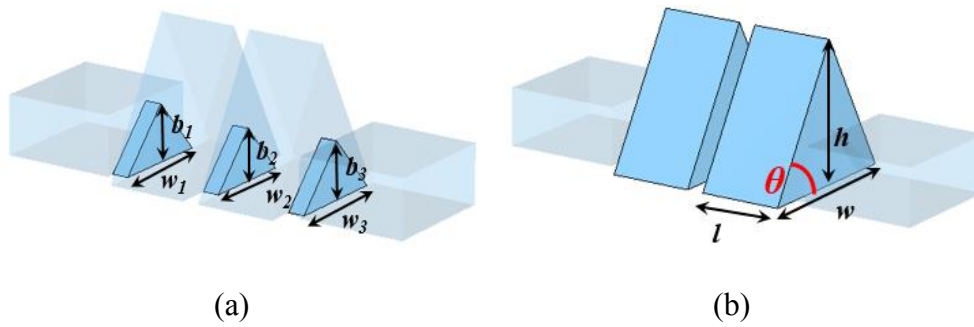


**Figure 6.9** The diagram of the 3<sup>rd</sup> order filter. (a) The triangular irises. (b) The isosceles triangular resonators. ( $h = 25.1$  mm,  $\theta \approx 60^\circ$ )

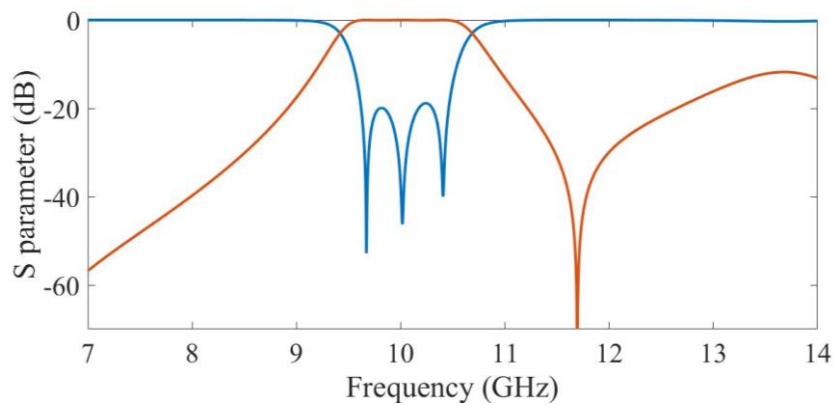


**Figure 6.10** Optimized results of the 3<sup>rd</sup> order BPF.

**Table 6.4** The optimized dimensions of the 3<sup>rd</sup> order filter.

$w_1$ ( $w_3$ )	$w_2$	$b_1$ ( $b_3$ )	$b_2$	$d$	$l$	$h$	$w$
(mm)	(mm)	(mm)	(mm)	(mm)	(mm)	(mm)	(mm)
19.58	17.60	9.79	8.80	3	14.50	25.10	30

## 6.4 Fabrication and measurement

The 3<sup>rd</sup> order filter with quasi-equilateral triangular resonators is manufactured using micro laser sintering (MLS) by a Concept Laser M2. The material is aluminium alloy

A20X. There is no internal supporting structure inside the filter. The triangular structure can realize self-supporting. The base is still raised so support is needed under the filter. But it is a relatively easy support structure and requires less support materials. As shown in Figure 6.11, the flanges have a defect due to the machine instability during the printing. This produced an undesired horizontal line step on the flange surface, which is clear in Figure 6.11 (b) and (c). The screw holes are therefore dislocated which makes flange interconnection difficult. The measurement was done by using alignment pins instead and clamps as shown in Figure 6.11 (a).

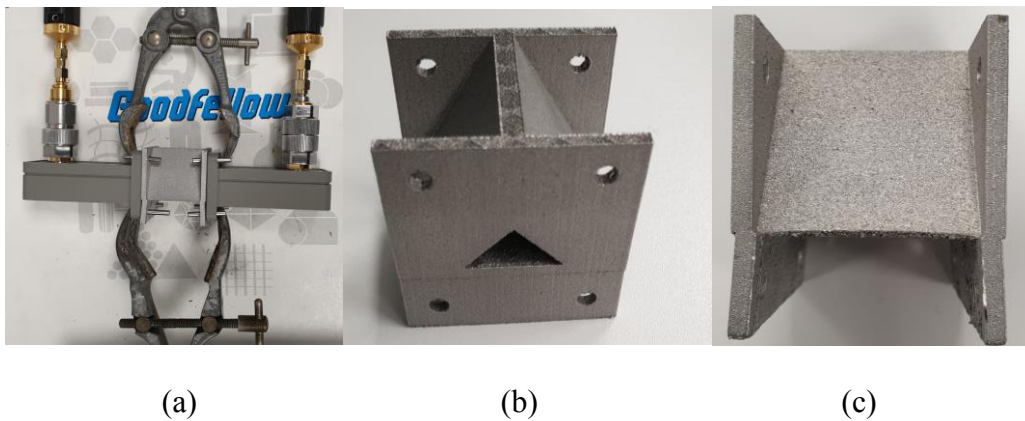


**Figure 6.11** (a) Measurement of the filter with triangular resonators. (b) front view of the filter. (c) Side view of the filter.

The measured results are shown in Figure 6.12. The filter is centred at 9.91 GHz with an 14.2 % 3dB-bandwidth (1.41 GHz). The return loss is better than 13.12 dB in passband. To estimate the tolerance of fabrication, the dimensions are estimated in simulation. The simulated fitting curves using estimated dimensions are shown in Figure 6.12 The dimensions in fitting are shown in Table 6.5. Round corners are considered in fitting. The radius of the round corner is represented as  $r$ . The value of  $w$ ,  $h$ ,  $l$ ,  $w_1$ ,  $w_2$  are larger than designed dimensions. The value of  $d$  is smaller than designed

dimensions. It means that the sizes of cavities are larger than the design. The thickness of irises  $d$  become smaller due to the shrinkage.

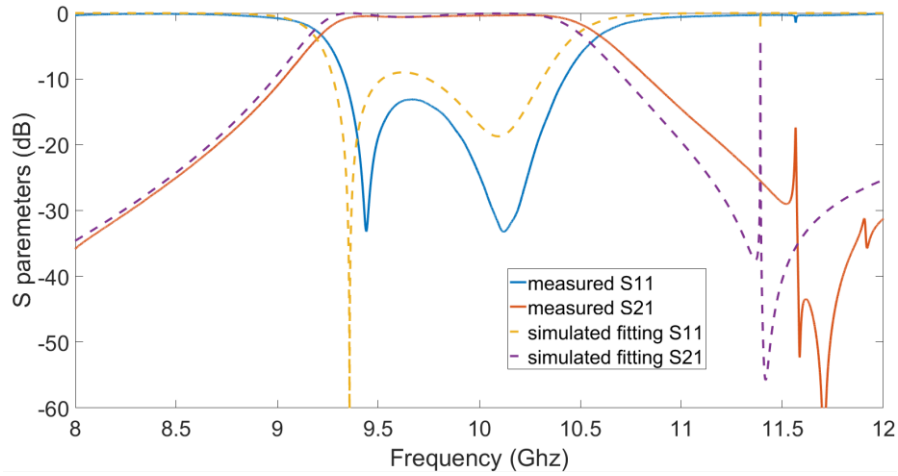


**Figure 6.12** The measured results and the simulated fitting curve of the 3<sup>rd</sup> order filter.

**Table 6.5** The comparison between the designed and estimated dimensions of the 3<sup>rd</sup> order filter. (The parameters are shown clearly in Figure 6.8)

Parameters	$r$ (mm)	$w$ (mm)	$h$ (mm)	$l$ (mm)	$w_1$ ( $w_3$ ) (mm)	$w_2$ (mm)	$d$ (mm)
Designed	0	30	25.10	14.50	19.58	17.60	3.0
Estimated	0.7	30.40	26.20	15.2	19.62	18.00	2.1

## 6.5 Summary

To reduce supporting structures in manufacturing process, triangular resonators are presented and utilized in this Chapter. It begins with the analysis of different triangular

resonators. Then the demonstration of designing a filter with triangular resonators is introduced. In this part, the 2<sup>nd</sup> order waveguide filter is designed. After adjusting this filter, a 3<sup>rd</sup> order filter is designed and fabricated using 3D printing techniques. This is followed by the measurement and analysis. The results are influenced by the low fabrication precision due to machine instability. Further research and fabrication are needed. The results show that the triangular resonator can realize self-supporting structure and no more additional internal supporting structure are needed.

# Chapter 7 Conclusion and future work

## 7.1 Conclusion

This thesis presented the work which can be grouped into two categories: (i) CNC machined waveguides filters working at X band and WR-1.5 band; (ii) 3D printed waveguide filters working at X band and V band.

For the first part, two waveguide bandpass filters are designed and fabricated. The first one is fabricated by high precision CNC machining. Reasonably good agreement between the measurement and simulated results shows that the precision CNC milling is a viable technology for producing terahertz waveguide filters. Sensitivity analysis is provided to improve the fabrication process. Yield analysis is presented to help estimate yield production. The second waveguide filter is designed with a centre frequency of 10 GHz. The folded structure allows a very compact filter with axial connection to waveguide ports. A new coupling structure to increase the bandwidth has been discussed. Staggered cutting plane is used to minimize the disturbance to current and therefore the leakage at contact surface. This folded structure enables highly compact waveguide filter with convenient flange connection and without sacrificing the performance.

For the second part, resonators with different shapes are analyzed and applied in filters. A V band filter is designed and fabricated with 90° twist. After coated with gold, the filter shows good performance and the measured results have a good agreement with the simulated results. 3D printing shows great potential for the devices working at 60 GHz or higher frequency. To reduce supporting structures in manufacturing process,

triangular resonators are presented and utilized in the last filter. The results are influenced by the low fabrication precision due to machine instability. Further research and fabrication are needed. The results show that the triangular resonator can realize self-supporting structure and no more additional internal supporting structure are needed.

## **7.2 Future work**

For the high precision CNC machining work, the 660 GHz folded waveguide filter is difficult to be fabricated. The performance of the filters working in Terahertz is very sensitive to the fabrication tolerance. What's more, the special folded structure increases the difficulty.

Therefore, the further efforts can be made to (i) find a higher precision machine and fabricate the 660 GHz folded waveguide filter; (ii) investigate more waveguide structures works at Terahertz, which can be fabricated by CNC; (ii) further improve the accuracy during fabrication process.

For the 3D printing work, the research on triangular resonators is not enough. More details are needed to be discussed, especially on the electric fields inside the cavities. Take the characteristics of electric fields in triangular resonators to achieve the desired performance in special cases.

The following work will concentrate on (i) analysis of the triangular waveguide filter; (ii) further test the ability of 3D printing in terms of accuracy in higher frequency

# Reference

- [1] Shao Q, Chen F C, Wang Y, et al. Design of Modified 4 x 6 Filtering Butler Matrix Based on All-Resonator Structures[J]. IEEE Transactions on Microwave Theory and Techniques, 2019(67-9).
- [2] Xiu Y Z, Chen J X, Xue Q, et al. Dual-Band Bandpass Filters Using Stub-Loaded Resonators[J]. IEEE Microwave & Wireless Components Letters, 2007, 17(8):583-585.
- [3] Hong J S, Lancaster M J. Theory and experiment of novel microstrip slow-wave open-loop resonator filters[J]. IEEE Transactions on Microwave Theory & Techniques, 2002, 45(12):2358-2365.
- [4] Sheng S, Lei Z. Compact dual-band microstrip bandpass filter without external feeds[J]. IEEE Microwave & Wireless Components Letters, 2005, 15(10):644-646.
- [5] Dong Y D, Yang T, Itoh T. Substrate Integrated Waveguide Loaded by Complementary Split-Ring Resonators and Its Applications to Miniaturized Waveguide Filters[J]. IEEE Transactions on Microwave Theory & Techniques, 2009, 57(9):2211-2223.
- [6] Chen X P, Wu K. Substrate Integrated Waveguide Cross-Coupled Filter With Negative Coupling Structure[J]. IEEE Transactions on Microwave Theory and Techniques, 2008, 56(1):142-149.
- [7] Chin, Kuo-Sheng, Chang, et al. LTCC Multilayered Substrate-Integrated Waveguide Filter With Enhanced Frequency Selectivity for System-in-Package Applications[J]. IEEE Transactions on Components, Packaging & Manufacturing Technology, 2014.
- [8] Shuang L, Jiang H, Xuan Z, et al. Micromachined WR-1.0 waveguide band-pass filter[C]// 2016 IEEE International Conference on Microwave and Millimeter Wave Technology (ICMMT). IEEE, 2016.
- [9] Kirilenko A, Rud L, Tkachenko V, et al. Evanescent-mode ridged waveguide bandpass filters with improved performance[J]. IEEE Transactions on Microwave Theory & Techniques, 2002, 50(5):1324-1327.
- [10] Wu Q, Zhu F, Yang Y, et al. An Effective Approach to Suppressing the Spurious Mode in Rectangular Waveguide Filters[J]. IEEE microwave and wireless components

letters, 2019, 29(11):703-705.

[11] Leong K M K H, Hennig K, Zhang C, et al. WR1.5 Silicon Micromachined Waveguide Components and Active Circuit Integration Methodology[J]. IEEE Transactions on Microwave Theory and Techniques, 2012, 60(4):998-1005.

[12] Lealsevillano C A, Reck T J, Jungkubiak C, et al. Silicon Micromachined Canonical  $E$ -Plane and  $H$ -Plane Bandpass Filters at the Terahertz Band[J]. IEEE Microwave & Wireless Components Letters, 2013, 23(6):288-290.

[13] Zheng Z, Hu J, Liu S, et al. WR-1.5 band waveguide bandpass dual-mode filter on silicon micromachining technique[C]. IEEE International Conference on Communication Problem-Solving. IEEE, 2016:112-114.

[14] Hu J, Liu S, Zhang Y, et al. Micromachined terahertz waveguide band-pass filters[C]. IEEE/MTT-S International Microwave Symposium-ims. IEEE, 2017.

[15] Yang H, Dhayalan Y, Shang X, et al. WR-3 Waveguide Bandpass Filters Fabricated Using High Precision CNC Machining and SU-8 Photoresist Technology[J]. IEEE Transactions on Terahertz Science & Technology, 2018, 8(1):100-107.

[16] Chen Q, Shang X, Tian Y, et al. SU-8 micromachined WR-3 band waveguide bandpass filter with low insertion loss[J]. Electronics Letters, 2013, 49(7):480-481.

[17] Shang X, Tian Y, Lancaster M J, et al. A SU8 Micromachined WR-1.5 Band Waveguide Filter[J]. IEEE Microwave and Wireless Components Letters, 2013, 23(6):300-302.

[18] Ding J Q, Shi S C, Zhou K, et al. Analysis of 220-GHz Low-Loss Quasi-Elliptic Waveguide Bandpass Filter[J]. IEEE Microwave & Wireless Components Letters, 2017, 27(7):648-650.

[19] Zhuang J X, Hong W, Hao Z C. Design and analysis of a terahertz bandpass filter[C]. Wireless Symposium. IEEE, 2015.

[20] Ding J Q, Shi S C, Zhou K, et al. WR-3 Band Quasi-Elliptical Waveguide Filters Using Higher Order Mode Resonances[J]. IEEE Transactions on Terahertz Science & Technology, 2017, PP(99):1-8.

[21] Zhang N, Song R, Hu M, et al. A Low-Loss Design of Bandpass Filter at the Terahertz Band[J]. IEEE Microwave & Wireless Components Letters, PP(99):1-3.

[22] Guo C, Shang X, Li J, et al. A lightweight 3-D printed X-band bandpass filter based on spherical dual-mode resonators[J]. IEEE Microwave and Wireless Components



Letters, 2016, 26(8): 568-570.

[23] Li J, Guo C, Mao L, et al. Monolithically 3-D Printed Hemispherical Resonator Waveguide Filters With Improved Out-of-Band Rejections[J]. IEEE Access, 2018, 6: 57030-57048.

[24] Hong J S, Lancaster M J. Microstrip filters for RF/microwave applications[M]. New York: (2001, Wiley)

[25] Richard J. C, Chandra M. Microwave Filters for Communication Systems, Fundamentals, Design, and Applications (2018, Wiley)

[26] CST Microwave Studio Germany Help Book, CST GmbH 2019.

[27] R. M. Kurzrok, General three-resonator filters in waveguide, IEEE Trans. Microw. Theory Techn., vol. 14, no. 1, pp. 46–47, Jan. 1966.

[28] A. E. Atia and A. E. Williams, Narrow-bandpass waveguide filters, IEEE Trans. Microw. Theory Techn., vol. 20, no. 4, pp. 258–265, Apr. 1972

[29] Carceller C, Soto P, Boria V, et al. Capacitive obstacle realizing multiple transmission zeros for in-line rectangular waveguide filters[J]. IEEE Microwave and Wireless Components Letters, 2016, 26(10): 795-797.

[30] Carceller C, Soto P, Boria V, et al. New folded configuration of rectangular waveguide filters with asymmetrical transmission zeros[C]. 2014 44th European Microwave Conference. IEEE, 2014: 183-186.

[31] Meyler J, Garb K, Kastner R. Waveguide E-plane folded cross-coupled filters[C]. 2013 IEEE International Conference on Microwaves, Communications, Antennas and Electronic Systems (COMCAS 2013). IEEE, 2013: 1-5.

[32] Amari S, Bornemann J. CIET-analysis and design of folded asymmetric H-plane waveguide filters with source-load coupling[C]. 2000 30th European Microwave Conference. IEEE, 2000: 1-4.

[33] Glubokov O, Zhao X, J Champion, et al. Micromachined Filters at 450 GHz With 1% Fractional Bandwidth and Unloaded Q over 700[J]. IEEE Transactions on Terahertz Science and Technology, 2018:1-1.

[34] O. A. Peverini et al., Integration of an H -Plane Bend, a Twist, and a Filter in Ku/K-Band Through Additive Manufacturing, in IEEE Transactions on Microwave Theory and Techniques, vol. 66, no. 5, pp. 2210-2219, May 2018.

[35] Y. Zhang et al., A 3-D Printed Ka-band Twisted Waveguide Filter with Filtering

and Polarization Rotation, 2019 IEEE International Symposium on Antennas and Propagation and USNC-URSI Radio Science Meeting, 2019, pp. 1701-1702.

[36] M. Rezaee and A. U. Zaman, Groove Gap Waveguide Filter Based on Horizontally Polarized Resonators for V-Band Applications, IEEE Transactions on Microwave Theory and Techniques, vol. 68, no. 7, pp. 2601-2609, July 2020.

[37] H. Zhang and Y. Liu, A V-band SIW filter with transmission zero based on high-order mode coupling, 2017 International Applied Computational Electromagnetics Society Symposium (ACES), 2017, pp. 1-2.

[38] B. Ke, H. Chiu, J. S. Fu and Q. Xue, A V-band low insertion loss GaAs bandpass chip filter using CMRC technology, Asia-Pacific Microwave Conference 2011, 2011, pp. 53-56.

[39] R. E. Amaya, A. Momciu and I. Haroun, High-Performance, Compact Quasi-Elliptic Band Pass Filters for V-Band High Data Rate Radios, in IEEE Transactions on Components, Packaging and Manufacturing Technology, vol. 3, no. 3, pp. 411-416, March 2013.

[40] R. Bairavasubramanian and J. Papapolymerou, Development of V-band Integrated Front-Ends on Liquid Crystal Polymer (LCP) Technology, in IEEE Antennas and Wireless Propagation Letters, vol. 7, pp. 134-137.

[41] Guo C, Shang X, Lancaster M J, et al. A 3-D printed lightweight X-band waveguide filter based on spherical resonators[J]. IEEE Microwave and Wireless Components Letters, 2015, 25(7): 442-444.

[42] Rohrdantz B, Rave C, Jacob A F. 3D-printed low-cost, low-loss microwave components up to 40 GHz[C]. 2016 IEEE MTT-S International Microwave Symposium (IMS). IEEE, 2016: 1-3.

[43] Chan K Y, Ramer R, Sorrentino R. Low-Cost Ku-Band Waveguide Devices Using 3-D Printing and Liquid Metal Filling[J]. IEEE Transactions on Microwave Theory and Techniques, 2018 (99): 1-9.

[44] Guo C, Li J, Xu J, et al. An X-band lightweight 3-D printed slotted circular waveguide dual-mode bandpass filter[C]. 2017 IEEE International Symposium on Antennas and Propagation & USNC/URSI National Radio Science Meeting. IEEE, 2017: 2645-2646.

[45] J.-S. Hong and M. J. Lancaster, Microstrip triangular patch resonator filters. IEEE

MTT-S Dig. (1), 2000, 331–334.

[46] M. Cuhaci, and D. S. James, Radiation from triangular and circular resonators in microstrip, IEEE MTT-S Digest 1977, 438–441.

[47] J.-S. Hong, and S. Li, Dual-mode microstrip triangular patch resonators and filters, In 2003 IEEE MTT-S International Microwave Symposium Digest, 1901–1904.

[48] J.-S. Hong, and S. Li, Theory and experiment of dual-mode microstrip triangular patch resonators and filters, IEEE Trans. Microwave Theory Techniques, 2004, 1237–1243.

[49] Moran-Lopez A, Corcoles J, Ruiz-Cruz J A, et al. Dual-mode filters in equilateral triangular waveguides with wide spurious-free response[C]. 2017 IEEE/MTT-S International Microwave Symposium - IMS 2017. IEEE, 2017.

## PUBLICATIONS

1. D. Wang, M. J. Lancaster, Y. Wang, Q. Zhang “WR-1.5 (500-750GHz) waveguide bandpass filter fabricated using high precision CNC machining,” *Microwave and Optical Technology Letters*.
2. T. Skaik, D. Wang “A 3D printed V-band twisted monolithic waveguide bandpass filter” *EuMW 2023*
3. D. Wang, Q. Zhang, Y. Wang “Compact folded waveguide bandpass filter with axial ports,” *Microwave and Optical Technology Letters*. (To be submit)

# WR-1.5 (500-750GHz) waveguide bandpass filter fabricated using high precision CNC machining

Daxin Wang, M. J. Lancaster, K. M. Shum, Qingfeng Zhang and Yi Wang

In this paper, a WR-1.5 band (500-750 GHz) 3<sup>rd</sup> order waveguide bandpass filter has been designed and fabricated using high precision computer numerically controlled (CNC) metal micromachining. The filter has been measured with a 7.29% (48.7 GHz) bandwidth at the centre frequency of 667.5 GHz. The minimum passband insertion loss is measured to be 0.87 dB and the measured return loss is better than 10 dB across the whole passband. The yield percentage is analysed and estimated based on the fabrication tolerance.

**Introduction:** In recent years, the fabrication of high precision components working at terahertz frequencies has received considerable attention due to their emerging applications in security scanning, astronomy, medical and other imaging as well as communication and radar. High precision is needed in the fabrication process. For example, a WR-1.5 rectangular waveguide is 0.381 × 0.1905 mm in cross section. Many different micromachining technologies have been employed to achieve this fabrication precision. In [1-4], silicon deep reactive ion etching (DRIE) was employed with waveguide filters up to 1.033 THz. However, high-accuracy fixtures are required to make the connection with other standard waveguides, which causes additional loss and mismatch. The process also requires a clean room environment with expensive etching facilities. The SU-8 photoresist technology [5-7] has been used to fabricate components up to terahertz frequencies. In [7], a 3<sup>rd</sup> order filter at 671 GHz with 0.65 dB insertion loss and an 8% bandwidth was demonstrated. SU8 exhibits advantages of excellent low insertion losses and high fabrication accuracy. However, the multiple-layer process is subject to assembly errors at higher frequencies [7].

Computer numerical controlled (CNC) milling is a traditional machining technology for metal waveguide structures. Some components fabricated by CNC milling with excellent performance have been reported in [8-15]. A pseudo-elliptic waveguide bandpass filter at 357 GHz with 0.7dB insertion loss and a 9.9 % bandwidth was presented in [8]. A backward wave oscillator working from 405 to 423 GHz was presented in [12] showing a 4 dB insertion loss. In [13], a high pass filter at 385-500 GHz was used in ALMA telescope. In [14], a series of milled filters working at 675- 700 GHz were fabricated for NASA's Aerosol, Cloud and Ecosystems mission. As reported by Jet Propulsion Laboratory in [15], the CNC technique has been further developed and applied to terahertz waveguide circuits up to 1.5 THz, with a very high

dimension accuracy (typically within 2-3 μm of the designed values). However, most of these are by very specialized machining processes. In this paper we use a MAKINO CNC machine from a commercial workshop and consider the yield from an example filter.

Fabricating CNC waveguide filters at terahertz frequencies is limited by the tool sizes and the cutting depth to tool diameter ratios. Currently the minimum tool sizes are around 50 μm in radius, which limits the depth to around 150 μm. In this work, a 3<sup>rd</sup> order filter using standard WR-1.5 waveguide (0.381 × 0.1905 mm) is fabricated by CNC machining to demonstrate the high-end milling techniques in producing terahertz waveguide components. The filter was designed at a centre frequency of 660 GHz with 5% bandwidth. Good results are obtained showing high-precision CNC is a viable technology even for frequencies approaching 1 THz.

**Design and fabrication:** A diagram of the filter is shown in Fig. 1a. Three TE<sub>101</sub> resonators are coupled together via inductive irises. The filter is electroplated in gold with a nominal conductivity of  $4.56 \times 10^7$  S/m used in the simulation. It is designed using the coupling matrix approach [16] to have a Chebyshev response with a centre frequency of 660 GHz, a bandwidth of 5 %, and a return loss of 20 dB.

The external quality factor,  $Q_e$  and coupling coefficients are calculated to be  $Q_{e1} = Q_{e3} = 17.03$ , and  $k_{12} = k_{23} = 0.0516$ . They are controlled by the irises.

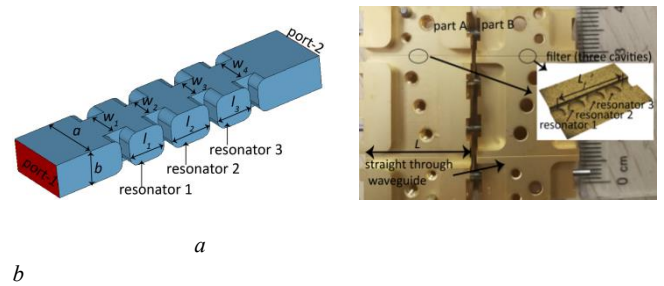


**Fig. 1** Air model of the filter and the CNC machined prototype  
a The air model inside the filter with optimised dimensions ( $w_1 = w_4 = 205.1 \mu\text{m}$ ,  $w_2 = w_3 = 151.9 \mu\text{m}$ ,  $l_1 = l_3 = 213.1 \mu\text{m}$ ,  $l_2 = 241.4 \mu\text{m}$ ).  
b Photograph and the view of cut plane ( $L = 20 \text{ mm}$ ,  $L_f = 0.96 \text{ mm}$ )

The corners of the cavities are rounded as the radius of the cutter used is 50 μm. This is one of the smallest currently available commercially and is taken into consideration in the design. Full-wave simulation and optimization are carried out by CST Microwave Studio [17]. The optimized dimensions are given in Fig. 1a. The simulated response is shown together with the measured results later in Fig. 2.

The filter is split on the E plane into two halves (A and B) as shown in Fig. 1b. This is to minimize the effect of the cut on the insertion loss. The machined part is electroplated with 2 μm gold. The filter is only 0.96 mm in length. However, to accommodate the UG387 standard flanges, a waveguide section of 9.52 mm has to be added between the filter and the test ports, leading to additional losses. In order to estimate and then remove the effect of this extension from the measurement, a straight waveguide of 20 mm is also fabricated alongside the filter.

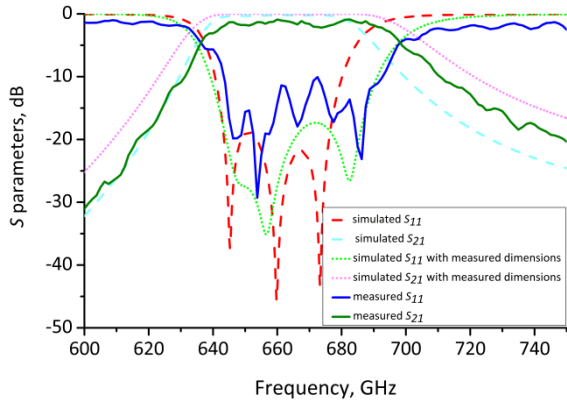


**Fig. 2** Simulated and measured response of the filter.

**Measurement and discussion:** The  $S$  parameter measurement was carried out using a Keysight network analyser with a pair of VDI (Virginia Diodes, Inc.) WR-1.5 waveguide heads. The comparison between the measured responses and the simulated is shown in Fig. 2 with reasonably good agreement. The measured filter has a 7.29% (48.7 GHz) bandwidth at a centre frequency of 667.5 GHz. The measured minimum insertion loss is 0.87 dB and the return loss better than 10 dB across the passband. The centre frequency is shifted upwards by around 7.5 GHz and the bandwidth is slightly larger than designed. This discrepancy is mainly due to the smaller-than-designed dimensions of the resonators and larger irises between them. The small ripples seen in the  $S_{11}$  measurement are most probably caused by the imperfect connection between the filter and waveguide ports.

The dimensions for both halves (A and B) of the manufactured filter were measured using a confocal microscope (ZEISS Smart Proof 5), and the results are given in Table 1. Note that all the lengths ( $l_1, l_2, l_3$ ) are smaller than designed. When re-simulated using the measured dimensions, the performance agrees much better with the measurements as shown in Fig. 2.

**Table 1** Comparison between the designed and measured dimensions.

	$D_{\text{designed}}$ ( $\mu\text{m}$ )	$D_{\text{measured}}^A$ ( $\mu\text{m}$ )	$D_{\text{measured}}^B$ ( $\mu\text{m}$ )	$D_{\text{measured}}^A$ - $D_{\text{designed}}$ ( $\mu\text{m}$ )	$D_{\text{measured}}^B$ - $D_{\text{designed}}$ ( $\mu\text{m}$ )
$l_1$	213.1	190.0	199.0	-23.1	-14.1
$l_2$	241.4	207.0	226.0	-34.4	-15.4
$l_3$	213.1	184.0	197.0	-29.1	-16.1
$w_1$	205.1	219.3	213.6	14.2	8.5
$w_2$	151.9	169.4	162.9	17.5	11
$w_3$	151.9	168.5	162.8	16.6	10.9
$w_4$	205.1	219.4	216.7	14.3	11.6

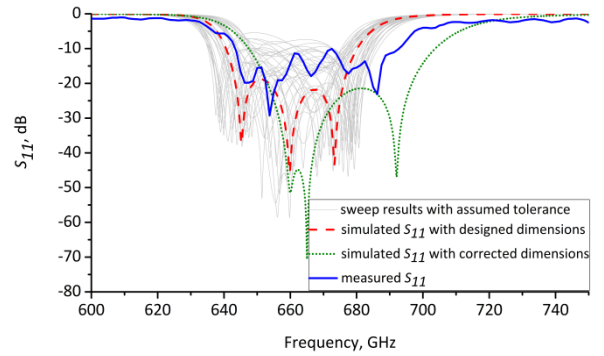


**Fig.3** The  $S_{11}$  parameter with the designed dimensions (red dashed curve) and the  $S_{11}$  parameter with corrected dimensions (green solid curve). The grey curves are the sweep results with assumed tolerance of 2.5  $\mu\text{m}$ . The blue curve is the measured  $S_{11}$ .

**Yield analysis:** Fabrication tolerances lead to performance deviation from the specification. Therefore, a yield analysis is performed. Yield percentage is the ratio of the qualified over the total quantity. This can be estimated after a sensitivity analysis for each parameter in CST microwave studio [17]. Compared with traditional methods, this simplifies the analysis and reduces the calculation time dramatically. Assuming the selection criteria is that the return loss is higher than 10 dB over 643.5- 676.5 GHz, the yield of the filter would be 92.4%, with assumed tolerance of 2.5  $\mu\text{m}$ . An alternative way to depict this is shown in Fig. 3 where a set of sweep results with maximum dimensional variation of 2.5  $\mu\text{m}$  are shown as grey curves. Note if the assumed tolerance rises to 10  $\mu\text{m}$  then the yield reduced to 62.7%. The red dashed curve in Fig. 3 is the simulated  $S_{11}$  parameter with the designed dimensions.

The real dimensional difference between the as-fabricated device and the design is much larger than the assumed tolerance of 2.5  $\mu\text{m}$  in our case. As shown in Table 1, the average difference in length is about -22  $\mu\text{m}$  and 13  $\mu\text{m}$  in width. Of course, this is for only two devices and not statistically significant. Nevertheless, it is not surprising to see that the yield percentage drops to 24.9% using the same selection criterion. The low percentage is mainly due to the frequency shift upwards caused by the generally smaller-than-designed resonators.

If we repeat the simulation using the average measured dimensions (i.e. reducing the lengths by 22  $\mu\text{m}$  and increasing the width by 13  $\mu\text{m}$ ), the passband of the filter will be shifted to 653.14 - 696.7 GHz. The  $S_{11}$  parameter with corrected dimensions is shown as green solid curve in Fig.3. If we use this frequency range as the selection criteria, the yield percentage becomes 78.6% under the average machine tolerance.

**Conclusion:** A high precision CNC milled waveguide bandpass filter working in the WR-1.5 band has been designed and fabricated. The filter is centred at 667.5 GHz with a 7.29% bandwidth. Reasonably good agreement between the measurement and simulated results shows that the precision CNC milling is a viable technology for producing terahertz waveguide filters. However, machine tolerance would significantly reduce the yield of production. Higher fabrication accuracy and tighter tolerance control is needed for high yield in the fabrication of terahertz waveguide devices.

Daxin Wang, M. J. Lancaster and Yi Wang (*Department of Electronic, Electrical and Systems Engineering, University of Birmingham, Birmingham B15 2TT, United Kingdom*)  
Qingfeng Zhang (*Department of Electrical and Electronic Engineering, Southern University of Science and Technology, Shenzhen 518055,*

People's republic of China)

E-mail: zhangqf@sustech.edu.cn

K. M. Shum(Department of Electronic Engineering, City University of Hong Kong, Hong Kong, People's republic of China )

Daxin Wang: Also with Department of Electrical and Electronic Engineering, Southern University of Science and Technology, Shenzhen 518055, People's republic of China.

## References

- 1 Leong, K. M., Hennig, K., et al.: 'WR1.5 silicon micromachined waveguide components and active circuit integration methodology', *Trans. Micro. Theory. Tech.*, 2012, **60**, (4), pp. 998-1005
- 2 Leal-Sevillano, C. A., Reck, T. J., et al.: 'Silicon micromachined canonical E-plane and H-plane bandpass filters at the terahertz band', *Microw. Wirel. Compon. Lett.*, 2013, **23**, (6), pp. 288-290.
- 3 Zheng, Z., Hu, J., et al.: 'WR-1.5 band waveguide bandpass dual-mode filter on silicon micromachining technique', IEEE Int. conf. Commu. Problem-Solving., October 2016, pp. 112-114
- 4 Hu, J., Liu, S., et al.: 'Micromachined terahertz waveguide band pass filters' IEEE MTT-S Int. Microwave Symp., Honolulu, HI, June 2017, pp. 650-653
- 5 Yang, H., Dhayalan, Y., et al.: 'WR-3 waveguide bandpass filters fabricated using high precision CNC machining and SU-8 photoresist technology', *Trans. Terahertz Science & Tech.*, 2018, **8**, (1), pp. 100-107
- 6 Chen, Q., Shang, X., et al.: 'SU-8 micromachined WR-3 band waveguide bandpass filter with low insertion loss', *Electron. Lett.*, 2013, **49**, (7), pp. 480-482
- 7 Shang, X., Tian, Y., Lancaster, M. J., et al.: 'A SU8 micromachined WR-1.5 band waveguide filter', *Microw. Wirel. Compon. Lett.*, 2013, **23**, (6), pp. 300-302.
- 8 Feng, Y., Zhang, B., et al.: 'WR-2.8 band pseudo-elliptic waveguide filter based on singlet and extracted pole resonator', *IEEE Access*, 2019, April.
- 9 Zhuang, J. X., Hong, W., et al.: 'Design and analysis of a terahertz bandpass filter', IEEE Wireless Symp., Shenzhen, 2015, pp. 1-4
- 10 Ding, J. Q., Shi, S. C., Zhou, K., et al.: 'WR-3 band quasi-elliptical waveguide filters using higher order mode resonances', *Trans. Terahertz Science & Tech.*, 2017, **7**, (3), pp. 1-8
- 11 Zhang, N., Song, R., Hu, M., et al.: 'A low-loss design of bandpass filter at the terahertz band', *Microw. Wirel. Compon. Lett.*, 2018, **28**, (7), pp. 573-575
- 12 Lee, I., Shin, J., Choi, E.: 'Nano-CNC fabricating Y-band folded waveguide backward wave oscillator', Int. Vacuum Electronics Conf., London, 2017, pp. 1-2, doi 10.1109/IVEC.2017. 8289585
- 13 Alvaro, G., Takafumi K., et al.: '275-500 GHz waveguide diplexer to combine local oscillators for different frequency bands,' *Trans. Terahertz Science & Tech.*, vol. 7, no. 6, pp. 669-676, Nov. 2017
- 14 Koller, D., Hesler, J., et al.: 'WM380 (675-700GHz) band-pass filters in milled, split-block construction', *Trans. Terahertz Science & Tech.*, 2018.
- 15 Bruneau, P. J., et al.: 'Machining of terahertz split-block waveguides with micrometer precision' International Conference on Infrared IEEE, 2008.
- 16 Hong, J.-S., and Lancaster, M.J.: 'Microstrip filters for RF/microwave applications' (Wiley, New York, 2001)
- 17 **CST Microwave Studio Germany, CST GmbH 2017**